Device Analysis of Thermally-Activated Delayed Fluorescence-Based Organic Light-Emitting Diodes Aimed for High Device Stability

田中, 正樹

https://doi.org/10.15017/4060120

出版情報：九州大学, 2019, 博士（工学）, 課程博士
バージョン：
権利関係：

2019

Doctor thesis

Device Analysis of Thermally-Activated Delayed Fluorescence-Based Organic Light-Emitting Diodes Aimed for High Device Stability

Masaki Tanaka

Department of Chemistry and Biochemistry

Graduate School of Engineering

Kyushu University

Table of contents

Chapter 3

Proving the origin of degradation in an organic light-emitting diode derived from triplet exciton interaction by a magnetic field

Chapter 1

Introduction of this thesis

1-1. Background and motivation

Since C. W. Tang and S. A. VanSlyke demonstrated an organic light-emitting diode (OLED) based on two stacked layers of organic molecules[1], OLED characteristics have been improved by numerous fundamental and industrial studies[2–6]. OLEDs have been attracting considerable attentions because the devices offer the possibility of low-cost fabrication of flexible and lightweight devices with high electroluminescence (EL) efficiency. A basic OLED structure shown in **Figure 1-1** contains organic layers having different functions during device operation. When an electric field is applied to the device, holes and electrons are injected from the cathode and the anode, respectively, and are transported in organic layers such as a hole-transport layer (HTL) and an electron-transport layer (ETL). The transported carriers encounter in the emission layer (EML) and recombine to generate excitons. Electrically generated excitons follow the spin-statics law[7], resulted in the generation ratio of singlet and triplet excitons with 1:3. Generally, only singlet excitons can contribute the EL from the devices based on a conventional fluorescence emitter.

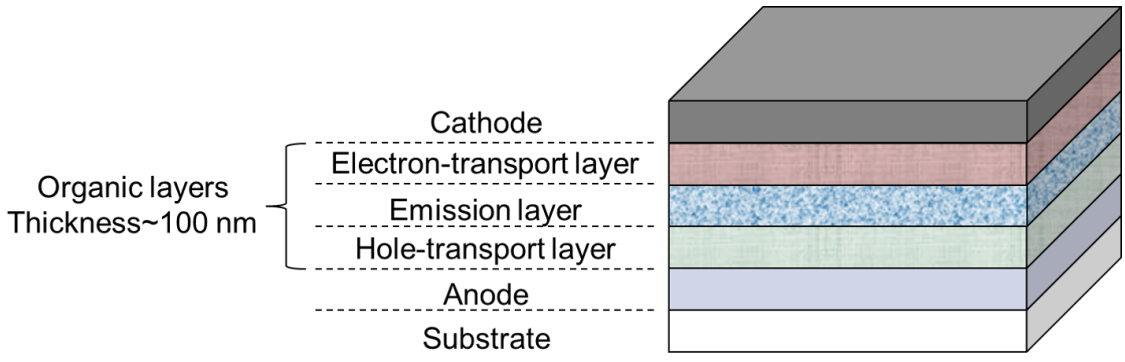

Figure 1-1. Typical device structure of an OLED.

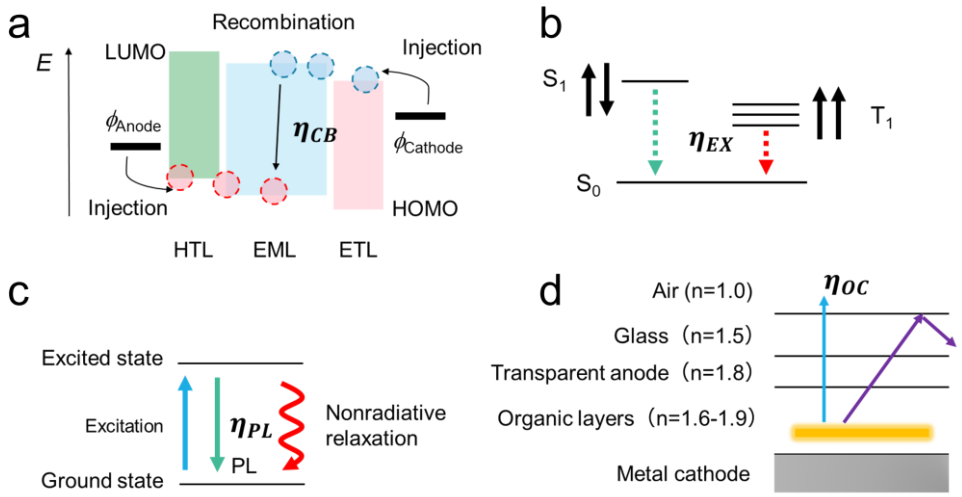

Figure 1-2. The operation processes of an OLED. (a), (b), (c) and (d) depict the carrier recombination, the exciton generation, the relaxation from an excited state to a ground state and light-outcoupling processes, respectively. HOMO and LUMO are the highest occupied and the lowest unoccupied molecular orbitals, respectively. ϕ_{Anode} and ϕ_{Cathode} are the work functions of anode and cathode, respectively.

Because of the operation mechanisms expressed above, an emission efficiency of OLEDs, *i.e.*, external EL quantum efficiency (EQE), is given by

$$\mathrm{EQE} = \eta_{CB} \times \eta_{EX} \times \eta_{QY} \times \eta_{OC}$$

where η_{CB}, η_{EX}, η_{QY} and η_{OC} are a carrier balance factor of injected carriers, an exciton-utilization efficiency, a photoluminescence (PL) quantum efficiency and a light-outcoupling efficiency as depicted in **Figure 1-2**. In the history of OLED research, to obtain the high EQE, the development of emitter molecules has been most important R&D subject[2,3,8,9].

The η_{EX} of the devices based on typical fluorescent emitters such as tris(8-hydroxyquinolinato)aluminium (Alq_3) is limited by 25% because the generated triplet excitons cannot contribute the EL emission. To improve the device efficiency, several triplet exciton harvesting technologies for OLEDs such as a triplet-triplet annihilation (TTA)[5,10], phosphorescence[2,8], and thermally-activated delayed fluorescence (TADF)[3,9]

have been studied as the schematics shown in **Figure 1-3**. The phosphorescent emitters such as tris(2-phenylpyridine)iridium(III) ($Ir(ppy)_3$)[2] efficiently emit room-temperature phosphorescence, *i.e.*, a relaxation from the lowest excited triplet state (T_1) to the ground state (S_0), due to a strong spin-orbit coupling induced by a heavy atom such as Ir. Then, all the electrically generated excitons can be converted to triplet excitons, contributing EL through the phosphorescence process.

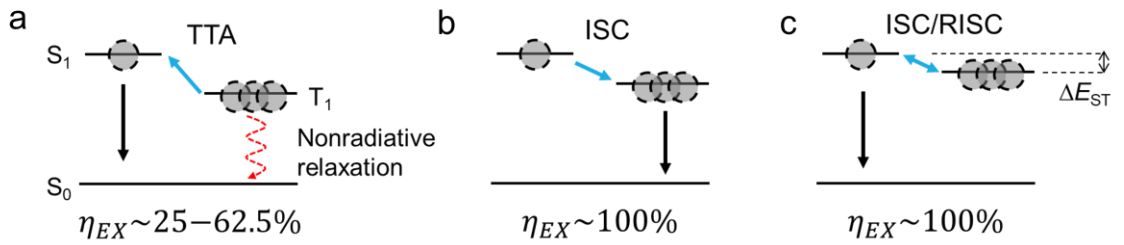

Figure 1-3. Schematics of exciton relaxation processes under electrical excitation. (a) fluorescent emitters with TTA, (b) phosphorescent emitters and (c) TADF emitters.

In contrast, TADF emitters exhibit an upconversion of excitons from an excited triplet state to an excited singlet state, *i.e.*, the reverse intersystem crossing (RISC), due to nearly zero energy gap between the lowest singlet and triplet excited energy levels (ΔE_{ST}). Then, all the excitons can contribute EL emission as fluorescence from the lowest excited singlet state (S_1)[3,9]. TADF emitters have a potential to achieve ultimate device performance and low cost for industrial fabrication because of no use of heavy atoms in TADF molecules. Although the great potential of TADF emitters is expected for display and lighting technologies, the device lifetime of TADF-OLEDs is still shorter than conventional fluorescent and phosphorescent OLEDs[11,12]. To spread TADF-OLEDs widely for commercial applications, the device stability of TADF-OLEDs must be improved.

To improve OLEDs' lifetimes, understanding of detailed degradation phenomena

is mandatory and several major mechanisms have been already proposed in fluorescence and phosphorescence based OLEDs[12–21]. Device degradation, *i.e.*, luminance decrease and voltage increase, results from the change in each quantum yield of η_{OC}, η_{EX}, η_{QY}, and η_{CB} under continuous operation. As shown in **Figure 1-4**, numerous factors can be considered as possible mechanisms to change the quantum yields in operating devices. Furthermore, previous researches revealed that the fundamental degradation origins are, for example, joule heat[19,20], exciton interaction[22,23], exited state stability[12,16], anion/cation/radical state stability[14,21], and interfacial stability between organic and metal layers[24,25] by means of several analysis methods. For device degradation study, some chemical, thermal and electrochemical analysis methods for organic materials, and optical, electrical, and simulation methods for devices are combined to reveal degradation mechanism. For example, Kondakov investigated the degradation behavior in the devices based on arylamine-type hole-transporting materials and Alq_3 by means of devices' voltammetric responses and mass spectroscopy to detect decomposed materials[14]. He observed the change in carrier injection characteristics in degraded devices and identified the degradation products induced from hole-transporting materials acting as carrier traps and nonradiative recombination centers in degraded devices. Further, he concluded the dominant degradation origin in his devices is the dissociations of weak carbon-nitrogen and carbon-carbon bonds in the hole-transporting materials, and luminance loss is induced by change in carrier balance, nonradiative recombination, and exciton quenching[14].

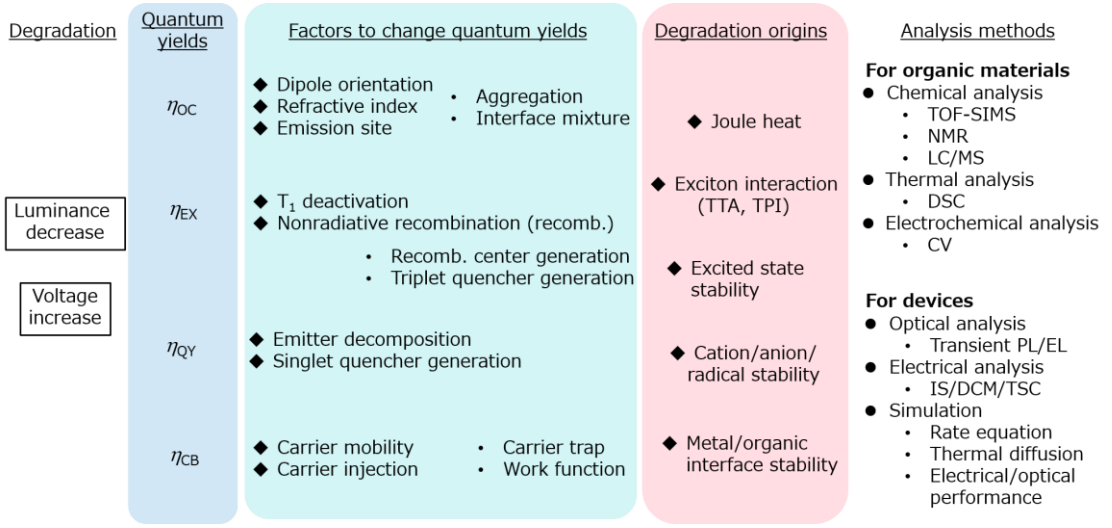

Figure 1-4. Schematics of device degradation mechanisms and analysis methods used for degradation analysis. TOF-SIMS, NMR, LC-MS, DSC, and CV are time-of-flight secondary ion mass spectroscopy[26], nuclear magnetic resonance[13], liquid chromatography-mass spectroscopy[14], differential scanning calorimetry[27], and cyclic voltammetry[28], respectively. IS, DCM, and TSC are impedance spectroscopy[29], displacement current measurement[30], and thermally stimulated current spectroscopy[31], respectively.

In case of devices based on phosphorescent and TADF emitters, triplet excitons generated under electrical excitation efficiently contribute EL as phosphorescence and fluorescence, respectively. However, rather long-lived and densely populated triplet excitons might become a reaction center for triplet exciton interactions such as TTA and triplet-polaron interaction (TPI) as shown in **Figure 1-5**[16–18,22,32]. Triplet excitons are quenched via these unwanted interactions to generate the high-energy particles such as highly-excited triplet excitons and polarons with enough high energy that results in chemical decomposition of organic materials. Giebink et al. studied the degradation mechanism of phosphorescent OLEDs by a numerical model to fit the device performance[22]. They tried to fit the trend in luminance decrease, voltage increase, and transient PL profiles in device degradation processes, and found that the model based TPI

as defect formation mechanism can fit the degraded device characteristics. Therefore, they concluded that most dominant degradation mechanism of phosphorescent OLEDs is the defect formation in an EML via TPI and broad recombination site width is preferable to suppress the unwanted annihilations such as TTA and TPI. Zhang et al. fabricated the phosphorescent devices based on graded dopant concentrations in the EMLs to lower the absolute exciton densities with broad distribution[33]. They successfully improved device lifetimes because of suppressed unwanted triplet interactions. Therefore, suppression of triplet interactions must be one of critical issues to elongate the device lifetime even in TADF-OLEDs.

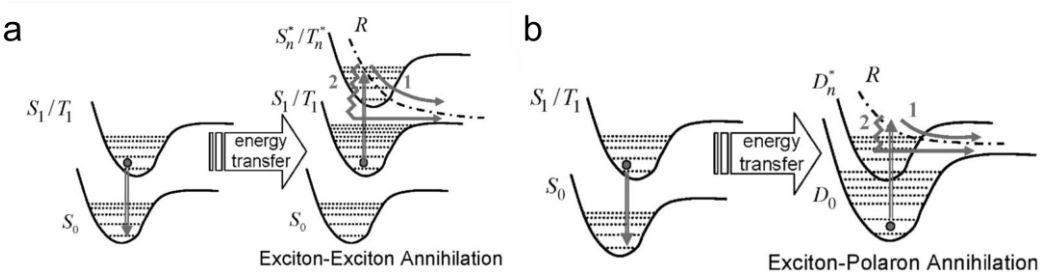

Figure 1-5. Schematics of intermolecular exciton interactions. (a) the exciton-exciton interaction. (b) the exciton-polaron interaction. (These figures were cited from N. C. Giebink *et al*., *J. Appl. Phys.* **103**, 044509 (2008)[22])

For the evaluation of exciton annihilation processes in OLEDs, the rate equations for exciton population have been widely used[34,35]. Those analyses were performed with the models based on exciton annihilation such as TTA, TPI and singlet-triplet annihilation (STA). However, because of several fitting parameters and the presence of multiple exciton annihilation processes, the analyses are complicated and difficult to apply to various situations. Therefore, a nondestructive analysis method for exciton dynamics under device operation has been strongly required for comprehensive understanding of

the exciton annihilation and degradation phenomena.

For proving triplet exciton dynamics, magnetic field effects (MFEs) in OLEDs have been investigated because an applied magnetic field can separate the degenerate triplet states generated in operating devices and modulate the device performance that reflects the triplet exciton dynamics[36–38]. The separation (Zeeman splitting, ΔE_Z) of the degenerate levels by a magnetic field (B) can be expressed by $g\mu_B B$ with g factor (g) and Bohr magneton (μ_B)[39] (**Figure 1-6**). In principle, the magnetic response mechanisms based on polaron-pair (PP) and triplet interaction models are used to understand the MFEs in OLEDs. PP (electron-hole pair) model is based on the suppression of intersystem crossing (ISC_{PP}) processes between a singlet PP (^{1}PP) state and triplet PP (^{3}PP) states that are well balanced under B=0 because of small energy difference between ^{1}PP and ^{3}PP[40]. As a result, suppressed ISC_{PP} increases the ^{1}PP population and the characteristic magnetic field is around 5 mT that can be estimated by the hyperfine coupling strength of PP states[40]. Magnetic response based on a triplet interaction model effectively decreases the reaction rate of triplet interaction such as TPI under the B (~100 mT)[41] corresponding to the zero-field splitting (ZFS) of a triplet excited state of organic molecules around 10 μeV (~ΔE_Z at 100 mT)[42,43]. On the other hand, the magnetic response of intersystem crossing in excitonic states (ISC_{EX}) is not common. Because ISC_{EX} is governed by relatively large ΔE_{ST} and slow ISC_{EX} rate, ΔE_Z under ~1 T cannot directly affect the excitonic state character. If the B corresponding to the ΔE_{ST}~100 meV for TADF molecules, *i.e.*, ~1 kT, is applied, the ISC_{EX} might be affected. Therefore, under the conventional experimental setup to apply B~1 T, PP and triplet interaction models are general mechanisms for MFEs in OLEDs (see discussion in **Chapter 3**).

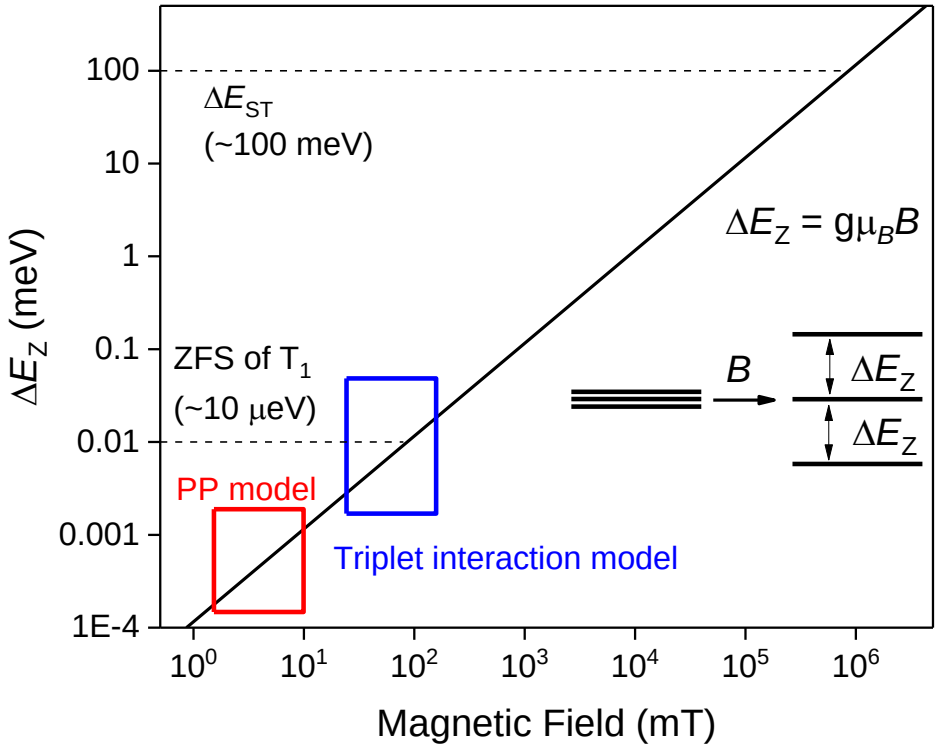

Figure 1-6. Relationship between magnetic field (B) and Zeeman splitting (ΔE_Z). Inset is schematic of Zeeman splitting of degenerate triplet state.

Furthermore, an improvement of OLEDs' EQE is also important to lengthen the device lifetime because high efficiency results in low operational current density, *i.e.*, low electrical stress for the devices under constant current operation. By the utilization of TADF molecules as emitters, internal quantum efficiency, IQE, defined by $\eta_{CB} \times \eta_{EX} \times \eta_{QY}$ has been reached to nearly 100%, whereas EQE is still limited by η_{OC}. Because OLEDs have many kinds of layers with different refractive indices such as a glass substrate, metal, transparent anode and organic layers. The interfaces with different refractive indices generate optical losses due to a refraction at the interfaces such as air/glass, glass/transparent anode, transparent anode/organic layer and organic/organic

layers. According to simple optical calculation, the η_{OC} is limited by around 20% with random orientation of transition dipole moment (TDM) of an emitter[44,45]. It has been reported that several special techniques can enhance the η_{OC} with microlens arrays[46,47], scattering particles[48,49] and grating structures[50,51]. However, for practical applications for display technology, it is difficult to apply those techniques because of the problems for high resolution, view angle and fabrication processes.

An increased fraction of emission to normal direction to a substrate from an EML enhances the η_{OC} because of the decreased confined EL by the refraction at the interfaces. The horizontal orientation of a TDM in an amorphous film that enhances η_{OC} has been reported[44,52–55]. According to an optical simulation, the perfectly horizontal TDM orientation can achieve approximately 1.5-times higher η_{OC} than that of the device based on random TDM orientation (**Figure 1-7**)[44,45]. TADF emitters exhibiting highly horizontal TDM orientations have been reported, and nearly 30% of EQEs of the OLEDs have been demonstrated[54–56].

Recently, the horizontal TDM orientations of the disk-like shaped TADF molecules in aligned mono-layer such as 2,4,5,6-tetra(9H-carbazol-9-yl)isophthalonitrile (4CzIPN) are reported[57]. Furthermore, because of the high potential of those carbazole-benzonitrile bridged emitters for OLEDs, the development of those emitters were well studied to achieve high EQE and extended stability[9,31]. Although the origin of horizontal orientation of linear-shape molecules has been studied, the mechanism of the orientation of disk-shaped molecules has not been clarified. The realization of perfect horizontal orientation of those high-performance molecules is desired to obtain an ultimate OLED performance.

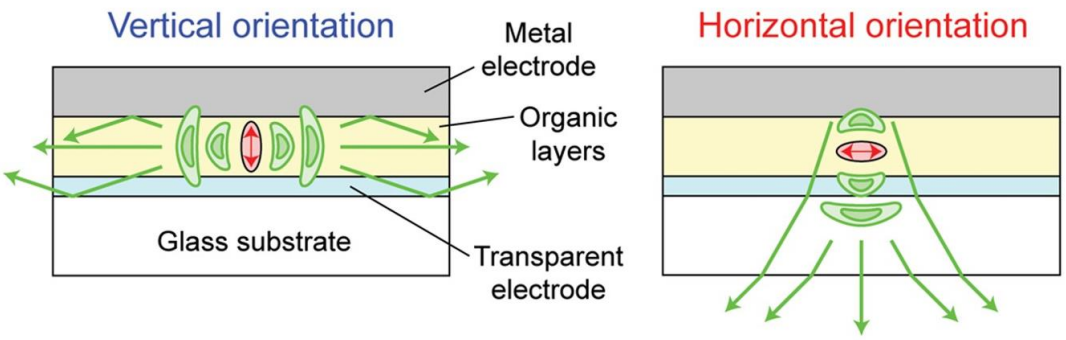

Figure 1-7. Schematics of the light-outcoupling of OLEDs with vertical and horizontal TDM orientations of emitters **(**This figure was cited from D. Yokoyama, *J. Mater. Chem.*, **21**, 19187-19202 (2011)[44]).

1-2. Purpose and outline

In this study, the research focused on the understanding of origins of OLED degradation and molecular orientation in films to develop highly efficient and stable TADF-OLEDs. Better understanding of the mechanisms can suggest the strategies to achieve ultimate OLED performance. In **Chapter 2**, the device characteristics of the OLEDs based on penta(9H-carbazol-9-yl)benzonitrile (5CzBN) and 2,4,6-tris(9H-carbaozle-9-yl)-3,5-bis(3,6-diphenylcarbazole-9-yl)benzonitrile (3Cz2DPhCzBN)[9] were compared in terms of the degradation events. 5CzBN-OLED exhibited the changes in EL spectral shape during an operational degradation, which suggested the change in the location of emission site in the emission layer, originating from changes in the carrier transport properties. This study concluded that the unwanted triplet exciton-polaron interaction (TPI) is a significant channel for the degradation of TADF-OLEDs.

In **Chapter 3**, magnetic field effects in OLEDs were studied to apply as an analysis method to investigate unwanted triplet interactions such as TPI that causes the device degradation as studied in **Chapter 2**. Magnetic-field-modulated EL (magneto-electroluminescence, MEL) of TADF-OLEDs largely depended on the delayed emission lifetimes of TADF emitters. This study identified that the MEL of TADF-OLEDs originated from the magnetic responses of electron-hole pairs and the TPI reaction, and confirmed that the shorten triplet-exciton-lifetimes of emitters decrease the rate of TPI reaction. Furthermore, the MEL-method was applied for the degradation analysis of the devices, and revealed that the inefficient exciton generation channels such as interfacial exciplex-formation were happened in the degraded OLEDs. According to **Chapters 2** and **3**, the degradation phenomena of TADF-OLEDs were comprehensively investigated and the strategies to improve device stability were proposed.

In **Chapter 4**, the molecular orientations in doped films based on host-guest system were studied to reveal the origin of horizontal molecular orientations. By means of optical and electrical analysis methods, the characterizations of transition and permanent dipole orientations of molecules were performed. We clarified that a glass transition temperature of host and intermolecular dipole-dipole interactions are ones of dominant issues to control emitter orientations in deposited films. Furthermore, a perfectly horizontal TDM orientation and η_{OC}~30% were demonstrated for TADF:host doped system. In **Chapter 5**, this thesis was summarized and future prospects were introduced.

References

1. C. W. Tang & S. A. Vanslyke, Organic electroluminescent diodes. *Appl. Phys. Lett.* **51**, 913–915 (1987).
2. C. Adachi, M. A. Baldo, S. R. Forrest & M. E. Thompson, High-efficiency organic electrophosphorescent devices with tris(2-phenylpyridine)iridium doped into electron-transporting materials. *Appl. Phys. Lett.* **77**, 904–906 (2000).
3. H. Uoyama, K. Goushi, K. Shizu, H. Nomura & C. Adachi, Highly efficient organic light-emitting diodes from delayed fluorescence. *Nature*. **492**, 234–238 (2012).
4. C. J. Chiang, C. Winscom, S. Bull & A. Monkman, Mechanical modeling of flexible OLED devices. *Org. Electron.* **10**, 1268–1274 (2009).
5. H. Kuma & C. Hosokawa, Blue fluorescent OLED materials and their application for high-performance devices. *Sci. Technol. Adv. Mater.* **15** (2014).
6. H. Nakanotani, T. Higuchi, T. Furukawa, K. Masui, K. Morimoto, M. Numata, H. Tanaka, Y. Sagara, T. Yasuda & C. Adachi, High-efficiency organic light-emitting diodes with fluorescent emitters. *Nat. Commun.* **5**, 4016 (2014).
7. M. A. Baldo, D. F. O'Brien, M. E. Thompson & S. R. Forrest, Excitonic singlet-triplet ratio in a semiconducting organic thin film. *Phys. Rev. B.* **60**, 14422–14428 (1999).
8. J. Lee, H.-F. Chen, T. Batagoda, C. Coburn, P. I. Djurovich, M. E. Thompson & S. R. Forrest, Deep blue phosphorescent organic light-emitting diodes with very high brightness and efficiency. *Nat. Mater.* **15**, 92–98 (2015).
9. H. Noda, H. Nakanotani & C. Adachi, Excited state engineering for efficient reverse intersystem crossing. *Sci. Adv.* **4**, eaao6910 (2018).

10. D. Y. Kondakov, T. D. Pawlik, T. K. Hatwar & J. P. Spindler, Triplet annihilation exceeding spin statistical limit in highly efficient fluorescent organic light-emitting diodes. *J. Appl. Phys.* **106**, 124510 (2009).

11. H. Nakanotani, K. Masui, J. Nishide, T. Shibata & C. Adachi, Promising operational stability of high-efficiency organic light-emitting diodes based on thermally activated delayed fluorescence. *Sci. Rep.* **3**, 2127 (2013).

12. A. S. D. Sandanayaka, T. Matsushima & C. Adachi, Degradation Mechanisms of Organic Light-Emitting Diodes Based on Thermally Activated Delayed Fluorescence Molecules. *J. Phys. Chem. C*. **119**, 23845–23851 (2015).

13. D. Y. Kondakov, W. C. Lenhart & W. F. Nichols, Operational degradation of organic light-emitting diodes: Mechanism and identification of chemical products. *J. Appl. Phys.* **101**, 024512 (2007).

14. D. Y. Kondakov, Role of chemical reactions of arylamine hole transport materials in operational degradation of organic light-emitting diodes. *J. Appl. Phys.* **104**, 084520 (2008).

15. S. Scholz, D. Kondakov, B. Lüssem & K. Leo, Degradation mechanisms and reactions in organic light-emitting devices. *Chem. Rev.* **115**, 8449–8503 (2015).

16. N. C. Giebink, B. W. D'Andrade, M. S. Weaver, J. J. Brown & S. R. Forrest, Direct evidence for degradation of polaron excited states in organic light emitting diodes. *J. Appl. Phys.* **105**, 124514 (2009).

17. J. Lee, C. Jeong, T. Batagoda, C. Coburn, M. E. Thompson & S. R. Forrest, Hot excited state management for long-lived blue phosphorescent organic light-emitting diodes. *Nat. Commun.* **8**, 15566 (2017).

18. W. Song & J. Y. Lee, Degradation Mechanism and Lifetime Improvement Strategy

for Blue Phosphorescent Organic Light-Emitting Diodes. *Adv. Opt. Mater.* **5**, 1600901 (2017).

19. K. Yoshida, T. Matsushima, Y. Shiihara, H. Kuwae, J. Mizuno & C. Adachi, Joule heat-induced breakdown of organic thin-film devices under pulse operation. *J. Appl. Phys.* **121**, 195503 (2017).

20. J. R. Gong, L. J. Wan, S. Bin Lei, C. L. Bai, X. H. Zhang & S. T. Lee, Direct evidence of molecular aggregation and degradation mechanism of organic light-emitting diodes under joule heating: An STM and photoluminescence study. *J. Phys. Chem. B.* **109**, 1675–1682 (2005).

21. N. Lin, J. Qiao, L. Duan, H. Li, L. Wang & Y. Qiu, Achilles heels of phosphine oxide materials for OLEDs: Chemical stability and degradation mechanism of a bipolar phosphine oxide/carbazole hybrid host material. *J. Phys. Chem. C.* **116**, 19451–19457 (2012).

22. N. C. Giebink, B. W. D'Andrade, M. S. Weaver, P. B. MacKenzie, J. J. Brown, M. E. Thompson & S. R. Forrest, Intrinsic luminance loss in phosphorescent small-molecule organic light emitting devices due to bimolecular annihilation reactions. *J. Appl. Phys.* **103**, 044509 (2008).

23. W. Song, T. Kim, J. Y. Lee, Y. Lee & H. Jeong, Investigation of degradation mechanism of phosphorescent and thermally activated delayed fluorescent organic light-emitting diodes through doping concentration dependence of lifetime. *J. Ind. Eng. Chem.* **68**, 350–354 (2018).

24. Q. Wang, Y. Luo & H. Aziz, Photodegradation of the organic/metal cathode interface in organic light-emitting devices. *Appl. Phys. Lett.* **97**, 2008–2011 (2010).

25. Q. Wang & H. Aziz, Exciton-induced degradation of organic/electrode interfaces

in ultraviolet organic photodetectors. *Org. Electron.* **14**, 3030–3036 (2013).

26. B. M. Bell, M. B. Clark, D. D. Devore, T. S. De Vries, R. D. Froese, K. C. Gray, D. H. K. Jackson, T. F. Kuech, H. Y. Na, K. L. Kearns, K. J. Lee, S. Mukhopadhyay, A. A. Rachford, L. P. Spencer & W. H. H. Woodward, Degradation of Hole Transport Materials via Exciton-Driven Cyclization. *ACS Appl. Mater. Interfaces*. **9**, 13369–13379 (2017).

27. J. Kwak, Y. Y. Lyu, S. Noh, H. Lee, M. Park, B. Choi, K. Char & C. Lee, Hole transport materials with high glass transition temperatures for highly stable organic light-emitting diodes. *Thin Solid Films*. **520**, 7157–7163 (2012).

28. S. Kim, H. J. Bae, S. Park, W. Kim, J. Kim, J. S. Kim, Y. Jung, S. Sul, S. G. Ihn, C. Noh, S. Kim & Y. You, Degradation of blue-phosphorescent organic light-emitting devices involves exciton-induced generation of polaron pair within emitting layers. *Nat. Commun.* **9**, 1211 (2018).

29. S. Nowy, W. Ren, A. Elschner, W. Lövenich & W. Brütting, Impedance spectroscopy as a probe for the degradation of organic light-emitting diodes. *J. Appl. Phys.* **107**, 054501 (2010).

30. Y. Kim, H. J. Ishino, R. Nakayama & Y. Ishii, Charge carrier dynamics in organic light-emitting diodes doped by a thermally activated delayed fluorescence emitter. *Org. Electron.* **17**, 114508 (2013).

31. D. P. K. Tsang, T. Matsushima & C. Adachi, Operational stability enhancement in organic light-emitting diodes with ultrathin Liq interlayers. *Sci. Rep.* **6**, 22463 (2016).

32. M. A. Baldo, C. Adachi & S. R. Forrest, Transient analysis of organic electrophosphorescence. II. Transient analysis of triplet-triplet annihilation. *Phys.*

Rev. B. **62**, 10967–10977 (2000).

33. Y. Zhang, J. Lee & S. R. Forrest, Tenfold increase in the lifetime of blue phosphorescent organic light-emitting diodes. *Nat. Commun.* **5**, 5008 (2014).

34. K. Masui, H. Nakanotani & C. Adachi, Analysis of exciton annihilation in high-efficiency sky-blue organic light-emitting diodes with thermally activated delayed fluorescence. *Org. Electron.* **14**, 2721–2726 (2013).

35. M. Inoue, T. Serevičius, H. Nakanotani, K. Yoshida, T. Matsushima, S. Juršenas & C. Adachi, Effect of reverse intersystem crossing rate to suppress efficiency roll-off in organic light-emitting diodes with thermally activated delayed fluorescence emitters. *Chem. Phys. Lett.* **644**, 62–67 (2016).

36. W. P. Gillin, S. Zhang, N. J. Rolfe, P. Desai, P. Shakya, A. J. Drew & T. Kreouzis, Determining the influence of excited states on current transport in organic light emitting diodes using magnetic field perturbation. *Phys. Rev. B* **82**, 195208 (2010).

37. P. Desai, P. Shakya, T. Kreouzis & W. P. Gillin, Magnetoresistance in organic light-emitting diode structures under illumination. *Phys. Rev. B* **76**, 235202 (2007).

38. A. J. Schellekens, W. Wagemans, S. P. Kersten, P. A. Bobbert & B. Koopmans, Microscopic modeling of magnetic-field effects on charge transport in organic semiconductors. *Phys. Rev. B* **84**, 075204 (2011).

39. Ö. Mermer, G. Veeraraghavan, T. L. Francis, Y. Sheng, D. T. Nguyen, M. Wohlgenannt, A. Köhler, M. K. Al-Suti & M. S. Khan, Large magnetoresistance in nonmagnetic π-conjugated semiconductor thin film devices. *Phys. Rev. B* **72**, 205202 (2005).

40. Y. Sheng, T. D. Nguyen, G. Veeraraghavan, Ö. Mermer, M. Wohlgenannt, S. Qiu & U. Scherf, Hyperfine interaction and magnetoresistance in organic

semiconductors. *Phys. Rev. B* **74**, 045213 (2006).

41. P. Desai, P. Shakya, T. Kreouzis, W. P. Gillin, N. A. Morley & M. R. J. Gibbs, Magnetoresistance and efficiency measurements of Alq3-based OLEDs. *Phys. Rev. B.* **75**, 094423 (2007).

42. T. Ogiwara, Y. Wakikawa & T. Ikoma, Mechanism of intersystem crossing of thermally activated delayed fluorescence molecules. *J. Phys. Chem. A.* **119**, 3415–3418 (2015).

43. E. W. Evans, Y. Olivier, Y. Puttisong, W. K. Myers, T. J. H. Hele, S. M. Menke, T. H. Thomas, D. Credgington, D. Beljonne, R. H. Friend & N. C. Greenham, Vibrationally Assisted Intersystem Crossing in Benchmark Thermally Activated Delayed Fluorescence Molecules. *J. Phys. Chem. Lett.* **9**, 4053–4058 (2018).

44. D. Yokoyama, Molecular orientation in small-molecule organic light-emitting diodes. *J. Mater. Chem.* **21**, 19187 (2011).

45. S. Nowy, B. C. Krummacher, J. Frischeisen, N. A. Reinke & W. Brütting, Light extraction and optical loss mechanisms in organic light-emitting diodes: Influence of the emitter quantum efficiency. *J. Appl. Phys.* **104**, 123109 (2008).

46. S. Möller & S. R. Forrest, Improved light out-coupling in organic light emitting diodes employing ordered microlens arrays. *J. Appl. Phys.* **91**, 3324–3327 (2002).

47. E. Wrzesniewski, S. H. Eom, W. Cao, W. T. Hammond, S. Lee, E. P. Douglas & J. Xue, Enhancing light extraction in top-emitting organic light-emitting devices using molded transparent polymer microlens arrays. *Small*. **8**, 2647–2651 (2012).

48. R. Bathelt, D. Buchhauser, C. Gärditz, R. Paetzold & P. Wellmann, Light extraction from OLEDs for lighting applications through light scattering. *Org. Electron.* **8**, 293–299 (2007).

49. H. W. Chang, J. Lee, S. Hofmann, Y. Hyun Kim, L. Müller-Meskamp, B. Lüssem, C. C. Wu, K. Leo & M. C. Gather, Nano-particle based scattering layers for optical efficiency enhancement of organic light-emitting diodes and organic solar cells. *J. Appl. Phys.* **113**, 204502 (2013).

50. T.-B. Lim, K. H. Cho, Y.-H. Kim & Y.-C. Jeong, Enhanced light extraction efficiency of OLEDs with quasiperiodic diffraction grating layer. *Opt. Express*. **24**, 17950 (2016).

51. T. Schwab, C. Fuchs, R. Scholz, A. Zakhidov, K. Leo & M. C. Gather, Coherent mode coupling in highly efficient top-emitting OLEDs on periodically corrugated substrates. *Opt. Express*. **22**, 7524 (2014).

52. T. Komino, H. Tanaka & C. Adachi, Selectively controlled orientational order in linear-shaped thermally activated delayed fluorescent dopants. *Chem. Mater.* **26**, 3665–3671 (2014).

53. D. Yokoyama, A. Sakaguchi, M. Suzuki & C. Adachi, Horizontal orientation of linear-shaped organic molecules having bulky substituents in neat and doped vacuum-deposited amorphous films. *Org. Electron.* **10**, 127–137 (2009).

54. T. Komino, Y. Sagara, H. Tanaka, Y. Oki, N. Nakamura, H. Fujimoto & C. Adachi, Electroluminescence from completely horizontally oriented dye molecules. *Appl. Phys. Lett.* **108**, 241106 (2016).

55. S. Y. Kim, W. I. Jeong, C. Mayr, Y. S. Park, K. H. Kim, J. H. Lee, C. K. Moon, W. Brütting & J. J. Kim, Organic light-emitting diodes with 30% external quantum efficiency based on a horizontally oriented emitter. *Adv. Funct. Mater.* **23**, 3896–3900 (2013).

56. D. R. Lee, B. S. Kim, C. W. Lee, Y. Im, K. S. Yook, S. H. Hwang & J. Y. Lee,

Above 30% external quantum efficiency in green delayed fluorescent organic light-emitting diodes. *ACS Appl. Mater. Interfaces*. **7**, 9625–9629 (2015).

57. Y. Hasegawa, Y. Yamada, M. Sasaki, T. Hosokai, H. Nakanotani & C. Adachi, Well-Ordered 4CzIPN ((4s,6s)-2,4,5,6-Tetra(9-H-carbazol-9-yl)isophthalonitrile) Layers: Molecular Orientation, Electronic Structure, and Angular Distribution of Photoluminescence. *J. Phys. Chem. Lett.* **9**, 863–867 (2018).

Chapter 2

Effect of carrier balance on device degradation of organic light-emitting diodes based on thermally activated delayed fluorescence emitters

Masaki Tanaka, Hiroki Noda, Hajime Nakanotani and Chihaya Adachi

Advanced Electronic Materials, **5**, 1800708 (2019)

Abstract

The relatively short device lifetime of blue OLEDs when compared with the lifetimes of green and red OLEDs is one of the crucial problems that must be overcome to enable practical application of these devices to full-color OLED displays. This work focuses on the degradation phenomena of OLEDs that are based on sky-blue TADF emitters and clarifies the degradation mechanisms based on spectral change of the electroluminescence, which indicates the formation of electromer emission from an electron transport layer. Additionally, it is determined that the change in the carrier balance that occurs during this degradation process can be ascribed to the formation of electron traps.

2-1. Introduction

OLEDs have been attracting considerable attention in recent years because they offer the possibility of low-cost fabrication of flexible and lightweight devices with high EL efficiency[1]. A wide variety of emitters have been developed for OLEDs to enhance their IQE, and one of most important factors in obtaining the ultimate IQE is the ratio of singlet to triplet exciton generation *via* carrier recombination. Purely aromatic compounds that exhibit TADF are promising candidate materials for realization of the ultimate EL efficiency at low cost because TADF can harvest triplet excitons in the form of light without use of rare metals such as iridium and platinum[2,3]. In fact, the small energy split between the lowest excited singlet state and the lowest excited triplet state (ΔE_{ST}) promotes efficient spin conversion between the singlet excitons and the triplet excitons and the converted singlet excitons can then emit light as delayed fluorescence with nearly 100% quantum efficiency. However, the device stability of blue TADF-OLEDs during continuous operation is still very short when compared with that of state-of-the-art blue OLEDs based on fluorescent or phosphorescent emitters[4,5].

To date, there have been a number of important reports on degradation mechanisms and strategies to enhance the device lifetimes of OLEDs have also been proposed[6–14]. Kondakov and Noguchi *et al.* both reported that the charge carrier recombination that occurs close to an interface between an emission layer (EML) and an adjacent transport layer can cause unpredictable chemical reactions between these molecules, which then leads to exciton quenching by the accumulated charge carriers[7,8]. Nakanotani *et al.*, also reported that shifting of the carrier recombination site from an interface into the bulk of the EML significantly enhanced the device lifetimes of TADF-OLEDs[4]. Furthermore, Zhang *et al.* reported that a device architecture using a gradually

doped EML in blue phosphorescent OLEDs can achieve a tenfold increase in the device lifetime because of the resulting control of the emission zone and the triplet exciton density inside the EML[9]. Therefore, to improve the device stability, spatial separation of the emission zone from the heterointerfaces is an important issue to reduce the encounter frequency between the excitons and quenching species[11–14].

To suppress unwanted interactions between the triplet excitons and quenching species such as trapped charge carriers, the triplet exciton lifetime of the emitters should be managed carefully because the rates of the exciton annihilation processes are critically dependent on the triplet exciton density. TADF molecules, which basically have long exciton lifetimes, consist of bridged donor-acceptor moieties and the combination of these moieties can affect the exciton lifetime[15,16]. Noda *et al.*, recently reported that insertion of different donor units into a parent benzonitrile-carbazole (CzBN) type molecule such as penta(9H-carbazol-9-yl)benzonitrile (5CzBN) shown in **Figure 2-1** was effective in shortening the triplet exciton lifetime and successfully improved both the EQE rolloff and the device's operational stability based on 2,4,6-tris(9H-carbaozle-9-yl)-3,5-bis(3,6-diphenylcarbazole-9-yl)benzonitrile (3Cz2DPhCzBN)[17]. While it was proposed that the improvement in the device's operational lifetime was caused not only by the short triplet lifetime but also by the change in the carrier transport abilities of the TADF molecules, the detailed mechanism that is responsible for the significant observed improvement in the operational lifetime remains unclear.

Here, I show that the short triplet-exciton lifetime of the TADF emitters suppresses carrier trap generation *via* reduction of the exciton-polaron interactions. In this work, I analyze the degradation mechanism of TADF-OLEDs based on CzBN-type TADF emitters by investigating the EL spectral change that occurs during device degradation.

In particular, I show that the OLED emits an unpredicted red emission after degradation. I determined that this unpredicted red emission originated from an electromer located in a hole-blocking layer (HBL) that is only observable under electrical excitation. This behavior directly demonstrates the existence of cation species of the hole-blocking material that are caused by hole current leakage from the EML without recombination.

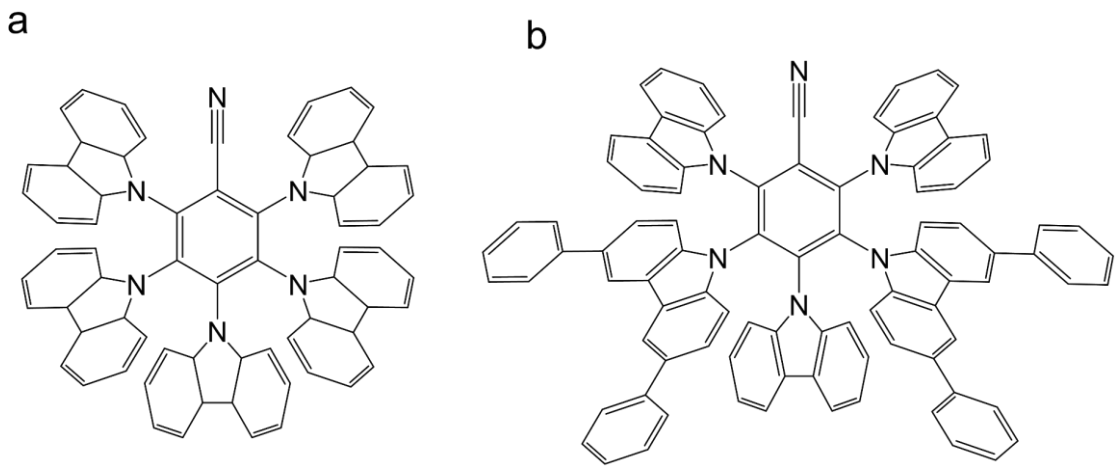

Figure 2-1. Molecular structures of (a) 5CzBN and (b) 3Cz2DPhCzBN.

2-2. Experimental

2-2-1. Sample fabrication

The TADF-OLEDs were fabricated by vacuum vapor deposition processes without exposure to ambient air. After fabrication, the devices were immediately encapsulated under a glass cover using epoxy glue in a nitrogen-filled glovebox (H_2O > 0.1 ppm, O_2 > 0.1 ppm). The OLED structure is ITO (100 nm) / HAT-CN (10 nm) / Tris-PCz (30 nm) / mCBP (5 nm) / EML (30 nm) / SF3-TRZ (10 nm) / 30 wt.% Liq:SF3-TRZ (50 nm) / Liq (2 nm) / Al (100 nm), where, in turn, the internal layers other than the EML correspond to a hole-injection layer (HIL), a hole-transporting layer (HTL), an electron-blocking layer (EBL), a hole-blocking layer (HBL), a Liq-doped electron-transporting layer (ETL)[18,19], and an electron-injection layer (EIL), respectively. HAT-CN, Tris-PCz, mCBP, SF3-TRZ[20], and Liq are 1,4,5,8,9,11-hexaazatriohenyleane hexacarbonitrile, 9,9'-diphenyl-6-(9-phenyl-9H-carbazol-3-yl)-9H,9'H-3,3'-bicarbazole, 3,3'-di(9*H*-carbazol-9-yl)-1,1'-biphenyl, 2-(9,9'-spirobi[fluoren]-3-yl)-4,6-diphenyl-1,3,5-triazine, and 8-hydroxyquinolinolato-lithium, respectively (**Figure 2-2**). The EMLs were formed by co-deposition of 20 wt.% TADF emitters and mCBP.

The device structure of the hole-only device (HOD) was ITO (100 nm) / HAT-CN (10 nm) / Tris-PCz (30 nm) / mCBP (5 nm) / 20 wt.% TADF emitter:mCBP (30 nm) / mCBP (5 nm) / Tris-PCz (30 nm) / HAT-CN (10 nm) / Al (100 nm). The device structure of the electron-only device (EOD) was ITO (100 nm) / LiF (0.8 nm) / SF3-TRZ (35 nm) / 20 wt.% TADF emitter:mCBP (30 nm) / SF3-TRZ (35 nm) / LiF (0.8 nm) / Al (100 nm). The single layer EL devices were fabricated using the following structure: ITO (100 nm) / MoO_3 (10 nm) / organic layer (100 nm) / LiF (0.8 nm) / Al (100 nm). Here, organic materials comprising Tris-PCz, mCBP, and SF3-TRZ were used.

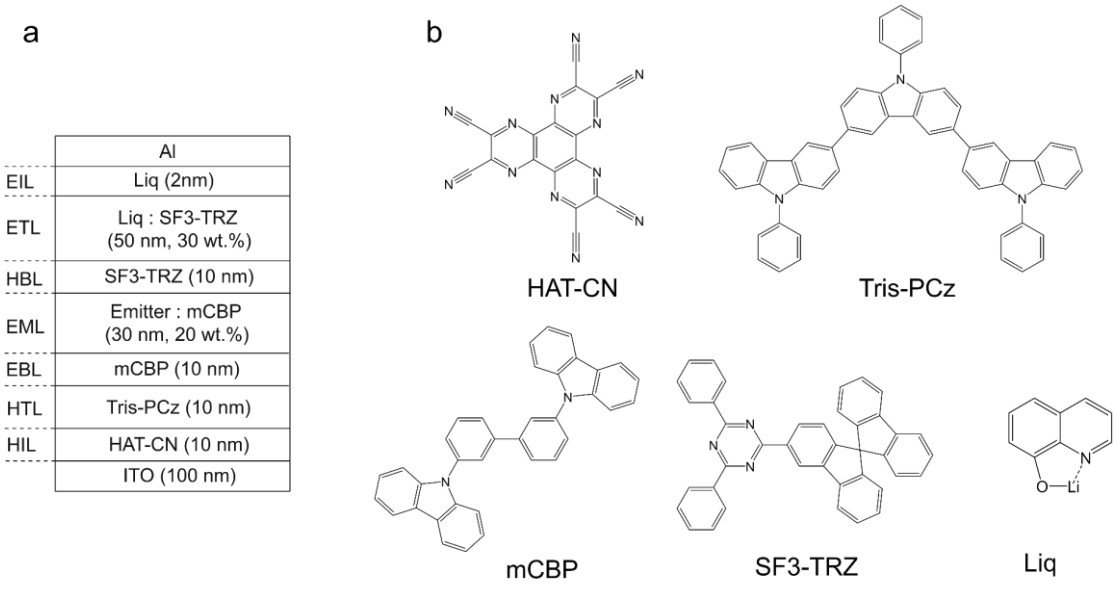

Figure 2-2. (a) OLED device structure, (b) molecular structures of HAT-CN, Tris-PCz, mCBP, SF3-TRZ and Liq.

All organic layers, except for the Liq layers, were deposited at a deposition speed of 0.1 nm/s, while the Liq layer was deposited at 0.03 nm/s. The deposition rates of LiF and Al were fixed at 0.01 nm/s and 0.1 nm/s, respectively. While the device area is approximately 0.04 cm^2, devices with areas of 0.01 cm^2 were fabricated for the transient EL measurements to minimize the effect of the resistance-capacitance (RC) constant.

2-2-2. Sample characterization

The EQE and current density (J) -voltage (V) -luminance (L) measurements were performed using a calibrated luminance meter (CS-2000, Konica Minolta). For the device lifetime tests, the luminance and EL spectra of the driving devices in the normal direction were measured using a luminance meter (SR-3AR, TOPCON) under constant current density driving conditions with an initial luminance of 1,000 cd m^{-2}. The HODs and EODs were evaluated at constant current densities of 1 mA cm^{-2} and 0.1 mA cm^{-2}, respectively. For analysis of the exciton-polaron interaction, UV light (5 mW cm^{-2}) within

the wavelength range from 300 nm to 400 nm from a xenon light source (MAX-303, Asahi Spectra) transmitted through a band-pass filter was used to irradiate the HODs and EODs. For the displacement current measurement (DCM), five repeated-triangular voltage signals were applied to each device using a function generator (WaveStation 2052, Teledyne Lecroy) and the displacement current was amplified using a current amplifier (CA5350, NF). The applied voltage and the amplified current were measured using an oscilloscope (HDO4054A, Teledyne Lecroy). The applied voltage signal ranged from −4 V to 4 V and the scan rate was 100 V s^{-1}. For the transient EL measurements, pulsed voltages were applied using a function generator. The emitted light was detected using a photomultiplier tube (PMT) module (H10721-01, Hamamatsu Photonics) through a short-pass filter with an operating wavelength of 550 nm and the current signals from the PMT were amplified using a current amplifier (DHPCA-100, Femto). All signals were measured using an oscilloscope with signal averaging performed over 1000 measurements.

The thin film samples were fabricated on a quartz substrate by vacuum vapor deposition to enable measurement of the photoluminescence quantum yield (PLQY) values and decay times of the TADF emitters. The PLQY values were measured using the Quantaurus-QY system (C11347-11, Hamamatsu Photonics) in flowing argon gas at an excitation wavelength of 340 nm. The transient PL decay profiles were recorded using the Quantaurus-Tau system (C11367-03, Hamamatsu Photonics) in ambient air.

To evaluate the dipole orientations of the TADF emitters in doped films, 15-nm-thick doped films were deposited on glass slides (refractive index: n = 1.52). Angular-dependent PL measurements were conducted using the C14234-01 measurement system (Hamamatsu Photonics) at an excitation wavelength of 365 nm and the order parameters

were determined by fitting of the profiles using Setfos 4.6 software (Fluxim).

Cyclic voltammetry measurements were performed using an electrochemical analyzer (ALS608D, BAS) with a platinum counter electrode, a glassy carbon working electrode and a silver reference electrode. The solvent used was *N*,*N*-dimethylformamide (DMF) with TBAPF6 acting as the supporting electrolyte; the solution concentration was less than 10^{-5} M because of the low solubility of DMF. The sweep rate used for the measurements was 0.01 V s^{-1}.

EL spectra with different dipole positions in the EML were simulated using Setfos 4.6 software (Fluxim). The refractive index values of each layer that were required for the simulations were estimated *via* ellipsometry measurements.

2-3. Results and discussion

2-3-1. Device performance of TADF-OLEDs

In this study, two TADF molecules were used as the doped emitters: 5CzBN and 3Cz2DPhCzBN. 3Cz2DPhCzBN has a partially modified 5CzBN structure and this modification results in slightly red-shifted photoluminescence (PL) and a shorter decay time for the delayed PL component when compared with that of 5CzBN acting as a sky blue emitter. For co-deposited films, *i.e.*, where the TADF emitters of 5CzBN and 3Cz2DPhCzBN were doped in a single mCBP layer, they had PL decay times of 12.5 μs and 5.6 μs and PL emission peak wavelengths of 482 nm and 494 nm, respectively (**Figure 2-3**).

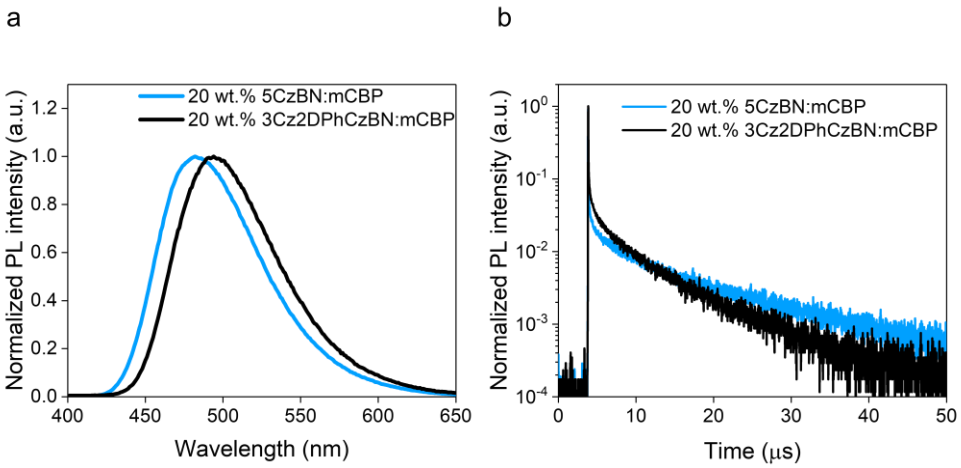

Figure 2-3. (a) Normalized PL spectra and (b) transient PL decay profiles of 5CzBN and 3Cz2DPhCzBN films doped in mCBP.

Although 2,4,6-tris(3,6-diphenylcarbazole-9-yl)-3,5-(9H-carbazole-9-yl)benzonitrile (2Cz3DPhCzBN) reported in Ref. 17 shows much shorter delayed lifetime than that of 3Cz2DPhCzBN, 2Cz3DPhCzBN has significantly larger difference of the energy gap compared to those of 5CzBN and 3Cz2DPhCzBN. Therefore, 3Cz2DPhCzBN was adopted as a doped emitter for the comparison of 5CzBN in this study. In addition, I

note that SF3-TRZ is an electron-transport material with the electron mobility of 7.0×10^{-5} cm^2 V^{-1} s^{-1} and relatively high glass transition temperature of 135 °C[20].

Figures 2-4a,b and **c** show the *J*-*V*-*L* characteristics, the *J*-EQE profiles and the EL spectra, respectively, for each fabricated OLED. The differences among the maximum EQE values for each OLED can be explained by the difference between the PL quantum yields (η_{QY}) of the emitters, which are 74% for 5CzBN and 86% for 3Cz2DPhCzBN, and a difference between their light-outcoupling efficiency (η_{OC}) values because the order parameter of the transition dipole moment vector (S)[21] for 3Cz2DPhCzBN (S = −0.20) showed a slightly higher horizontal orientation than that of 5CzBN (S = −0.13) (**Figure 2-5**).

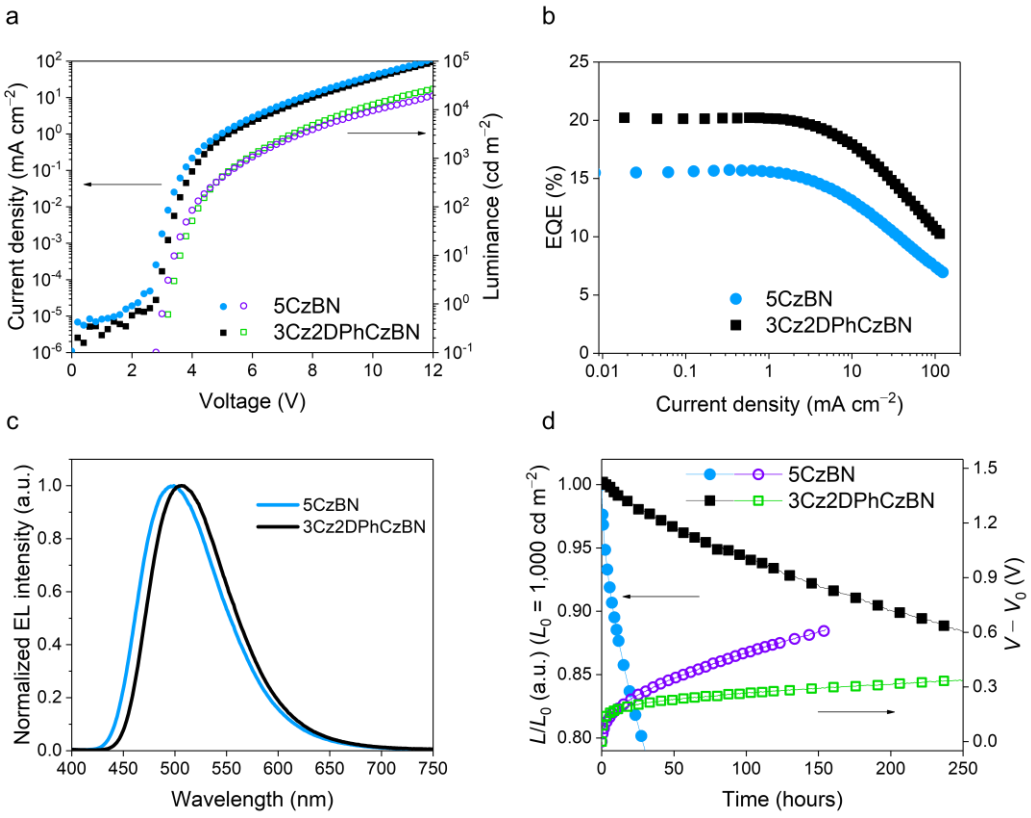

Figure 2-4. (a) *J*-*V*-*L* characteristics, (b) *J*-EQE characteristics, (c) normalized EL spectra and (d) luminance decay curves (L/L_0) and driving voltage differences ($V-V_0$) for the devices based on 5CzBN and 3Cz2DPhCzBN.

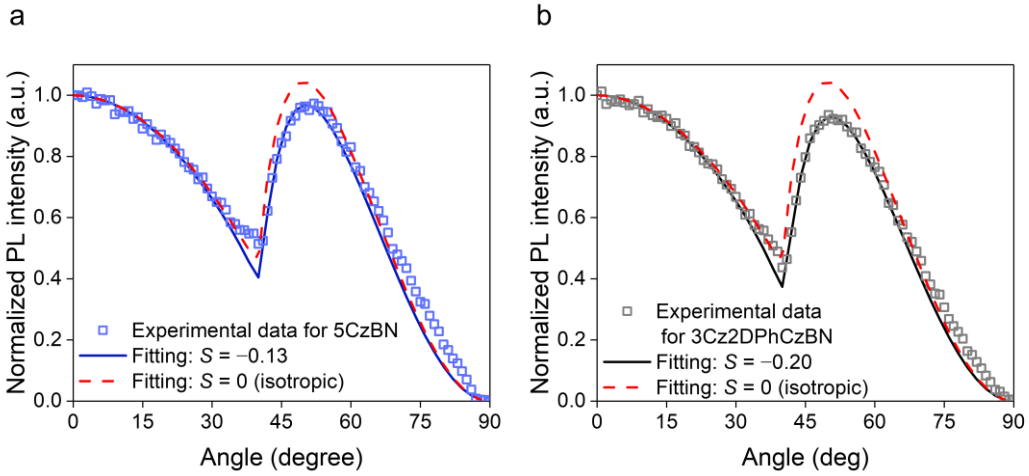

Figure 2-5. Angular-dependent PL profiles of films of (a) 20 wt.% 5CzBN:mCBP and (b) 20 wt.% 3Cz2DPhCzBN:mCBP.

Device lifetime tests were also conducted at the constant current densities for these two emitters (J = 2.9 mA cm^{-2} and 1.7 mA cm^{-2}, respectively) that were responsible for the initial luminance of 1,000 cd m^{-2}. The LT_{90} (which is the time at which the luminance decreases to 90% of the initial luminance) values for the 5CzBN- and 3Cz2DPhCzBN-based OLEDs are 7.9 h and 201 h, respectively (**Figure 2-4d**). The 3Cz2DPhCzBN-based OLED shows an LT_{90} that is approximately 25 times longer than that of the 5CzBN-based OLED, and this result clearly indicates that the partially modified TADF emitter with the shorter exciton lifetime is useful in improving device stability, as reported in Ref. 17. Note that the slight difference between the lifetime characteristics in this study and those in the previous study can be ascribed to the different fabrication conditions used.

2-3-2. Investigation of EL spectral change during device operation

2-3-2-1. Origin of blue shift of TADF emission

To discuss the degradation processes of each OLED, the EL spectral changes were monitored. The normalized EL spectra and their dependence on driving time are shown in **Figures 2-6a** and **b**. In the case of the 5CzBN-based OLED, unpredicted red emission emerged gradually over time. In contrast, in the case of the 3Cz2DPhCzBN-based OLED, the appearance of this red emission is strongly suppressed. To confirm the changes in these spectral shapes in more detail, the difference spectra, ΔI_{EL} ($I_{EL,normalized}$ (t) − $I_{EL,normalized}$ (0)), are shown in **Figures 2-6c** and **d**. From these spectra, two unique behaviors can be identified. The first is the occurrence of the red emission and the second is the presence of an isosbestic point at around 500 nm, which indicates a blue shift in the EL spectra during device degradation. The spectral shifts of these OLEDs under constant conditions indicate changes in the carrier recombination zones in their EMLs during device degradation[22].

To evaluate the relationship between the spectral shift and the emission position, optical simulations using Setfos 4.6 were performed (**Figure 2-7a**). The simulation results for the 5CzBN-based OLED indicates that the blue shift in the EL spectra corresponds to a shift in the emission position from the anode side to the cathode side, thus indicating that the exciton density at the EML/HBL interface gradually increases during device degradation. The difference spectra that were calculated based on the optical simulation by varying the emission position (**Figure 2-7g**) follow the experimental results well, as shown in **Figures 2-6c** and **d**.

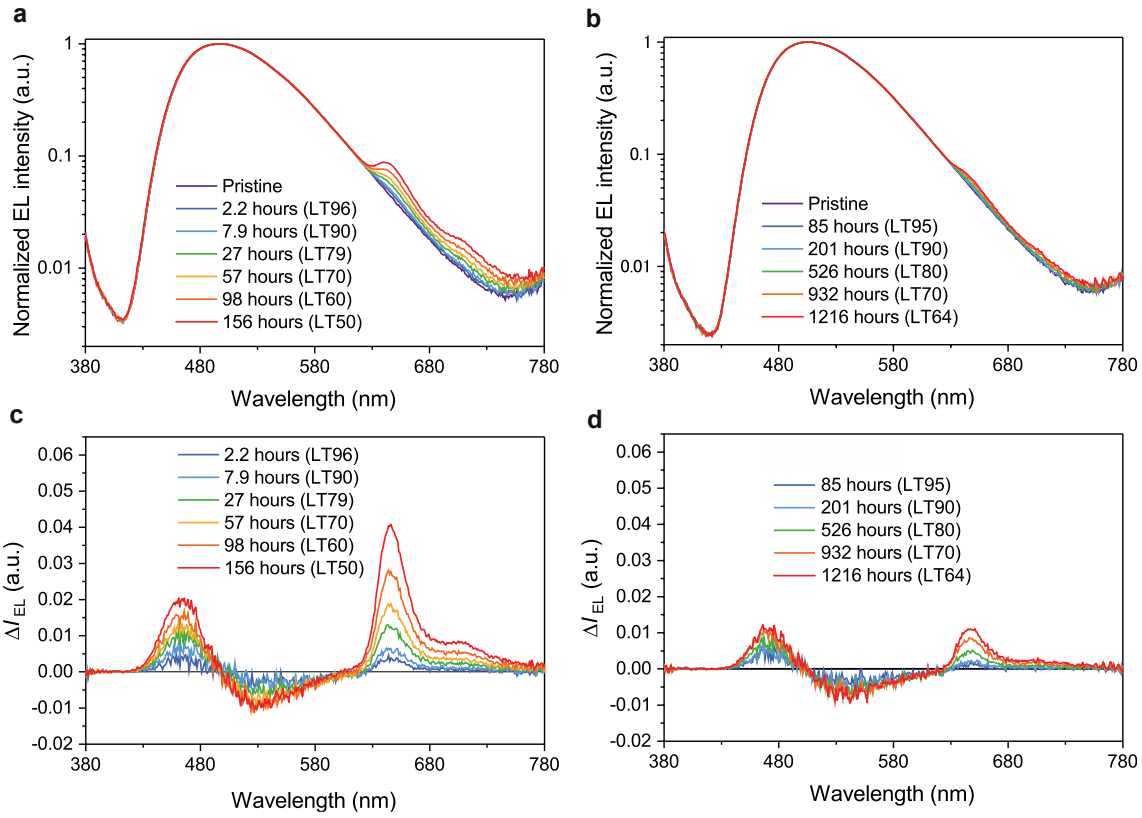

Figure 2-6. Normalized EL spectra of (a) 5CzBN-based OLED and (b) 3Cz2DPhCzBN with various driving times. Difference spectra of (c) 5CzBN-based OLED and (d) 3Cz2DPhCzBN-based OLED during degradation.

A blue shift in the EL spectrum with increasing current density was even observed in the fresh device (**Figure 2-7b**), indicating that the recombination area in the EML gradually shifts away from the EBL-side towards the HBL-side. These EL spectral shifts were also confirmed in other OLEDs with greater EML thicknesses of 50 and 70 nm (**Figures 2-7c-f**). Furthermore, optical simulations indicate that the recombination zone under 1 mA cm^{-2} that is comparable to the actual current densities before degradation is located near the center of the EML. Based on the EL spectral changes observed during degradation, the exciton distribution in the EML is believed to shift as follows: in the initial stage, the excitons are rather widely distributed within the EML, with the peak density occurring at near the center of the EML; this peak density then gradually shifts

toward the HBL interface during device degradation, which results in a relatively high exciton density close to the EML/EBL interface. The details of the degradation process will be discussed based on the process shown in **Figure 2-15**.

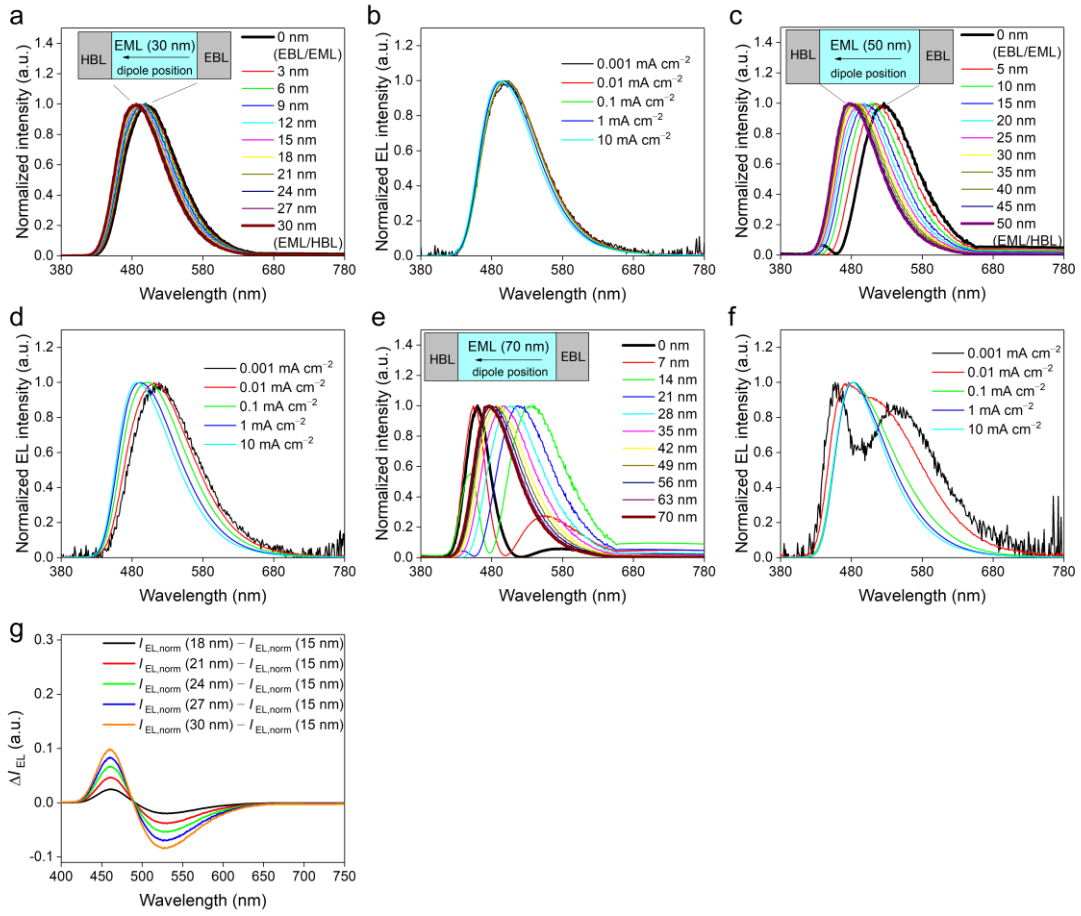

Figure 2-7. Results of optical simulations for various dipole positions in the EML and the EL spectral dependence on current density and the EML thickness of 5CzBN-based OLEDs. (a), (c), and (e) Results of optical simulations of OLEDs with different EML thicknesses (30, 50, and 70 nm). The inset shows a simple illustration of the correlation between spectrum and dipole position in the EML. (b), (d), and (f) Normalized EL spectra of 5CzBN-based OLEDs with different EML thicknesses (30, 50, and 70 nm). (g) Difference spectra calculated from the simulation results (**Figure 2-7a**). These spectra were calculated as the difference between the normalized spectra, $I_{\mathrm{EL,norm}}(x)$ and $I_{\mathrm{EL,norm}}$ (15 nm), where x is the emissive dipole position.

2-3-2-2. Origin of unpredicted red emission

Next, I discuss the origins of the unpredicted red emission from the OLED. First, the PL spectra of each of the materials constituting the OLEDs were confirmed (**Figure 2-8**). However, no red-emission components were observed from these films under optical excitation.

In addition, the EL spectra of each single layer were also investigated because I supposed that the red emission would only occur under electrical excitation[23,24]. The device structure of the single-layer device is as follows: ITO (100 nm) / MoO_3 (10 nm) / organic layer (100 nm) / LiF (0.8 nm) / Al (100 nm) (**Figure 2-9a**). **Figure 2-9b** shows summarized PL and EL spectra for each of the materials and obviously indicates that the red emission originates from the SF3-TRZ layer under EL condition.

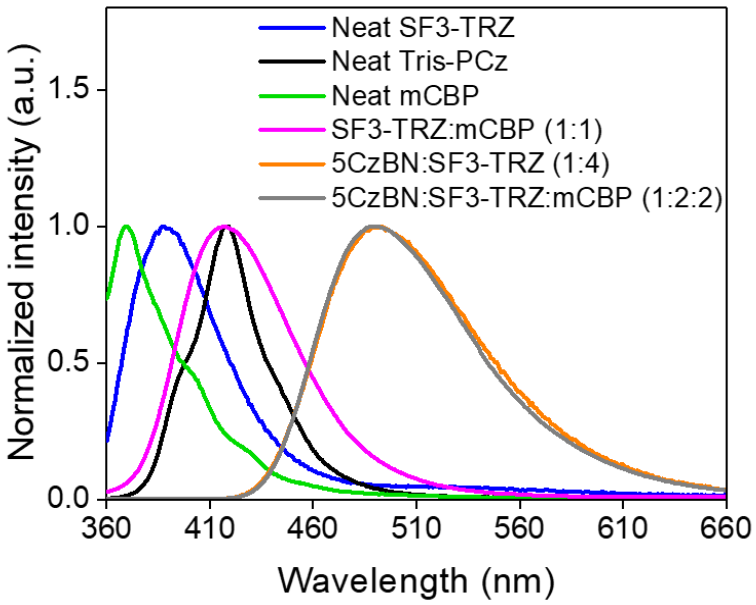

Figure 2-8. Normalized PL spectra of films of neat SF3-TRZ, neat Tris-PCz, neat mCBP, 50 wt.% SF3-TRZ:mCBP, 20 wt.% 5CzBN:SF3-TRZ and 20 wt.% 5CzBN:40 wt.% SF3-TRZ:40 wt.% mCBP.

Because the red emission was only observed under electrical excitation, I speculate that the red EL can be attributed to electromer emission, as reported by Kalinowski *et al.*[23] Electromer emission was previously ascribed to dimer emission processes occurring among molecules with a tritolylamine unit, such as 4,4'-cyclohexylidenebis[N,N-bis(4-methylphenyl)benzamine] (TAPC), which can only be observed under electrical excitation. While the origin of the electromer emission remains unclear, it is proposed that the electromer emission comes from cross-transition recombination occurring between the anion and cation species of identical organic molecules[25]. Therefore, the occurrence of the electromer emission provides direct evidence for the existence of the SF3-TRZ cation species in the aged OLEDs.

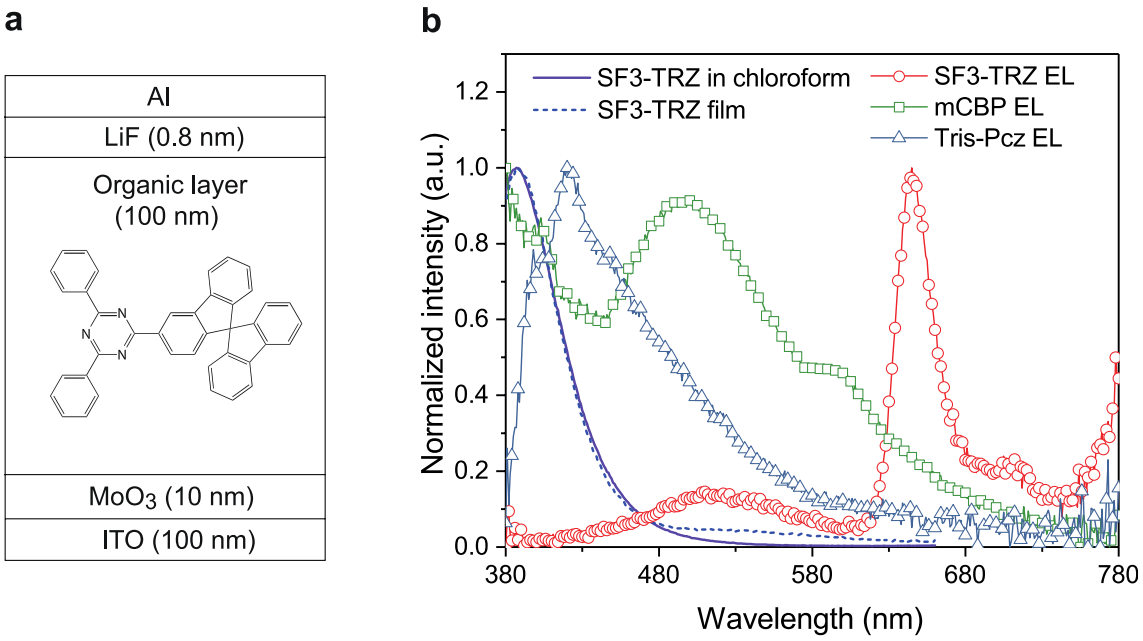

Figure 2-9. (a) Device structure of single layer OLEDs. SF3-TRZ, mCBP, and Tris-PCz layers were used as 100-nm-thick organic layers. The inset shows the molecular structure of SF3-TRZ. (b) PL and EL spectra of each organic material. Purple and broken blue lines indicate the PL spectra of a SF3-TRZ solution in chloroform (10^{-5} M) and a vacuum-deposited SF3-TRZ film, respectively. Red circles, green quadrangles, and blue triangles indicate the EL spectra of single layer OLEDs based on SF3-TRZ, mCBP, and Tris-PCz, respectively.

Additionally, the existence of the SF3-TRZ cation species means that the hole carriers that are transported in the EML reach the HBL/EML interface and the injection of holes into the HBL subsequently occurs, resulting in carrier recombination in SF3-TRZ with a decrease in the EQE. These two experimental observations, *i.e.*, the blue shift in the TADF emission and the emergence of the electromer emission, provide positive evidence for a change in the carrier balance during device operation. I note here that the exciton quenching processes in the EML are not the dominant factor in the drop in luminance[26] because the EL decay constants for each OLED based on transient EL measurements are almost the same (**Figure 2-10**).

In contrast to the 5CzBN-based OLED, the increase in the electromer emission was suppressed well in the 3Cz2DPhCzBN-based OLED during device ageing, thus indicating superior device stability. In general, the electron transport properties in the EMLs of TADF-OLEDs are strongly dependent on the charge carrier transport abilities of the TADF molecules because of the rather high doping concentration (20 wt.% in this work) combined with the lowest unoccupied molecular orbital (LUMO) energy level of the TADF molecules being lower than that of the host materials, which resulted in the electron transport by the TADF molecules being dominant[4]. Therefore, the change in the carrier balance during device operation implies differences in the carrier transport stabilities of the EMLs, *i.e.*, in the 5CzBN or 3Cz2DPhCzBN:mCBP films.

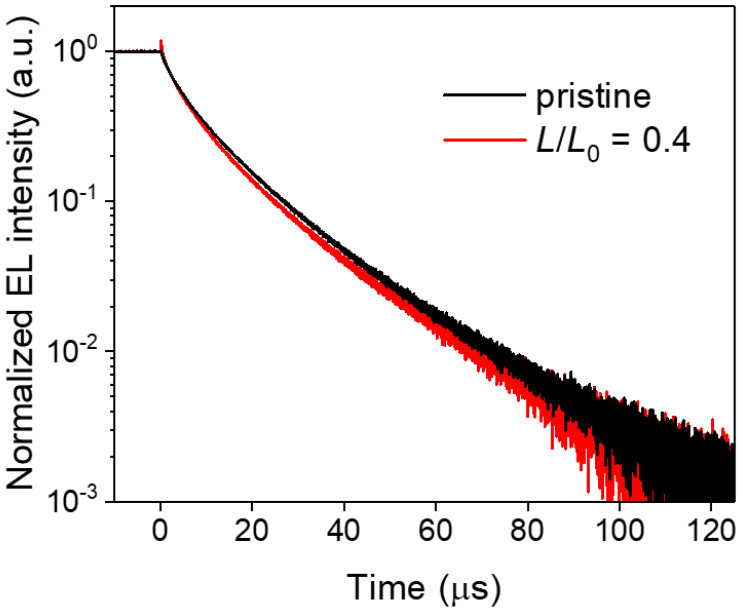

Figure 2-10. Transient EL decay curves of 5CzBN-based OLEDs before and before degradation with on-voltage related to 3 mA cm^{-2}. An off-voltage was −10 V to promote to de-trap of trapped charge carriers in the devices.

2-3-3. Investigation of carrier transport dynamics in EML

2-3-3-1. Studies for evaluation of carrier trap generation

To evaluate the charge carrier transport abilities of the co-deposited films, operational stability tests of both HODs and EODs were performed (**Figure 2-11**). I also examined the performance of these devices under UV irradiation to understand the effects of the photo-generated excitons. In the case of the HOD test results presented in **Figure 2-11a**, the changes in the driving voltage (ΔV) under a constant current density (J = 1 mA cm^{-2}) in each TADF molecule were not significant, regardless of the light irradiation. In case of the EOD test results, however, the ΔV of the 5CzBN-based EOD (J = 0.1 mA cm^{-2}) was much larger than that of the 3Cz2DPhCzBN-based EOD under UV irradiation (**Figure 2-11b**).

Furthermore, when compared with the case of zero current stress under UV irradiation (indicated by the square symbols in **Figure 2-11b**), the increase in ΔV in the EODs under both current and UV stresses was quite pronounced, thus indicating that the exciton-polaron interaction promotes the generation of deep electron traps[27,28]. These results indicate that the electron transport ability of the 5CzBN-doped EML decreases during device operation. One possible electron-trap formation mechanism is decomposition of the 5CzBN and mCBP in the doped EML caused by the formation of higher state polarons through triplet-polaron annihilation process.

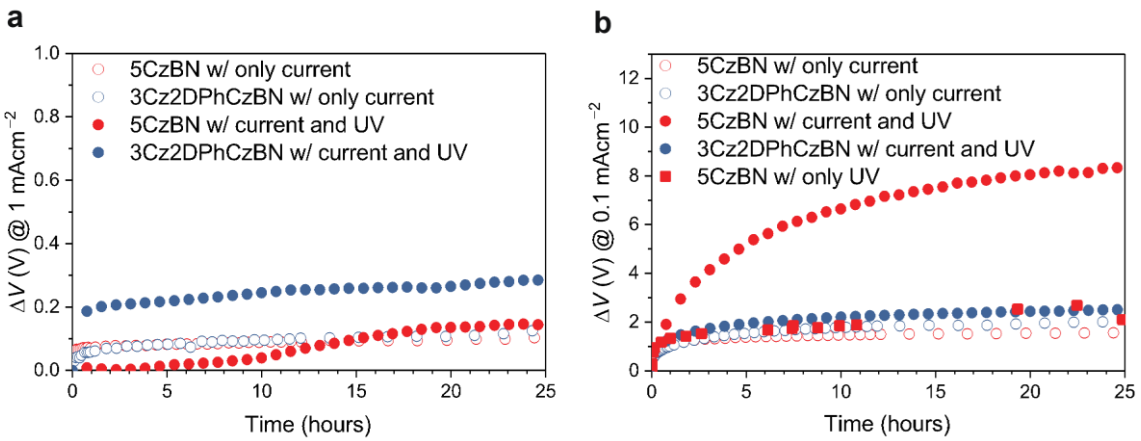

Figure 2-11. (a) Results of the HOD tests. (b) Results of the EOD tests. Red and Blue opened circles represent results for devices based on the 5CzBN and 3Cz2DPhCzBN emitter materials under continuous current stress (HOD: 1 mA cm^{-2}; EOD: 0.1 mA cm^{-2}) without UV irradiation, respectively. Red and blue filled circles represent the conditions of the corresponding devices under continuous current and UV stress, respectively. Red quadrangles represent the results obtained under continuous UV stress for the measured voltage at periodic intervals.

2-3-3-2. Carrier transport in OLEDs and luminance drop mechanism

To investigate the carrier dynamics in OLEDs, a capacitance analysis was performed *via* the displacement current measurement (DCM) method[8] (**Figure 2-12**). Five triangle-voltage signals were continuously applied to the devices before and after degradation. In the fresh device case shown in **Figures 2-12a** and **b**, the DCM signals of the OLEDs with both 5CzBN and 3Cz2DPhCzBN showed plateau characteristics, suggesting that carrier injection and subsequent accumulation occurred in both devices. Because of the complex multi-layered structures of these OLEDs with their highly conductive HAT-CN and Liq-doped layers, the accumulation position cannot be calculated using the capacitance value on the plateau; however, this plateau is the result of electron injection and accumulation near the interface between the EBL and the EML, as can be confirmed by the results from OLEDs with various thicknesses for each organic layer.

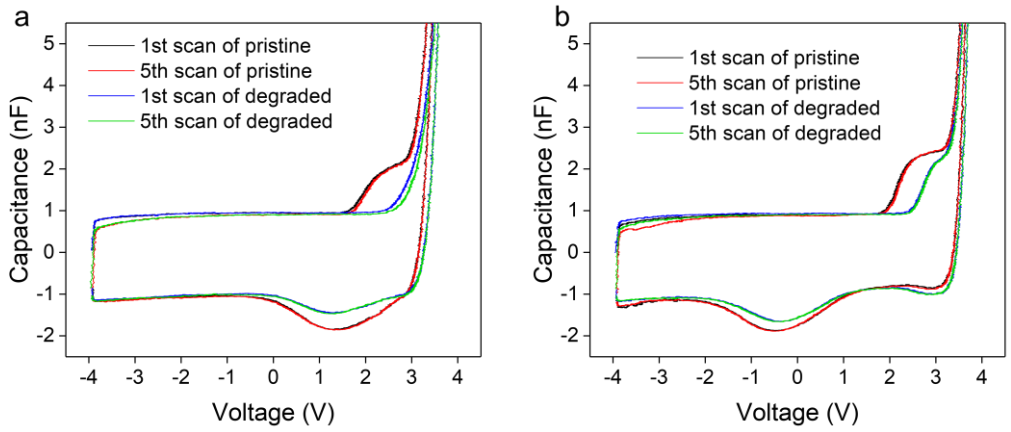

Figure 2-12. DCM profiles of the devices based on (a) 5CzBN before degradation and after driving for 3.5 hours, (b) 3Cz2DPhCzBN before degradation and after driving for 5 hours. Black and purple lines show the 1st and the 5th scans of the pristine devices. Blue and orange lines show the corresponding scans of degraded devices. Before the 1st scan, −10 V was applied to the devices for 10 s for de-trapping.

Furthermore, the DCM profiles of the 1st and the 5th scans were almost identical, thus indicating that the trapped electrons in the pristine devices can easily be de-trapped during the measurement cycle. Note that the devices were biased at −10 V for 10 s before the 1st scan to de-trap any unwarranted carriers. After the degradation of the OLEDs, the electron injection and accumulation processes in the 5CzBN-based OLED were suppressed well and the voltages of the rising capacitances in the 1st and 5th scans were appreciably different (**Figure 2-12a**), suggesting that generated deep electron traps affect the carrier dynamics in the 5CzBN-based OLED.

In contrast to the 5CzBN-based OLED, the DCM signals from the 1st and 5th scans of the degraded 3Cz2DPhCzBN-based OLED were almost identical, indicating that deep electron traps, which cannot be de-trapped during the measurement cycle, were not generated in this device (**Figure 2-12b**). I thus inferred that the deep electron traps were formed in the EML of the 5CzBN-based OLED during device aging which originates from the triplet exciton-polaron interaction (TPI) as mentioned above.

The reason why the electron transport ability of 3Cz2DPhCzBN remains stable, even after excitation by both light irradiation and current flow, appears to be a lower probability of interaction between excitons and the anions of 3Cz2DPhCzBN because it has a shorter exciton lifetime than 5CzBN. Another possible reason may be differences in the chemical stabilities of these TADF emitters in their anion states, where the capping by a phenyl unit at the 3, 6-position of the carbazoles surely affects the chemical reactivity. To evaluate the electrochemical stabilities of these emitters, cyclic voltammetry measurements were performed in an *N*,*N*-dimethylformamide solution (**Figure 2-13**). While there were small signals because of the low solubility of these materials, clear reversible signals occurring at around −2.0 V vs. Fc/Fc^+ (ferrocene) could be observed in

each molecule. These results suggest no significant differences in the stability of the anion state in both 5CzBN and 3Cz2DPhCzBN and the shorter exciton lifetime of 3Cz2DPhCzBN would therefore represent a possible mechanism for the stability enhancement.

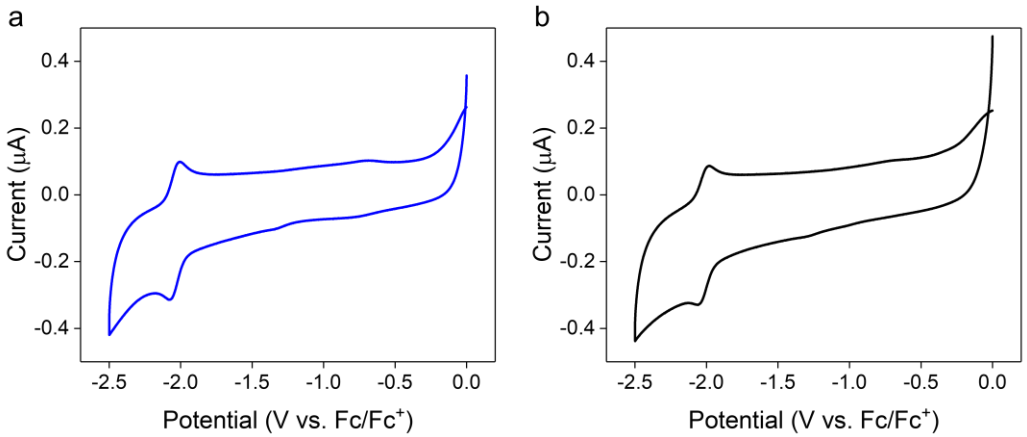

Figure 2-13. Results of cyclic voltammetry measurements of TADF molecules. (a) 5CzBN solution and (b) 3Cz2DPhCzBN solution in *N*,*N*-dimethylformamide.

Additionally, it must also be clarified whether the electron-transport properties of the SF3-TRZ layer are degraded by the injected holes and the subsequent formation of the electromers. According to the report of Kwon *et al.*, electron injection into a TAPC film causes the formation of the electromers that leads to the formation of defect sites and inferior device performances[29]. To evaluate the irreversibility of electromer formation in a SF3-TRZ film, OLEDs were fabricated without the EML and the EBL and *J*-*V*-*L* measurements of these devices were performed repeatedly (**Figure 2-14**). Here, the holes are injected directly from a Tris-PCz layer to the SF3-TRZ layer, resulting in more efficient electromer emission than that in conventional OLEDs. The voltage ranges used for these *J*-*V*-*L* measurements were (a) from −2 V to +12 V and (b) from −2 V to +6 V to enable investigation of the dependence of the results on the number of holes injected into

the SF3-TRZ layer. In the case of measurement condition (a), the EL intensity of the electromers increased with measurement time, indicating that the injected holes and the emerging electromers would damage the SF3-TRZ layer. In contrast, in the case of measurement condition (b), no change was observed in the overall emission shape, indicating that low or zero electromer formation would not induce serious damage. In the case of the pristine OLEDs, no obvious electromer emissions were observed. Therefore, if the electron transport properties of the EML are efficient and small numbers of holes arrive at the interface between the EML and the HBL, no degradation of the SF3-TRZ occurs. I therefore propose that the rapid luminance drop in the 5CzBN-based OLED during continuous operation was caused by the inferior electron transport stability of its EML and this would lead to the change in the carrier balance and subsequent hole current leakage into the HBL (**Figure 2-15**).

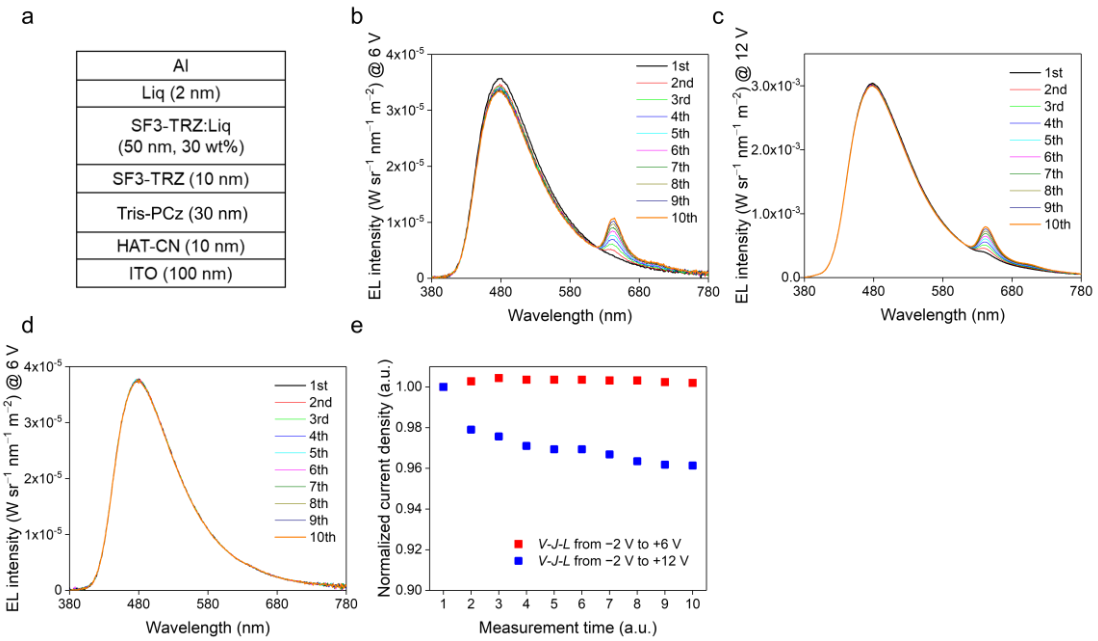

Figure 2-14. Results of repeated *J-V-L* measurements to investigate the reversibility of the electromer emission and formation processes. (a) Device structure of OLED without EML and EBL. (b) EL spectra (not normalized) at 6 V for each measurement time in the measurement range from −2 V to +12 V. (c) EL spectra at 12 V for each measurement time in the measurement range from −2 V to +12 V. (d) EL spectra at 6 V for each measurement time in the measurement range from −2 V to +6 V. (e) Normalized current density at 6 V versus *J-V-L* measurement time for both measurements.

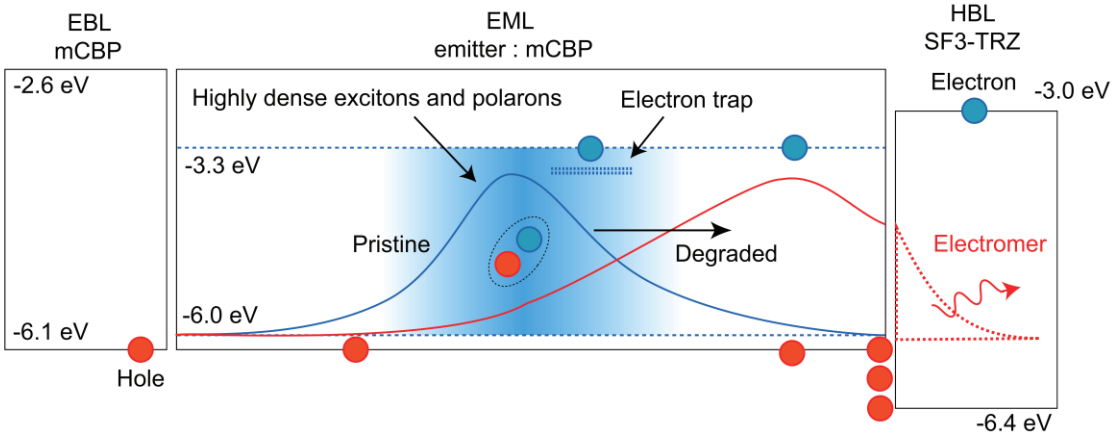

Figure 2-15. Schematic of the proposed OLED degradation process. Blue and red lines represent the relative exciton distributions of the pristine and degraded conditions, respectively. The HOMO and LUMO levels of each material for the EBL, the EML and the HBL are also shown.

2-4. Summary

In conclusion, I identified the change in the carrier balance as the main degradation process in 5CzBN-based OLEDs. The EL spectral change in the TADF emitters that occurred during degradation testing and the occurrence of electromer emission from the HBL, *i.e.*, the SF3-TRZ layer, indicated that degradation of the electron transport ability of the EML, resulting in inferior device performance. It was also proposed that the shortening of the triplet exciton lifetimes of the TADF emitters enhances device stability because of the suppression of unwanted triplet exciton-polaron interaction. Thus, I clarified that TPI is one of main channels for the device degradation. Furthermore, I note that the behavior of the SF3-TRZ layer in showing electromer emission provides a good indicator to aid in understanding of the shift in the carrier recombination site during degradation.

References

1. C. W. Tang & S. A. Vanslyke, Organic electroluminescent diodes. *Appl. Phys. Lett.* **51**, 913–915 (1987).
2. H. Uoyama, K. Goushi, K. Shizu, H. Nomura & C. Adachi, Highly efficient organic light-emitting diodes from delayed fluorescence. *Nature*. **492**, 234–238 (2012).
3. S. Hirata, Y. Sakai, K. Masui, H. Tanaka, S. Y. Lee, H. Nomura, N. Nakamura, M. Yasumatsu, H. Nakanotani, Q. Zhang, K. Shizu, H. Miyazaki & C. Adachi, Highly efficient blue electroluminescence based on thermally activated delayed fluorescence. *Nat. Mater.* **14**, 330–336 (2015).
4. H. Nakanotani, K. Masui, J. Nishide, T. Shibata & C. Adachi, Promising operational stability of high-efficiency organic light-emitting diodes based on thermally activated delayed fluorescence. *Sci. Rep.* **3**, 2127 (2013).
5. T. Kamata, H. Sasabe, M. Igarashi & J. Kido, A Novel Sterically Bulky Hole Transporter to Remarkably Improve the Lifetime of Thermally Activated Delayed Fluorescent OLEDs at High Brightness. *Chem. Eur. J.* **24**, 4590–4596 (2018).
6. A. S. D. Sandanayaka, T. Matsushima & C. Adachi, Degradation Mechanisms of Organic Light-Emitting Diodes Based on Thermally Activated Delayed Fluorescence Molecules. *J. Phys. Chem. C*. **119**, 23845–23851 (2015).
7. D. Y. Kondakov, Role of chemical reactions of arylamine hole transport materials in operational degradation of organic light-emitting diodes. *J. Appl. Phys.* **104**, 084520 (2008).
8. Y. Noguchi, H. J. Kim, R. Ishino, K. Goushi, C. Adachi, Y. Nakayama & H. Ishii, Charge carrier dynamics and degradation phenomena in organic light-emitting

diodes doped by a thermally activated delayed fluorescence emitter. *Org. Electron.* **17**, 184–191 (2015).

9. Y. Zhang, J. Lee & S. R. Forrest, Tenfold increase in the lifetime of blue phosphorescent organic light-emitting diodes. *Nat. Commun.* **5**, 5008 (2014).
10. D. P. K. Tsang & C. Adachi, Operational stability enhancement in organic light-emitting diodes with ultrathin Liq interlayers. *Sci. Rep.* **6**, 22463 (2016).
11. Y. Im, M. Kim, Y. J. Cho, J. A. Seo, K. S. Yook & J. Y. Lee, Molecular Design Strategy of Organic Thermally Activated Delayed Fluorescence Emitters. *Chem. Mater.* **29**, 1946–1963 (2017).
12. Z. Liu, F. Cao, T. Tsuboi, Y. Yue, C. Deng, X. Ni, W. Sun & Q. Zhang, A high fluorescence rate is key for stable blue organic light-emitting diodes. *J. Mater. Chem. C.* **6**, 7728–7733 (2018).
13. D. Zhang, M. Cai, Y. Zhang, Z. Bin, D. Zhang & L. Duan, Simultaneous Enhancement of Efficiency and Stability of Phosphorescent OLEDs Based on Efficient Förster Energy Transfer from Interface Exciplex. *Appl. Mater. Interfaces.* **8**, 3825–3832 (2016).
14. L. S. Cui, Y. L. Deng, D. P. K. Tsang, Z. Q. Jiang, Q. Zhang, L. S. Liao & C. Adachi, Controlling Synergistic Oxidation Processes for Efficient and Stable Blue Thermally Activated Delayed Fluorescence Devices. *Adv. Mater.* **28**, 7620–7625 (2016).
15. J. Lee, K. Shizu, H. Tanaka, H. Nakanotani, T. Yasuda, H. Kaji & C. Adachi, Controlled emission colors and singlet-triplet energy gaps of dihydrophenazine-based thermally activated delayed fluorescence emitters. *J. Mater. Chem. C.* **3**, 2175–2181 (2015).

16. P. Rajamalli, N. Senthilkumar, P. Gandeepan, P.-Y. Huang, M.-J. Huang, C.-Z. Ren-Wu, C.-Y. Yang, M.-J. Chiu, L.-K. Chu, H.-W. Lin & C.-H. Cheng, A New Molecular Design Based on Thermally Activated Delayed Fluorescence for Highly Efficient Organic Light Emitting Diodes. *J. Am. Chem. Soc.* **138**, 628–634 (2016).

17. H. Noda, H. Nakanotani & C. Adachi, Excited state engineering for efficient reverse intersystem crossing. *Sci. Adv.* **4**, eaao6910 (2018).

18. J. Endo, T. Matsumoto & J. Kido, Organic electroluminescent devices with a vacuum-deposited Lewis-acid-doped hole-injecting layer. *Jpn. J. Appl. Phys.* **41**, L358–L360 (2002).

19. G. Jin, J. Z. Liu, J. H. Zou, X. L. Huang, M. J. He, L. Peng, L. L. Chen, X. H. Zhu, J. Peng & Y. Cao, Appending triphenyltriazine to 1,10-phenanthroline: a robust electron-transport material for stable organic light-emitting diodes. *Sci. Bull.* **63**, 446–451 (2018).

20. L. S. Cui, S. Bin Ruan, F. Bencheikh, R. Nagata, L. Zhang, K. Inada, H. Nakanotani, L. S. Liao & C. Adachi, Long-lived efficient delayed fluorescence organic light-emitting diodes using n-type hosts. *Nat. Commun.* **8**, 2250 (2017).

21. T. Komino, H. Tanaka & C. Adachi, Selectively controlled orientational order in linear-shaped thermally activated delayed fluorescent dopants. *Chem. Mater.* **26**, 3665–3671 (2014).

22. B. Perucco, N. A. Reinke, D. Rezzonico, M. Moos & B. Ruhstaller, Analysis of the emission profile in organic light-emitting devices. *Opt. Express*. **18**, A246 (2010).

23. J. Kalinowski, G. Giro, M. Cocchi, V. Fattori & P. Di Marco, Unusual disparity in electroluminescence and photoluminescence spectra of vacuum-evaporated films

of 1,1-bis ((di-4-tolylamino) phenyl) cyclohexane. *Appl. Phys. Lett.* **76**, 2352–2354 (2000).

24. H. Yu, Y. Zhang, Y. J. Cho & H. Aziz, Exciton-Induced Degradation of Carbazole-Based Host Materials and Its Role in the Electroluminescence Spectral Changes in Phosphorescent Organic Light Emitting Devices with Electrical Aging. *ACS Appl. Mater. Interfaces*. **9**, 14145–14152 (2017).

25. J. Kalinowski, Bimolecular excited species in optical emission from organic electroluminescent devices. *J. Non. Cryst. Solids*. **354**, 4170–4175 (2008).

26. T. D. Schmidt, L. Jäger, Y. Noguchi, H. Ishii & W. Brütting, Analyzing degradation effects of organic light-emitting diodes via transient optical and electrical measurements. *J. Appl. Phys.* **117**, 215502 (2015).

27. N. C. Giebink, B. W. D'Andrade, M. S. Weaver, J. J. Brown & S. R. Forrest, Direct evidence for degradation of polaron excited states in organic light emitting diodes. *J. Appl. Phys.* **105**, 124514 (2009).

28. N. C. Giebink, B. W. D'Andrade, M. S. Weaver, P. B. MacKenzie, J. J. Brown, M. E. Thompson & S. R. Forrest, Intrinsic luminance loss in phosphorescent small-molecule organic light emitting devices due to bimolecular annihilation reactions. *J. Appl. Phys.* **103**, 044509 (2008).

29. S. Kwon, K. R. Wee, C. Pac & S. O. Kang, Significance of irreversible formation of "electromer" in 1-bis[4-[N,N-di(4-tolyl)amino]phenyl]-cyclohexane layer associated with the stability of deep blue phosphorescent organic light emitting diodes. *Org. Electron.* **13**, 645–651 (2012).

Chapter 3

Proving the origin of degradation in an organic light-emitting diode derived from triplet exciton interaction by a magnetic field

Masaki Tanaka, Ryo Nagata, Hajime Nakanotani and Chihaya Adachi

Communications Materials, submitted

Abstract

Magnetic field effects (MFEs) on the electroluminescence of OLEDs are used to characterize exciton dynamics such as generation, annihilation, and degradation. However, MFE interpretation has been puzzling and is far from being comprehensive. Here, I show that the MFEs in OLEDs can be understood in terms of the combined magnetic responses of device characteristics derived from polaron-pair and triplet exciton quenching processes such as triplet-polaron interactions and triplet-triplet annihilation. Device degradation has a clear relationship with the MFE amplitudes, enabling nondestructive measurements of OLED degradation. The results and proposed mechanism provide a better understanding of MFEs on OLEDs and device degradation phenomena.

3-1. Introduction

A significant improvement in OLED stability is of crucial importance, particularly in blue OLEDs, so that they can be used in high-performance displays and light sources. To improve OLED lifetimes, a detailed understanding of degradation processes is required. Several mechanisms have been proposed[1–9]. For example, Kondakov *et al*. reported that chemical decomposition of the organic materials is a critical degradation route[1–4] that originates from high-energy particles, such as highly excited triplet excitons and polarons, generated *via* triplet-triplet annihilation (TTA) or triplet-polaron interactions (TPI)[5–8]. In **Chapter 2**, the carrier transport properties of EMLs were investigated by means of EOD and HOD studies, and I clarified that TPI is one of dominant channels for the degradation of TADF-OLEDs. The carrier traps generated through the highly excited polarons during device operation significantly affect the carrier transport properties in the EML and the OLED performance[9]. It has been strongly suggested that the dynamics of triplet excitons is largely responsible for device degradation. However, no direct evidence has been presented, and a detailed analysis of exciton dynamics *via* nondestructive measurements is complex.

To probe the dynamics of excited triplet states, external magnetic fields are used to lift the degeneracy. Magnetic field effects (MFEs) on the EL properties of OLEDs were first reported in 2003 by Kalinowski *et al*.[10], in which the field modulated the ratio of the singlet/triplet exciton yield. This was the result of modulating the ratio of singlet and triplet polaron pairs (^{1}PP and ^{3}PP). Numerous studies regarding the mechanism of MFEs on OLEDs were then based on fluorescence[11,12], phosphorescence[13], exciplex[14], and TADF emitters[15,16] to unveil the underlying dynamics of exciton generation, radiation, and annihilation processes. The PP[11,17], TPI[16,18], and TTA mechanisms[12,16] were proposed

to explain MFEs. However, the interpretation of MFEs based on EL has been unclear, and the relationship between exciton dynamics and OLED degradation has been lacking. **Figure 3-1** shows the schematics of magnetic responses of the OLEDs in this study.

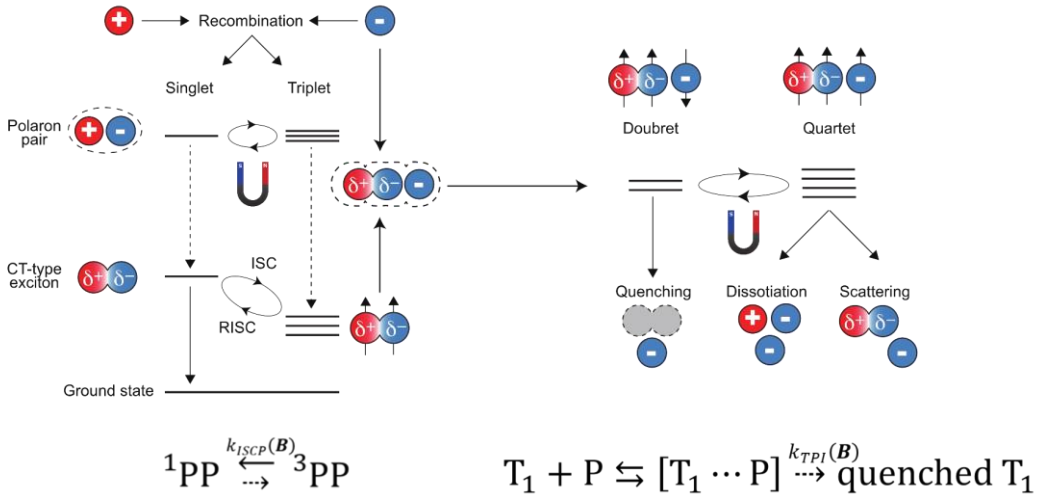

Figure 3-1. Schematic of TPI in OLEDs under electrical excitation. A magnetic field suppresses the ISC of the PP state (small ISC rate, k_{ISCP}) and TPI reactions (small TPI rate, k_{TPI}). $[\mathbf{T_1} \cdots \mathbf{P}]$ represents a trion intermediate state.

Here, I demonstrate that magnetic-field-modulated EL (MEL) can be used to track triplet excitons dynamics in OLEDs during the degradation. MEL signals from TADF-OLEDs were divided into low-field effects (LFEs) and high-field effects (HFEs) that corresponded to PP and TPI mechanisms, respectively. I also found that HFE shows a clear dependence on triplet exciton lifetimes. Based on the assignment of the origin of the MEL signals, I analysed those signals of degraded OLEDs that exhibited large amplitudes relative to those of pristine (undegraded) OLEDs. Then, I confirmed that the shapes of the MEL profiles changed due to an exciplex formation according to the unwanted change in location of the carrier recombination zone. I thus nondestructively revealed the exciplex formation at the interface between an emission layer (EML) and a hole-blocking layer (HBL) that resulted in low IQE.

3-2. Experimental

3-2-1. Sample fabrication

Various TADF molecules were used as emitters in OLEDs, and all were synthesized here (**Figure 3-2**). The 4CzIPN, PXZ-TRZ, and ACRXTN molecules have relative short exciton lifetimes relative to those of 2CzPN, PIC-TRZ, and 3CzTRZ. 4CzIPN, PXZ-TRZ, ACRXTN, 2CzPN, PIC-TRZ and 3CzTRZ are 1,2,3,5-tetrakis(carbazol-9-yl)-4,6-dicyanobenzene, 10-[4-(4,6-diphenyl-1,3,5-triazin-2-yl)phenyl]-10H-phenoxazine, 3-(9,9-dimethylacridin-10(9H)-yl)-9H-xanthen-9-one, 1,2-bis(carbazol-9-yl)-4,5-dicyanobenzene, 2-biphenyl-4,6-bis(12-phenylin-dolo[2,3-a]carbazol-11-yl)-1,3,5-triazine and 9-(3-(9H-carbazol-9-yl)-9-(4-(4,6-diphenyl-1,3,5-triazin-2-yl)phenyl)-9H-carbazol-6-yl)-9H-carbazole, respectively.

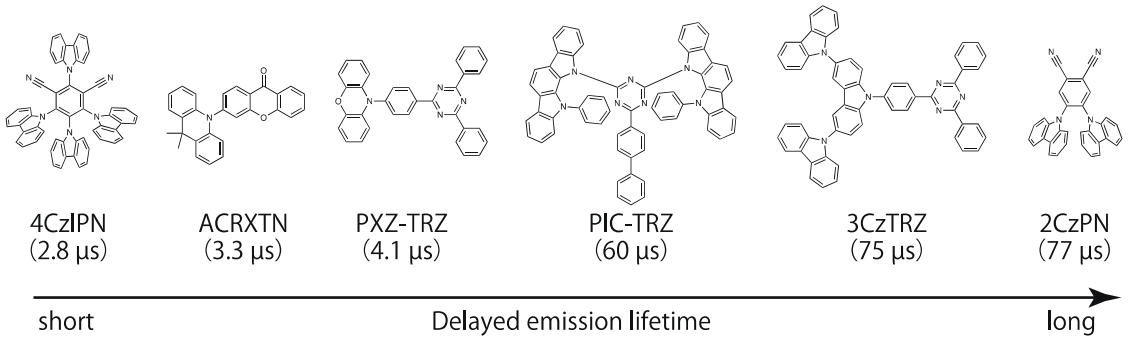

Figure 3-2. Molecular structures of TADF emitters, with delayed-emission lifetimes.

The OLEDs were fabricated *via* vacuum vapor deposition without exposure to ambient air. The device structure (**Figure 3-3**) is ITO (100 nm) / HAT-CN (10 nm) / Tris-PCz (30 nm) / mCBP or mCP (5 nm) / EML (30 nm) / SF3-TRZ (10 nm) / 30 wt.% Liq:SF3-TRZ (50 nm) / Liq (2 nm) / Al (100 nm). The EMLs were formed using a co-deposition technique. For 3CzTRZ, mCP was adopted as a host and electron-blocking layer (EBL) because of triplet exciton confinement. In other cases, mCBP was used as a

host and EBL. ITO, HAT-CN, Tris-PCz, mCBP, mCP, SF3-TRZ, and Liq are indium tin oxide, 1,4,5,8,9,11-hexaazatriohenyleane hexacarbonitrile, 9,9'-diphenyl-6-(9-phenyl-9H-carbazol-3-yl)-9H,9'H-3,3'-bicarbazole, 3,3'-di(9H-carbazol-9-yl)-1,1'-biphenyl, 1,3-bis(N-carbazolyl)benzene, 2-(9,9'-spirobi[fluoren]-3-yl)-4,6-diphenyl-1,3,5-triazine and 8-hydroxyquinolinolato-lithium, respectively. All organic layers, except for the Liq layer, were deposited at a rate of 0.1 nm/s, while the Liq layer was deposited at 0.03 nm/s. The deposition rate of Al was 0.1 nm/s. The device area was approximately 0.04 cm^2. After fabrication, the devices were immediately encapsulated under glass using epoxy glue in a nitrogen-filled glovebox (H_2O > 0.1 ppm, O_2 > 0.1 ppm).

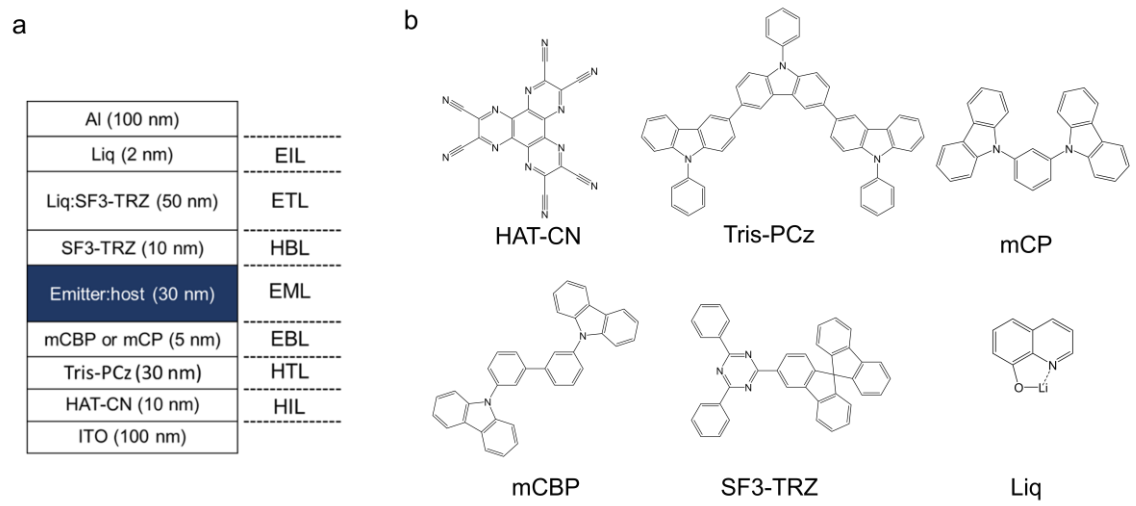

Figure 3-3. (a) Device structure of TADF-OLEDs in this study. (b) molecular structures for the devices.

3-2-2. Sample characterization

In MFE measurements, the magnetic field was applied along the direction of the substrate, and the magnitude (B) was varied over 0–0.57 T. EL spectra were collected with a fiber spectrometer (MAYA2000PRO, Ocean) and the driving voltage (V) or current density (J) at each magnitude of the magnetic field were measured with a source-measure unit (Keithley 2612B, Tektronix). Measurements were performed for two cycles of from 0 to 0.57 T and from 0.57 to 0 T and were averaged into one cycle. MEL_J, MR, MEL_V and MC were calculated from:

$$MEL_J = \frac{I_{EL}(B) - I_{EL}(0)}{I_{EL}(0)} \quad \text{(under constant current condition)}$$

$$\mathrm{MR} = \frac{V(B) - V(0)}{V(0)} \quad \text{(under constant current condition)}$$

$$MEL_V = \frac{I_{EL}(B) - I_{EL}(0)}{I_{EL}(0)} \quad \text{(under constant voltage condition)}$$

$$\mathrm{MC} = \frac{J(B) - J(0)}{J(0)} \quad \text{(under constant voltage condition)}$$

where MEL_J, MR, MEL_V, MC, $I_{EL}(B)$, $V(B)$, and $J(B)$ were the magneto-electroluminescence under constant J, the magneto-resistance, the magneto-electroluminescence under V, magneto-conductance, the intensity of electroluminescence, the voltage, and the current density under magnetic field B, respectively. The fitting analysis of the MFE profiles to separate LFE and HFE was performed with Lorentzian and non-Lorentzian functions with four parameters for amplitudes and characteristic magnetic fields. All the parameters were constrained as positive values in the fits. Initial values of A_L, A_H, B_L, and B_H were 0.05, 0.1, 3 mT, and 10 mT, respectively.

3-3. Results and discussion

3-3-1. Assessment of MFE profiles in various TADF-OLEDs

3-3-1-1. MEL profiles and fitting analysis

I focused on TADF emitter-based OLEDs (**Figure 3-2**). First, the MEL profiles of undegraded OLEDs were analyzed to probe the origin. **Figure 3-4** shows typical MEL_J profiles of a 4CzIPN based OLED. To assess the origin of the MEL profiles of the OLEDs, I performed an analysis of the MEL profiles by the fitting analysis based on the well-established Lorentzian and non-Lorentzian equations[16–19]:

$$\mathrm{MFE} = \mathrm{LFE} + \mathrm{HFE} = \frac{A_L B^2}{B^2 + B_L^2} + \frac{A_H B^2}{(B + B_H)^2}$$

where A_L, B_L, A_H, and B_H were parameters for the amplitudes (A_L and A_H) and characteristic magnetic fields (B_L and B_H) for LFE and HFE, respectively. The results are summarized in **Figure 3-4a** and **Table 1**. The MEL profiles were separated into two parts, indicating that there are two different mechanisms to explain the MEL profiles.

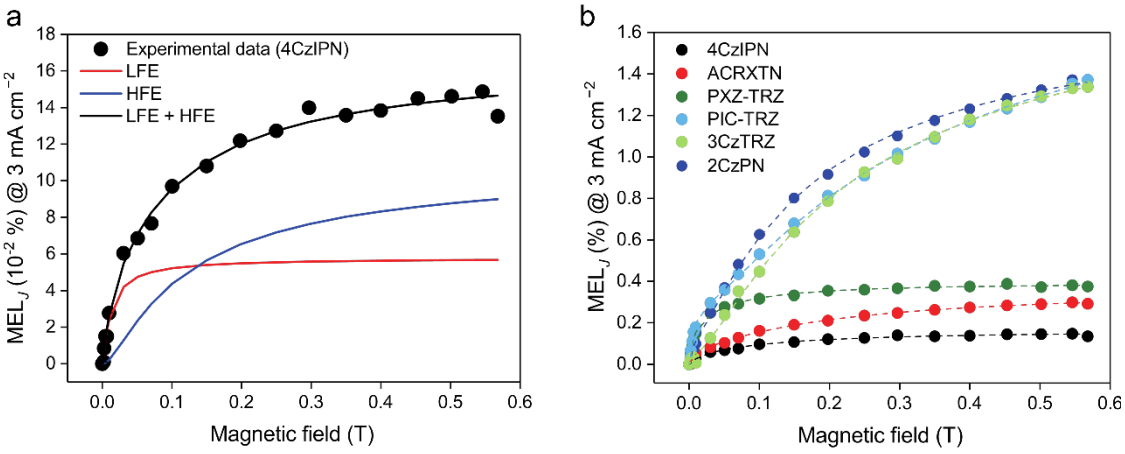

Figure 3-4. (a) Fit of MEL_J profile of 4CzIPN-based OLED under constant 3.0-mA cm^{-2} current into LFE and HFE. (b) MEL_J profiles of various TADF-OLEDs. The dashed lines are fits.

Table 3-1. Fitting parameters of MEL$_J$ of TADF-OLEDs by LFE and HFE. $|D|$ and $|E|$ are the absolute values of ZFS parameters. (Refs.:20,21)

	A_L (-)	B_L (mT)	A_H (-)	B_H (mT)	$\|D\|$ (mT)	$\|E\|$ (mT)
4CzIPN	0.058	5.3	0.11	58.5	40, 46	11
PXZ-TRZ	0.239	6.6	0.18	58.5	49	5.4
ACRXTN	0.091	4.1	0.29	101.0	No data	
2CzPN	0.117	4.8	1.62	81.0	68	15
PIC-TRZ	0.264	5.7	1.83	192.7	98	9.6
3CzTRZ	0.038	4.3	1.87	112.5	No data	

Because B_L is a comparable value for the PP mechanism[16–19], LFE originate from 'bright' singlet excitons to an increase in ^{1}PP generation by the magnetic field. In contrast, a large value (~100 mT) was found for B_H. I compared the B_H with the zero-field splitting (ZFS) values, *i.e.*, D and E, of the excited triplet state of TADF emitters reported previously[20,21], and the good agreement suggested that the HFE results from the reaction of triplet excitons.

The delayed fluorescence lifetimes of TADF emitters affect the MEL profile, as shown in **Figure 3-4b**. Although the signs of all the MEL$_J$ profiles were positive, the shape and magnitude of the profiles, especially in the HFE region, depended on the delayed fluorescence lifetimes of the emitters. This behavior can be naturally understood from the probability of triplet exciton reaction such as TTA and TPI that should strongly depend on triplet exciton lifetimes[22–24]. In fact, the devices based on TADF emitters exhibiting long-delayed fluorescence showed steep EL efficiency rolloff as shown in **Figure 3-5**.

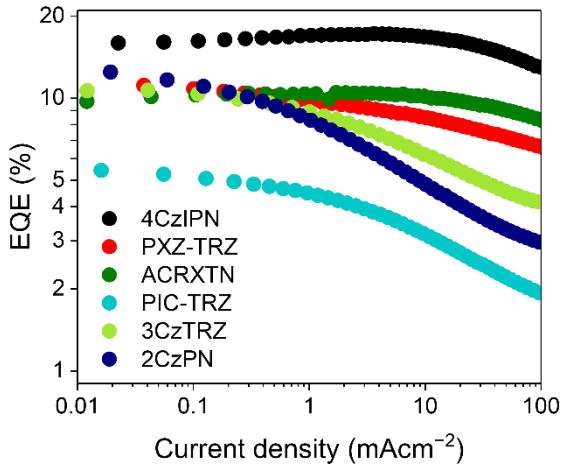

Figure 3-5. (a) *J*-EQE characteristics of TADF-OLEDs.

3-3-1-2. Possibility of TTA as HFE

Magneto-photoluminescence (MPL) measurements were performed and confirmed that the MPL of 20 wt.% 4CzIPN:mCBP and 2CzPN:mCBP films did not exhibit PL modulation in high magnetic fields (**Figure 3-6**). Thus, the contribution of a TTA event to the MEL$_J$ can be negligible.

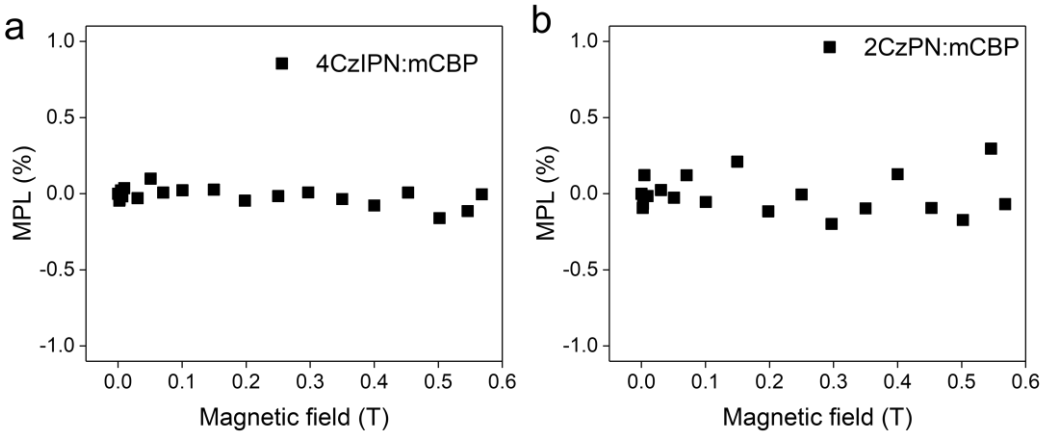

Figure 3-6. MPL profiles of 20 wt.% (a) 4CzIPN:mCBP and (b) 2CzPN:mCBP films with 405-nm excitation.

3-3-1-3. Possibility of TPI as HFE

Considering the effect of TPI on MEL$_J$, **Figure 3-1** is a schematic of a TPI process in OLEDs under electrical excitation. The triplet-polaron intermediate state (trion) is formed when the two particles, *i.e.*, a triplet exciton (T_1) and a polaron (P), and has two possible spin states: 'doublet' and 'quartet'[18,19,25]. Because the reaction of doublet-trion, *i.e.*, triplet exciton-polaron annihilation (TPA), is spin-allowed, the triplet exciton can be immediately quenched *via* energy transfer to the polaron, generating a ground-state molecule and an excited (hot) polaron. Because the energy of the hot polaron is enough high to dissociate chemical bonds, the TPA generates the decomposed materials acting as an exciton quencher and/or a carrier trap.

In contrast, the reaction of a quartet state is spin-forbidden and the lifetime of a quartet-trion is longer than that of the doublet. Thus, there are two possible ways of the quartet-trion reaction: "carrier scattering" and "exciton dissociation." In carrier scattering, a quartet -trion separates into a triplet exciton and a polaron, where the net charge carrier mobility is decreased. In contrast, the dissociation process increases the net carrier density because the triplet exciton dissociates into a hole and an electron *via* the quartet-trion intermediate state.

A magnetic field can suppress the interaction probability between a triplet exciton and a polaron, reducing the rates of annihilation, scattering, and dissociation[17,18,23,25–27]. Hence, the emission and carrier transport properties should have a strong dependence on an applied magnetic field. In this research, although TPA and exciton dissociation processes were observed *via* TPI reactions in MFEs in TADF-OLEDs, carrier scattering process was not observed. I infer that carrier scattering is a minor effect in the TADF-OLEDs because of the limited change in carrier transport due to the rather aligned HOMO

and LUMO levels of the doped emitters relative to those of the host molecules (**Figure 3-7**).

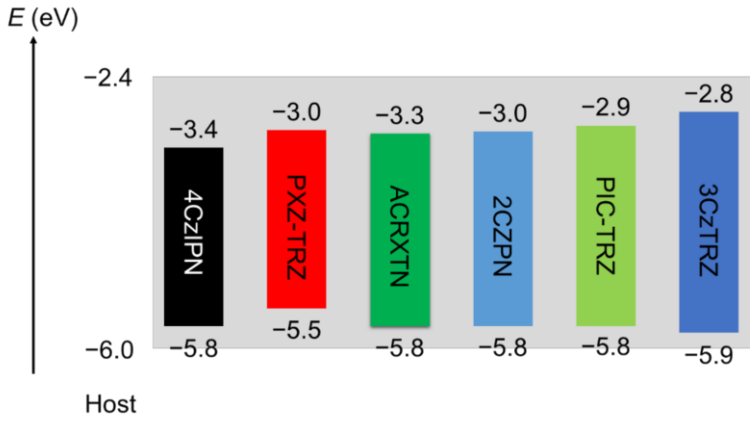

Figure 3-7. Energy level diagrams of HOMO and LUMO levels of EMLs for various TADF emitters[28–32].

3-3-2. Comparison of MFEs under constant current and voltage conditions

To understand the origin of MFEs in OLEDs comprehensively, the MFE profiles such as MEL_J, magneto-resistance (MR), MEL under a constant voltage (MEL_V), and the magneto-conductance (MC) in 4CzIPN- and 2CzPN-based OLEDs are shown in **Figure 3-8**. Logarithmic MFE profiles are depicted to separate the dominant LFE and HFE components below and above 0.1 T, respectively. In contrast to the positive sign of MEL_J and MR (**Figures 3-8a** and **c**), MEL_V and MC include negative components (**Figures 3-8b** and **d**). The magneto-efficiency under constant voltage ($M\eta_V$) were calculated by[16]:

$$M\eta_V = \ MEL_V - MC$$

MEL_Js have positive signs of LFE and HFE whereas MEL_Vs have different shapes, i.e., both negative sighs for LFE and HFE of 4CzIPN-OLED and negative and positive signs for LFE and HFE of 2CzPN-OLED. On the other hand, $M\eta_V$s have both positive sign of LFE and HFE. This indicates that the negative sign of the LFE of MEL_V did not result from lowering of the emission efficiency but instead from decreased current density. Furthermore, the MR signals in **Figures 3-8a** and **c** can be attributed to TPI-induced triplet dissociation because of the increased net charge carrier density in the EMLs. In a magnetic field, the charge carrier density *via* exciton dissociation should decrease and the resistance should increase. Although the MR profiles had positive LFE and HFE, the MC profiles had negative LFE and HFE because of the inverse relationship between resistance and conductance.

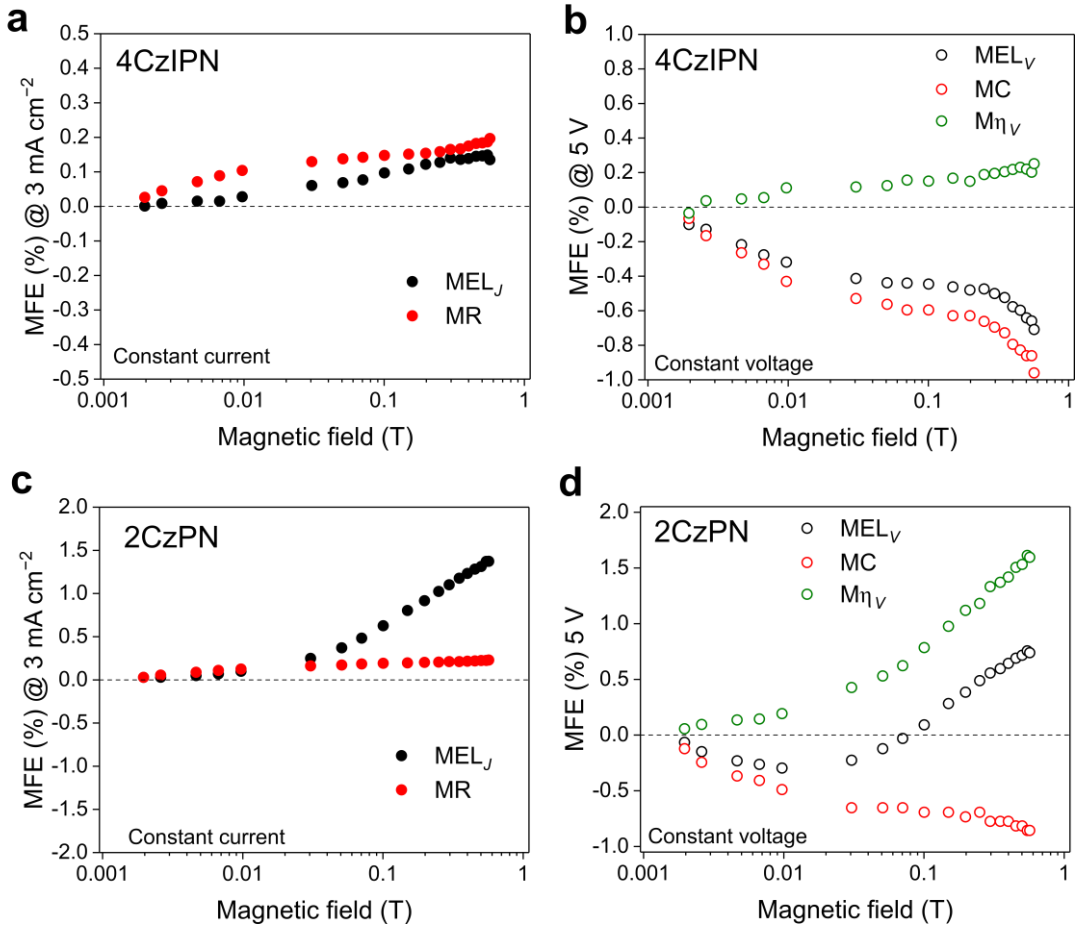

Figure 3-8. (a and c) MEL$_J$ and MR of 4CzIPN-based and 2CzPN-based OLEDs under a constant current density of 3.0 mA cm^{-2}. (b and d) MEL$_V$, MR and Mη_V of 4CzIPN-based and 2CzPN-based OLEDs under the constant applied voltage of 5 V.

MEL$_J$ signals in **Figures 3-8a** and **c** had positive HFE, indicating increased EL from the magnetic field, while the positive LFE of MEL$_J$ can be understood as an increase in singlet excitons by the PP mechanism explained above. The high magnetic field suppressed triplet quenching through TPA and triplet dissociation processes, and increased the triplet exciton density. It also successively enhanced the upconversion of triplet excitons to singlet states *via* RISC, resulting in the positive HFE of MEL. In the case of MEL$_V$ signals in **Figures 3-8b** and **d**, a decrease in current density by the magnetic field results in decreased luminance and a negative LFE.

The negative HFE of MEL_V in the 4CzIPN-based device (**Figure 3-8b**) suggested that there was a larger contribution due to the decreased current density (negative MC), relative to the effect of TPA suppression and dissociation processes to increase the EL intensity. This was because of the small extent of triplet exciton quenching in the 4CzIPN-based device. Therefore, the LFE and HFE result from the PP and TPI mechanisms that are mainly TPA and triplet dissociation, respectively. These results indicate that the observation of MFEs of TADF-OLEDs can clearly prove the presence of TPI under device operation, that is one of the dominant degradation channels as suggested in **Chapter 2**.

3-3-3. Exciton dynamics in degraded TADF-OLEDs

3-3-3-1. Variation of MEL of degraded devices

MFEs were shown to help understand triplet exciton dynamics in OLEDs. They can also be applied to track OLED degradation. **Figures 3-9a** and **b-d** plot the decreased luminance and MEL$_J$ profiles of 4CzIPN-, 2CzPN-, and ACRXTN-based OLEDs under a constant current density of 3.0 mA cm^{-2}, respectively. L/L_0 is the relative luminance normalized by the initial luminance L_0, which was 1,686 cd m^{-2} for 4CzIPN, 492 cd m^{-2} for 2CzPN, and 812 cd m^{-2} for ACRXTN. During the degradation, the MEL$_J$s monotonically increased with the drop in luminance, which strongly indicated changes in triplet exciton dynamics during device aging. The discussion below omits the effect of a TTA process on the degradation because it was not the primary channel for triplet quenching under low current density (3.0 mA cm^{-2}), as discussed in **Appendix A**.

The MEL$_J$ signals in the degraded OLEDs were well separated into LFEs and HFEs, and the magnitudes of both (A_L and A_H) were plotted with L/L_0 and operation time in **Figures 3-10a** and **b**, respectively. The A_Ls and A_Hs exhibited a linear increase with decreased luminance in all devices. The characteristic magnetic fields B_Ls and B_Hs of LFE and HFE were also plotted with L/L_0 and the operation time in **Figures 3-10c** and **d**, respectively. The B_Hs of degraded devices were smaller than those of pristine devices that exhibited good agreement with the ZFS values of their excited triple states. The decreases in B_Hs thus suggest additional components that affect the MFE.

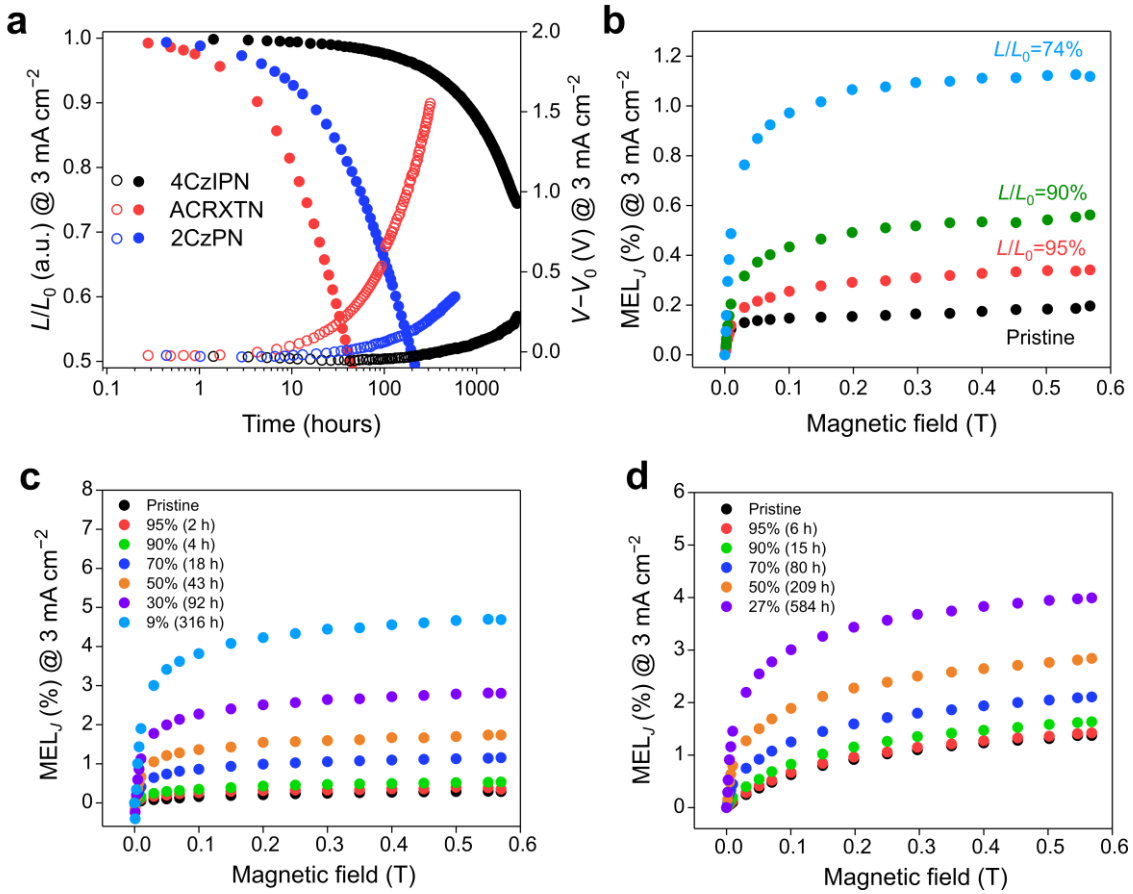

Figure 3-9. (a) Luminance decays and operating voltage characteristics of 4CzIPN-, ACRXTN-, and 2CzPN-based OLEDs with a constant current density of 3.0 mA cm^{-2}. (b), (c) and (d) MEL_J profiles of pristine and degraded 4CzIPN-, ACRXTN- and 2CzPN-based OLEDs, respectively.

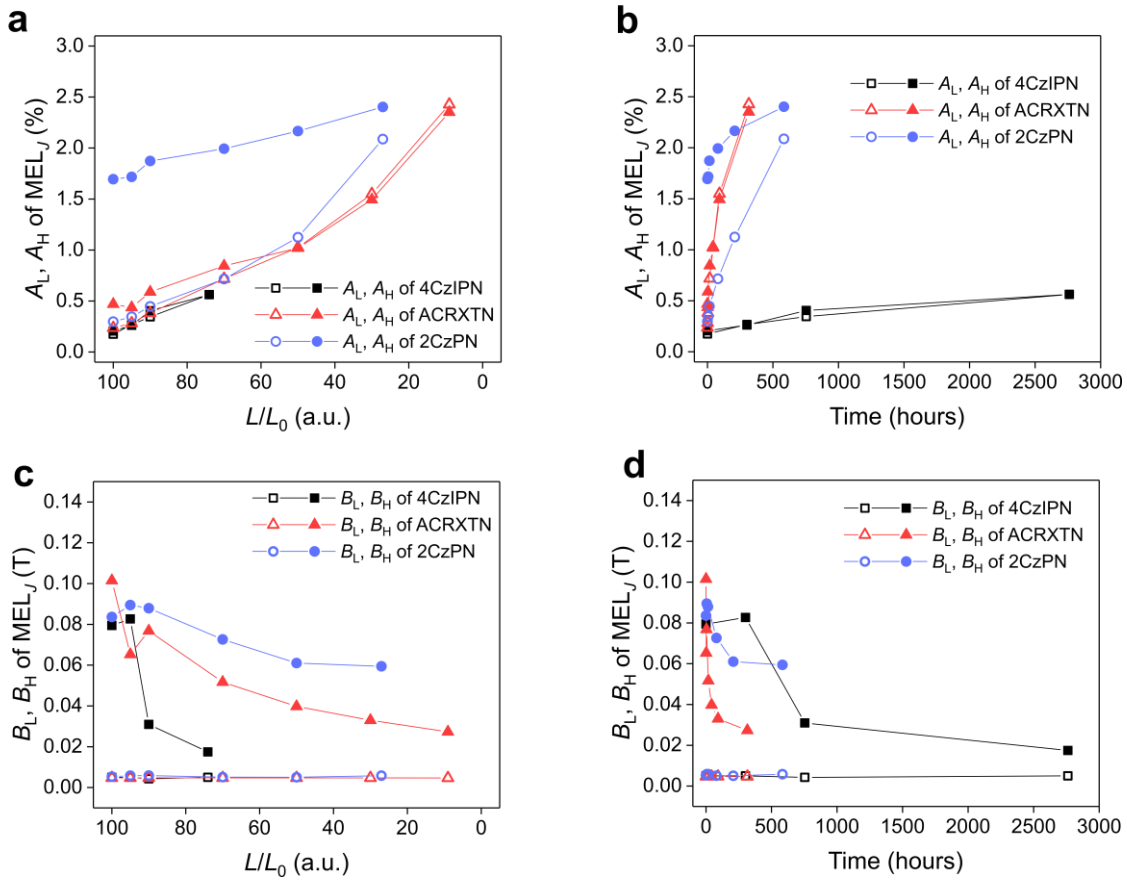

Figure 3-10. Relationship between L/L_0 and (a) A_L and A_H, (c) B_L and B_H. Relationship between operating time and (b) A_L and A_H, (d) B_L and B_H.

3-3-3-2. Exciplex formation detected by MFE

One component could be exciplex formation at the interface between the EML and HBL because of the change in the carrier transport in the EML during device degradation that induces a large accumulation of holes and electrons at the interface. This was confirmed by moving the recombination site toward the HBL side and observing electromer emission from SF3-TRZ (**Figure 3-11**)[9].

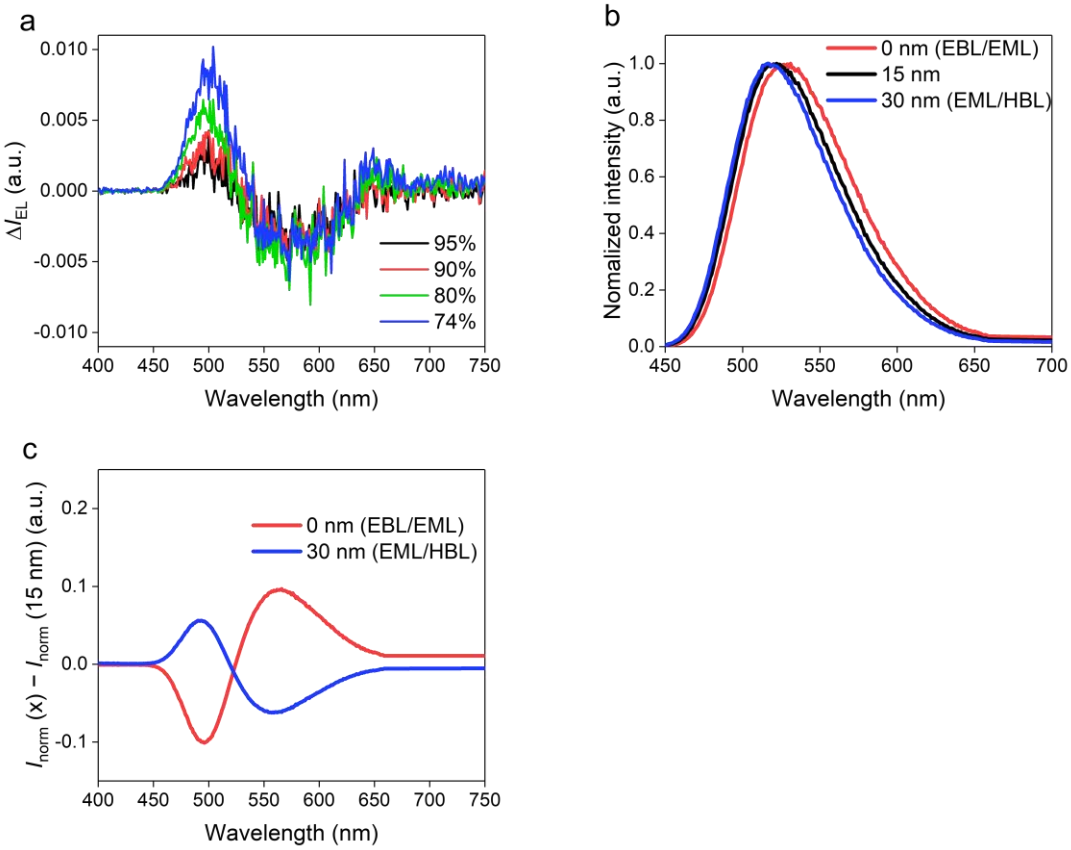

Figure 3-11. (a) Difference spectra of a degraded 4CzIPN-based OLED. Difference spectrum were defined in **Chapter 2**. After degradation, spectral blueshift and weak red emission were observed. (b) Results of optical simulations of normalized spectra of a 4CzIPN-OLED with various emitter locations in the EML (emitter distribution: delta distribution). (c) Calculated difference spectra from the simulation results of **Figure 3-11b**. x means the position of dipole from an interface between EBL and EML.

In addition, the EL redshifted relative to the PL with increased shoulder emission between 450 and 500 nm in the undoped device, with the EML containing only mCBP (**Figure 3-12a**). The emission can be assigned to the exciplex ($mCBP^{\delta+}$:SF3-$TRZ^{\delta-}$). **Figure 3-12b** shows MEL_J at various emission wavelengths of the undoped device. Because this emission may have included some other components of emissive species such as the emission from a monomer, excimer[33,34], electromer[9,35,36], or an electroplex[13,37], the MEL_J signals in **Figure 3-12b** exhibited unusual profiles. The long-wavelength emission had large MELs (**Figure 3-12c**), even though the exciplex generally has large MELs at short wavelengths[14]. Although the detailed mechanism and the origin of these results remain unclear, they strongly suggest that MEL_Js of the degraded devices contain TADF emission *via* energy transfer (Förster resonance energy transfer (FRET) and Dexter energy transfer) from the exciplex ($mCBP^{\delta+}$:SF3-$TRZ^{\delta-}$), as shown in **Figure 3-12d**. Thus, I speculate that there were three components of the MFE in the degraded devices originating from PP, TPI, and exciplex formation.

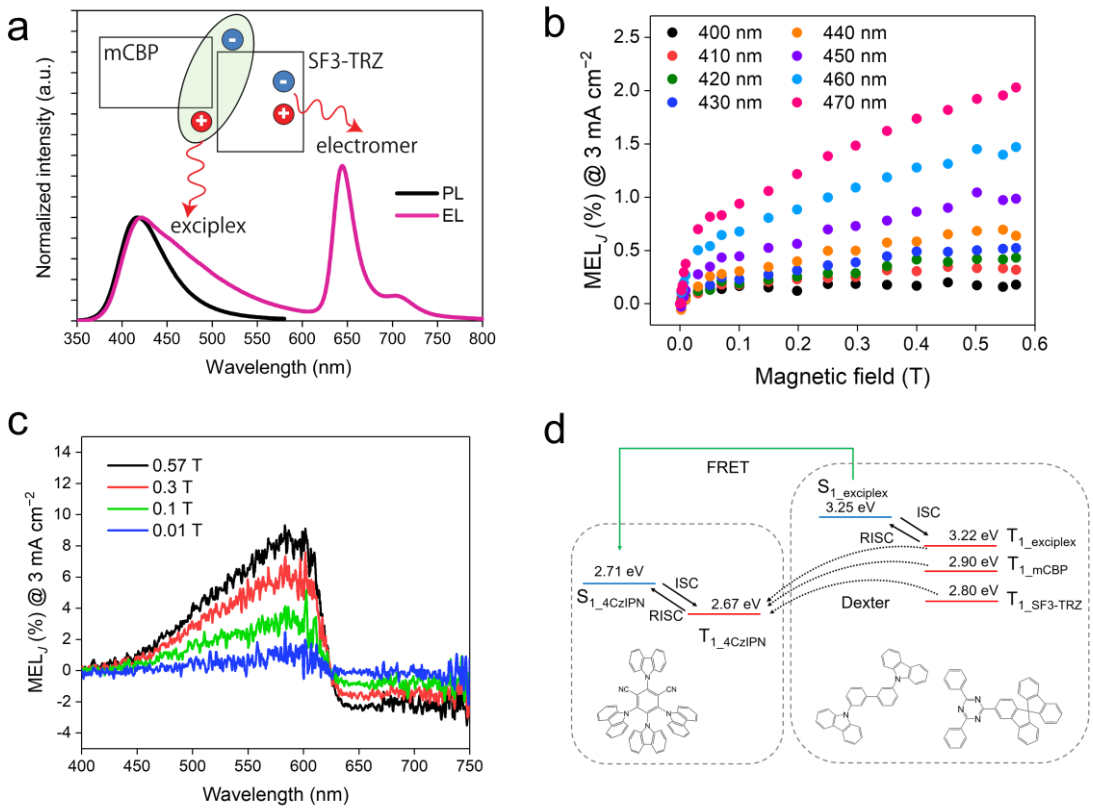

Figure 3-12. (a) PL spectrum of the co-deposited film of 50 wt.%-mCBP:SF3-TRZ, and EL spectrum of the undoped EML device (only mCBP). (b) MEL$_J$ profiles of undoped EML device with various emission wavelengths. (c) Wavelength dependence of MEL$_J$ of the undoped EML device. (d) Schematic of energy transfer to TADF emitters in degraded devices.

3-3-3-3. Contribution of exciton quenching to luminance drop

Electrically-generated triplet excitons in the degraded devices significantly suffered from deactivation processes and were quenched because of their long lifetimes. The linear relationships between L/L_0 and A_L (**Figure 3-10a**) indicated that fractions of deactivated triplet excitons increased with degradation in all devices. These increases were not due to the generation of 'static' triplet quenchers, such as decomposed materials, because there was no change in delayed emission lifetime between the pristine and degraded devices (**Figure 3-13**) in both transient PL and EL decays[38]. I thus estimated the origin for the A_L increases from the aspect of TPI probability and the change in carrier recombination sites, such as adjacent layers and/or film interfaces. In degraded devices, the PP mechanism converted ^{3}PP into ^{1}PP, and the magnetic field decreased the population of deactivated triplet excitons by TPI, resulting in the large LFE amplitude.

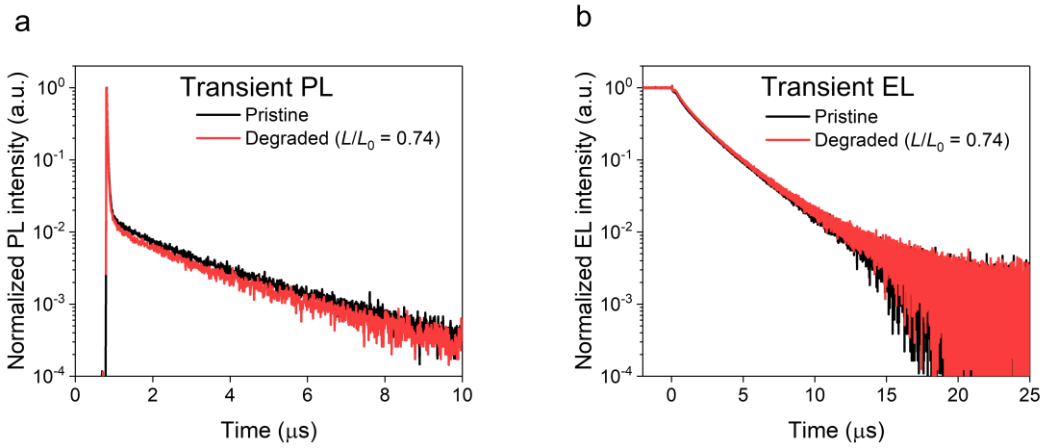

Figure 3-13. Transient emission profiles of pristine and degraded 4CzIPN-based devices. (a) PL and (b) EL. 4CzIPN PL excitation wavelength was 405 nm. The driving voltage corresponded to the current density of 3 mA cm^{-2}. A negative bias of −10 V turned off the devices to reduce the effect of carrier traps.

3-3-3-4. Carrier trap generation in degraded OLEDs

I conducted displacement current measurements (DCM)[4] to obtain information on carrier transport and injection in the degraded devices. DCM profiles of pristine devices depicted in **Figure 3-14** exhibited increases in capacitance and plateau structure at injection voltage (V_{inj}), indicating carrier injection and accumulation. The V_{inj}s depended on doped emitter molecules in the EML. The current onset was lower than the 2.6-V threshold voltage (V_{th}) of actual injection current because the carrier injection and accumulation were originating from a surface charge of the EMLs induced by spontaneous orientation polarization (SOP) of polar emitter molecules, as reported by Noguchi *et al*[4]. The SOP of the doped TADF molecules forms a surface charge δ^- at the interface between the EBL and EML, and δ^+ at the interface between the EML and HBL. The layer thickness dependence of the 2CzPN-based OLED in the DCM profiles (**Figure 3-14d**) confirmed that electrons were injected and accumulated in the devices at the V_{inj}.

In the degraded devices, V_{inj} shifted positive and the accumulation charge densities were reduced because they were proportional to the difference between V_{inj} and V_{th}. This indicated the formation of the charge carrier traps, especially electron traps in the EML, and simultaneously suppressed carrier injection (see ref. 4). Hence, the generation of carrier traps in degraded devices changed the charge transport properties and increased exciton quenching by TPI. As reported previously, undesired triplet reactions such as TPI are origins of carrier traps in TADF-OLEDs[9,39,40].

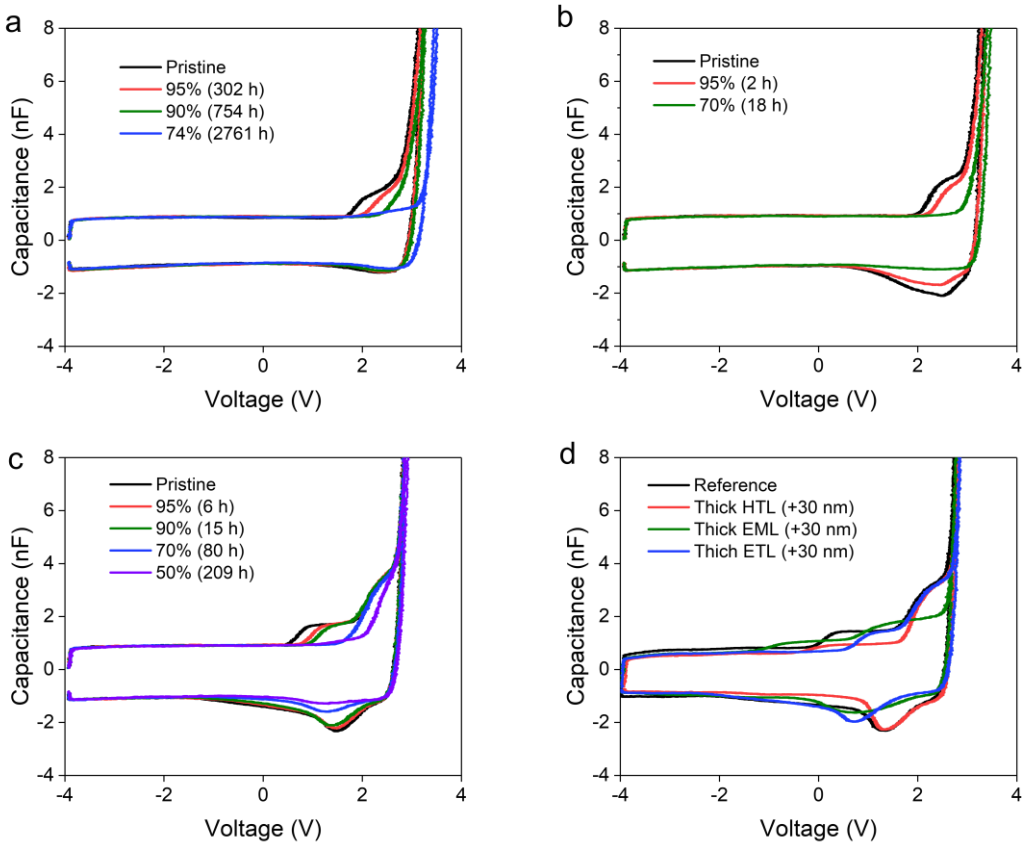

Figure 3-14. DCM profiles of pristine and degraded OLEDs based on (a) 4CzIPN, (b) ACRXTN, and (c) 2CzPN. (d) DCM profiles of thicker 2CzPN-based OLED (red: thick HTL, green: thick EML, blue: thick ETL) than the reference device.

3-3-3-5. Detailed interpretation of MFE variations during degradation

Regarding the HFE amplitudes, those of degraded devices include the effects of TPI and exciplex formation. The increase in HFE amplitudes (**Figures 3-10a** and **b**) also suggested, as explained above, an increase in the fraction of deactivated triplet excitons *via* TPI and exciplex formation at the EML/HBL interface. I understand device degradation by observing MFEs, which include PP and TPI mechanisms, and exciplex formation.

Furthermore, the linear relationships between L/L_0s and the amplitudes of MELs (**Figure 3-10a**) for pristine and degraded devices originate from both the change in EL intensity under the magnetic field $\Delta I_{EL}(B)$ and the EL intensity with no magnetic field $I_{EL}(0)$. The relative $\Delta I_{EL}(B)$s increase during the initial device degradation and decrease during the latter part (see **Appendix B**). An increase in TPI and exciplex formation increases the magnitudes of MELs. However, the recovery of EL intensity $\Delta I_{EL}(B)$s decreases in extremely inefficient devices because the conversion of triplet PP to singlet PP, and the suppression of TPI, cannot contribute to the emission from the TADF emitters in degraded devices, such as an extremely biased condition.

3-3-3-6. Operational lifetime improvement under magnetic field

Device operation under external magnetic fields should lengthen the operational lifetime because the field reduces the triplet density and suppresses undesired TPI. **Figure 3-15** shows the luminance decay curves with and without a 0.2-T magnetic field under 30 mA cm^{-2} current density. The field slightly but clearly improved the device stability. Specifically, the averaged LT_{95} was 3.3 hours without and 4.0 hours with the magnetic field, respectively. Here, I assume that:

$$\mathrm{LT} \times L_0^n = const.$$

where n is an acceleration factor[41]. In **Table 2**, I obtain n of 2.0, and LT_{95} is predicted to be 369 hours under a 3.0 mA cm^{-2} current density and a 0.2-T magnetic field. This is a 20% improvement in device stability and strongly indicates that either or both the decrease in triplet excitons as a LFE and the suppression of TPI as a HFE can enhance device stability because of suppressed triplet excitons reactions.

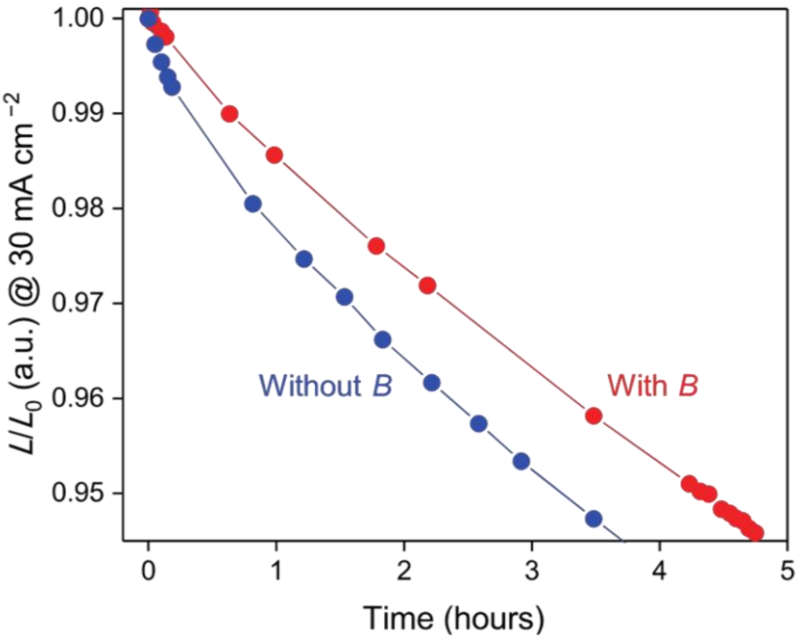

Figure 3-15. Luminance decay curves of 4CzIPN-based OLEDs under constant high current of 30 mA cm^{-2}. The pixels were fabricated on same substrate at the same time.

Table 3-2. Device lifetime measurements with and without an external magnetic field. LT_{95}s are averaged.

Current density	L w/o B (cd m^{-2})	MEL_J (%)	L w/ 0.2 T (cd m^{-2})	LT_{95} w/o B (hours)	LT_{95} w/ 0.2 T (hours)
3 mA cm^{-2}	1680	0.12	1682	302	369 (estimated)
30 mA cm^{-2}	15977	0.42	16044	3.41	4.03

3-4. Summary

I investigated the MFEs on the EL of TADF-OLEDs to understand the underlying dynamics of triplet excitons during electrical excitation and during OLED degradation. MFEs measurements clearly indicated the presence of TPI under device operation, identified as the main channel for OLED degradation in **Chapter2**. Furthermore, from changes in HFEs of degraded devices, I confirmed that undesired exciton generation, such as interfacial exciplex formation, also reduces the IQE. The MFE analysis can thus nondestructively clarify the dynamics of triplet excitons in devices under operation.

3-5. Appendix A: Input bias dependence of MFEs

The triplet density increases at high current densities, increasing triplet quenching. Therefore, the MFEs should also depend on the applied voltage, and can be used to identify the dynamics of excitons and carriers in the devices. The MFE dependences on current density are shown in **Figure A-1**. The *J*-MR characteristics at 0.5 T showed trends of increasing and decreasing to zero (**Figures A-1b** and **d**). This behaviour was reported by Desai *et al*. previously[25,42]. TPI results in MC because the carrier traps in the system acting as reaction centres are limited and have a maximum at a certain current density. I thus conclude that TPI is one of the reaction channels for triplet exciton.

In contrast to *J*-MR characteristics, the sign of MEL_J changed from positive to negative with increasing current density (**Figures A-1c**). The curve shape of MEL_J (**Figures A-1a**) suggest that TTA in EML is the dominant annihilation process[12,15].

To investigate the effect of triplet exciton lifetimes on current-dependent MFEs, i.e., the contribution of TTA, the injection current dependence of MEL_J of 4CzIPN device was measured (**Figure A-2**). Although the MEL_J of 2CzPN exhibited sign conversion from positive to negative under high current density, the 4CzIPN-based device had only a monotonic increase in MEL_J, which suggests that the TTA is less of an annihilation process in the 4CzIPN-based device relative to the 2CzPN-based device. Therefore, TTA is not a dominant annihilation process in the devices under the low injection current density of 3.0 mA cm^{-2}.

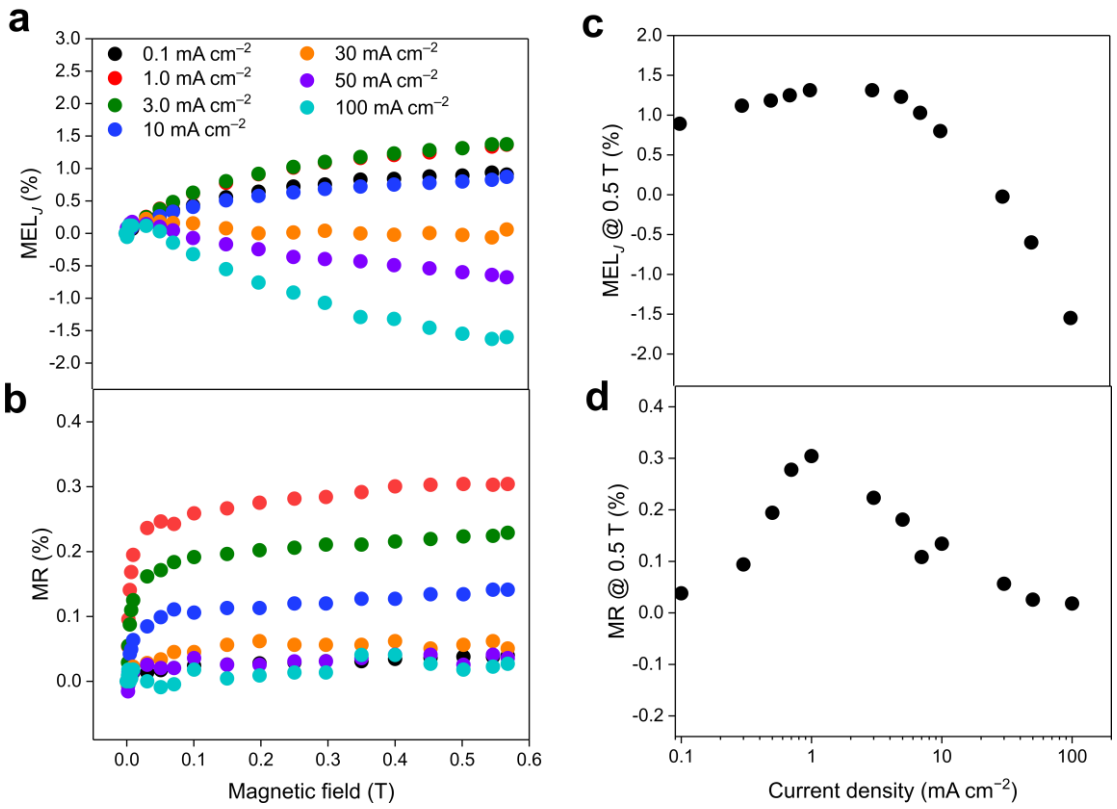

Figure A-1. MFE profiles of 20 wt.%-doped 2CzPN based OLED under various current conditions. (a) MEL$_J$ and (b) MR. Characteristics of *J*-MFE @ 0.5 T. (c) MEL$_J$ and (d) MR.

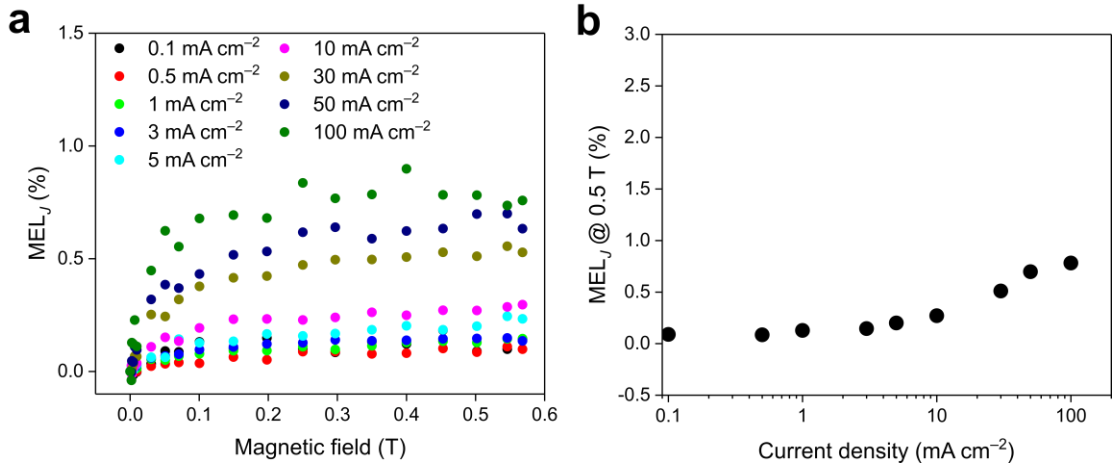

Figure A-2. MEL$_J$ profiles of 20 wt.% 4CzIPN-base under various current conditions and (b) *J*-MEL$_J$ characteristics of 20 wt.% 4CzIPN-based OLED.

3-6. Appendix B: Relative $\Delta I_{EL}(B,t)$ in device degradation

The magneto-electroluminescence, *i.e.*, $MEL_J(B,t)$ under magnetic field, B, at driving time, t, can be expressed by:

$$MEL_J(B,t) = \frac{\Delta I_{EL}(B,t)}{I_{EL}(t)}$$

$\Delta I_{EL}(B,t)$ and $I_{EL}(t)$ are the change in the EL intensity of the device under a magnetic field and the EL intensity without the field, respectively. For a pristine condition, $MEL_J(B,0)$ can be expressed by:

$$MEL_J(B,0) = \frac{\Delta I_{EL}(B,0)}{I_{EL}(0)}$$

$\Delta I_{EL}(B,0)$ and $I_{EL}(0)$ are the change in the EL intensity of device under magnetic field and the EL intensity without the field at the initial condition of device, respectively. $I_{EL}(t)$ of the degraded device is approximately indicated by:

$$I_{EL}(t) = I_{EL}(0) \times \frac{L}{L_0}$$

L/L_0 is the relative luminance. Therefore, the relative change in the EL intensity during degradation based on the EL intensity of the pristine device, *i.e.*, $\Delta I_{EL}(B,t)/I_{EL}(0)$, can be expressed by:

$$\frac{\Delta I_{EL}(B,t)}{I_{EL}(0)} = MEL_J(B,t) \times \frac{L}{L_0}$$

The products of L/L_0 and the amplitudes of LFE and HFE, *i.e.*, A_L and A_H, should be the factors that correspond to $\Delta I_{EL}(B,t)/I_{EL}(0)$s. In **Figure B-1**, non-linear relationships between those factors and L/L_0 were observed in contrast to simple factors such as A_L and A_H (**Figure 3-10**).

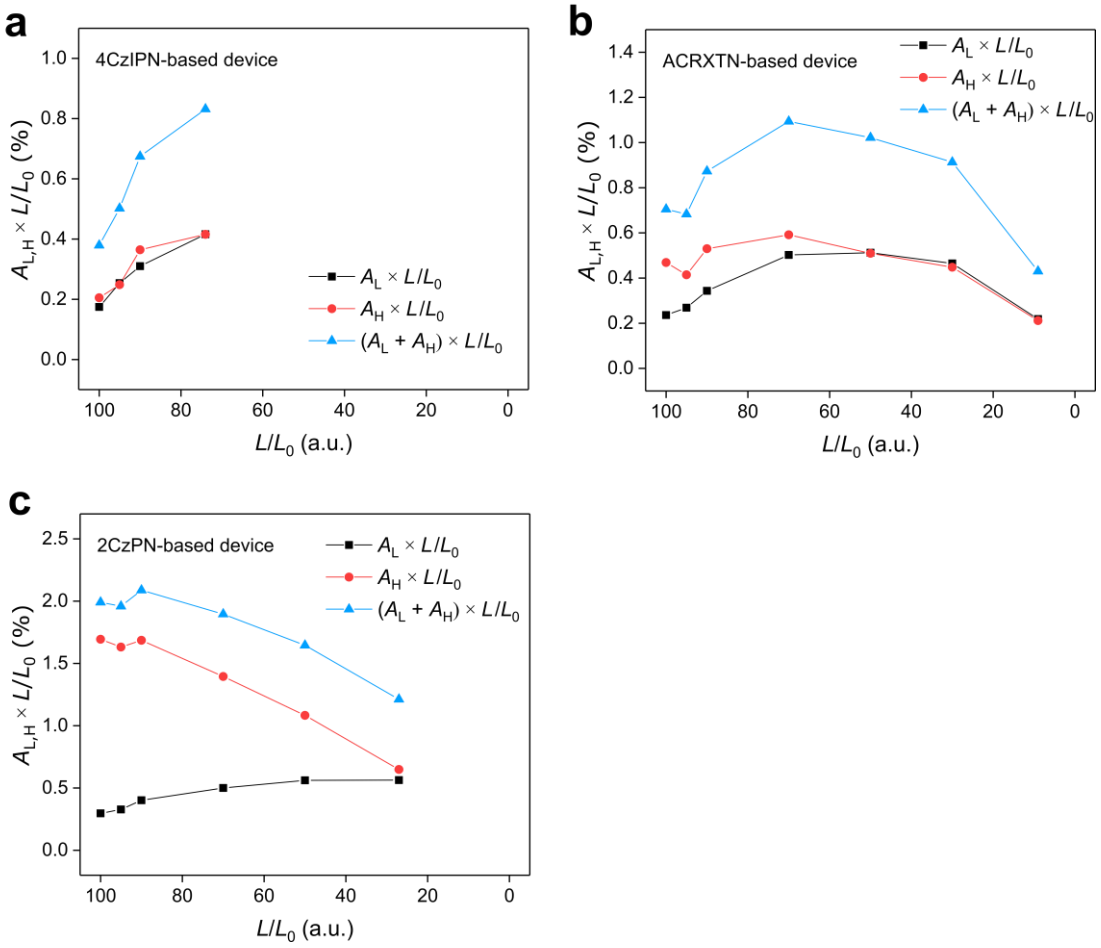

Figure B-1. Change in factors corresponding to the relative $\Delta I_{EL}(B,t)/I_{EL}(0)$s of pristine and degraded devices with based on (a) 4CzIPN, (b) ACRXTN, and (c) 2CzPN.

References

1. D. Y. Kondakov, W. C. Lenhart & W. F. Nichols, Operational degradation of organic light-emitting diodes: Mechanism and identification of chemical products. *J. Appl. Phys.* **101**, 024512 (2007).
2. D. Y. Kondakov, Role of chemical reactions of arylamine hole transport materials in operational degradation of organic light-emitting diodes. *J. Appl. Phys.* **104**, 084520 (2008).
3. S. Scholz, D. Kondakov, B. Lüssem & K. Leo, Degradation mechanisms and reactions in organic light-emitting devices. *Chem. Rev.* **115**, 8449–8503 (2015).
4. Y. Noguchi, H. J. Kim, R. Ishino, K. Goushi, C. Adachi, Y. Nakayama & H. Ishii, Charge carrier dynamics and degradation phenomena in organic light-emitting diodes doped by a thermally activated delayed fluorescence emitter. *Org. Electron.* **17**, 184–191 (2015).
5. N. C. Giebink, B. W. D'Andrade, M. S. Weaver, J. J. Brown & S. R. Forrest, Direct evidence for degradation of polaron excited states in organic light emitting diodes. *J. Appl. Phys.* **105**, 124514 (2009).
6. J. Lee, C. Jeong, T. Batagoda, C. Coburn, M. E. Thompson & S. R. Forrest, Hot excited state management for long-lived blue phosphorescent organic light-emitting diodes. *Nat. Commun.* **8**, 15566 (2017).
7. W. Song & J. Y. Lee, Degradation Mechanism and Lifetime Improvement Strategy for Blue Phosphorescent Organic Light-Emitting Diodes. *Adv. Opt. Mater.* **5**, 1600901 (2017).
8. M. A. Baldo, C. Adachi & S. R. Forrest, Transient analysis of organic electrophosphorescence. II. Transient analysis of triplet-triplet annihilation. *Phys.*

Rev. B. **62**, 10967–10977 (2000).

9. M. Tanaka, H. Noda, H. Nakanotani & C. Adachi, Effect of Carrier Balance on Device Degradation of Organic Light-Emitting Diodes Based on Thermally Activated Delayed Fluorescence Emitters. *Adv. Electron. Mater.* **5**, 1800708 (2019).
10. J. Kalinowski, M. Cocchi, D. Virgili, P. Di Marco & V. Fattori, Magnetic field effects on emission and current in Alq_3-based electroluminescent diodes. *Chem. Phys. Lett.* **380**, 710–715 (2003).
11. Q. Peng, X. Li & F. Li, Time-resolved spin-dependent processes in magnetic field effects in organic semiconductors. *J. Appl. Phys.* **112**, 114512 (2012).
12. J. Zhou, P. Chen, X. Wang, Y. Wang, Y. Wang, F. Li, M. Yang, Y. Huang, J. Yu & Z. Lu, Charge-transfer-featured materials - Promising hosts for fabrication of efficient OLEDs through triplet harvesting via triplet fusion. *Chem. Commun.* **50**, 7586–7589 (2014).
13. J. Kalinowski, M. Cocchi, D. Virgili, V. Fattori & P. Di Marco, Magnetic field effects on organic electrophosphorescence. *Phys. Rev. B.* **70**, 205303 (2004).
14. Y. Lei, Q. Zhang, L. Chen, Y. Ling, P. Chen, Q. Song & Z. Xiong, Ultralarge Magneto-Electroluminescence in Exciplex-Based Devices Driven by Field-Induced Reverse Intersystem Crossing. *Adv. Opt. Mater.* **4**, 694–699 (2016).
15. J. Deng, W. Jia, Y. Chen, D. Liu, Y. Hu & Z. Xiong, Guest concentration, bias current, and temperature-dependent sign inversion of magneto-electroluminescence in thermally activated delayed fluorescence devices. *Sci. Rep.* **7**, 44396 (2017).
16. R. Pan, X. Tang, Y. Hu, H. Zhu, J. Deng & Z. Xiong, Extraordinary magnetic field

effects mediated by spin-pair interaction and electron mobility in thermally activated delayed fluorescence-based OLEDs with quantum-well structure. *J. Mater. Chem. C.* **7**, 2421–2429 (2019).

17. V. N. Prigodin, J. D. Bergeson, D. M. Lincoln & A. J. Epstein, Anomalous room temperature magnetoresistance in organic semiconductors. *Synth. Met.* **156**, 757–761 (2006).

18. T. L. Keevers, W. J. Baker & D. R. McCamey, Theory of exciton-polaron complexes in pulsed electrically detected magnetic resonance. *Phys. Rev. B.* **91**, 205206 (2015).

19. A. H. Devir-Wolfman, B. Khachatryan, B. R. Gautam, L. Tzabary, A. Keren, N. Tessler, Z. V. Vardeny & E. Ehrenfreund, Short-lived charge-transfer excitons in organic photovoltaic cells studied by high-field magneto-photocurrent. *Nat. Commun.* **5**, 4529 (2014).

20. T. Ogiwara, Y. Wakikawa & T. Ikoma, Mechanism of intersystem crossing of thermally activated delayed fluorescence molecules. *J. Phys. Chem. A.* **119**, 3415–3418 (2015).

21. E. W. Evans, Y. Olivier, Y. Puttisong, W. K. Myers, T. J. H. Hele, S. M. Menke, T. H. Thomas, D. Credgington, D. Beljonne, R. H. Friend & N. C. Greenham, Vibrationally Assisted Intersystem Crossing in Benchmark Thermally Activated Delayed Fluorescence Molecules. *J. Phys. Chem. Lett.* **9**, 4053–4058 (2018).

22. D. Y. Kondakov, T. D. Pawlik, T. K. Hatwar & J. P. Spindler, Triplet annihilation exceeding spin statistical limit in highly efficient fluorescent organic light-emitting diodes. *J. Appl. Phys.* **106**, 124510 (2009).

23. D. Song, S. Zhao, Y. Luo & H. Aziz, Causes of efficiency roll-off in

phosphorescent organic light emitting devices: Triplet-triplet annihilation versus triplet-polaron quenching. *Appl. Phys. Lett.* **97**, 243304 (2010).

24. M. Inoue, T. Serevičius, H. Nakanotani, K. Yoshida, T. Matsushima, S. Juršenas & C. Adachi, Effect of reverse intersystem crossing rate to suppress efficiency roll-off in organic light-emitting diodes with thermally activated delayed fluorescence emitters. *Chem. Phys. Lett.* **644**, 62–67 (2016).
25. M. Cox, P. Janssen, F. Zhu & B. Koopmans, Traps and trions as origin of magnetoresistance in organic semiconductors. *Phys. Rev. B.* **88**, 035202 (2013).
26. V. Ern & R. E. Merrifield, Magnetic field effect on triplet exciton quenching in organic crystals. *Phys. Rev. Lett.* **21**, 609–611 (1968).
27. M. Wittmer & I. Zschokke-Gränacher, Exciton-charge carrier interactions in the electroluminescence of crystalline anthracene. *J. Chem. Phys.* **63**, 4187–4194 (1975).
28. H. Nakanotani, K. Masui, J. Nishide, T. Shibata & C. Adachi, Promising operational stability of high-efficiency organic light-emitting diodes based on thermally activated delayed fluorescence. *Sci. Rep.* **3**, 2127 (2013).
29. H. Nakanotani, T. Higuchi, T. Furukawa, K. Masui, K. Morimoto, M. Numata, H. Tanaka, Y. Sagara, T. Yasuda & C. Adachi, High-efficiency organic light-emitting diodes with fluorescent emitters. *Nat. Commun.* **5**, 4016 (2014).
30. K. Masui, H. Nakanotani & C. Adachi, Analysis of exciton annihilation in high-efficiency sky-blue organic light-emitting diodes with thermally activated delayed fluorescence. *Org. Electron.* **14**, 2721–2726 (2013).
31. H. Fukagawa, T. Shimizu, T. Kamada, S. Yui, M. Hasegawa, K. Morii & T. Yamamoto, Highly efficient and stable organic light-emitting diodes with a greatly

reduced amount of phosphorescent emitter. *Sci. Rep.* **5**, 9855 (2015).

32. J. Nishide, H. Nakanotani, Y. Hiraga & C. Adachi, High-efficiency white organic light-emitting diodes using thermally activated delayed fluorescence. *Appl. Phys. Lett.* **104**, 233304 (2014).

33. S. T. Hoffmann, P. Schro, M. Rothmann, R. Q. Albuquerque, P. Strohriegl & A. Ko, Triplet Excimer Emission in a Series of 4,4′-Bis(N-carbazolyl)-2,2′-biphenyl Derivatives. *J. Phys. Chem. B.* **115**, 414–421 (2011).

34. S. A. Bagnich, S. Athanasopoulos, A. Rudnick, P. Schroegel, I. Bauer, N. C. Greenham, P. Strohriegl & A. Köhler, Excimer formation by steric twisting in carbazole and triphenylamine-based host materials. *J. Phys. Chem. C*. **119**, 2380–2387 (2015).

35. J. Kalinowski, G. Giro, M. Cocchi, V. Fattori & P. Di Marco, Unusual disparity in electroluminescence and photoluminescence spectra of vacuum-evaporated films of 1,1-bis ((di-4-tolylamino) phenyl) cyclohexane. *Appl. Phys. Lett.* **76**, 2352–2354 (2000).

36. P. Yuan, X. Qiao, D. Yan & D. Ma, An inversion of magnetic field effects in electromer-based organic light-emitting diodes. *J. Mater. Chem. C*. **7**, 1035–1041 (2019).

37. T. Granlund, L. A. A. Pettersson, M. R. Anderson & O. Inganäs, Interference phenomenon determines the color in an organic light emitting diode. *J. Appl. Phys.* **81**, 8097–8104 (1997).

38. T. D. Schmidt, L. Jäger, Y. Noguchi, H. Ishii & W. Brütting, Analyzing degradation effects of organic light-emitting diodes via transient optical and electrical measurements. *J. Appl. Phys.* **117**, 215502 (2015).

39. W. Song, T. Kim, J. Y. Lee, Y. Lee & H. Jeong, Investigation of degradation mechanism of phosphorescent and thermally activated delayed fluorescent organic light-emitting diodes through doping concentration dependence of lifetime. *J. Ind. Eng. Chem.* **68**, 350–354 (2018).

40. J. Sohn, D. Ko, H. Lee, J. Han, S. D. Lee & C. Lee, Degradation mechanism of blue thermally activated delayed fluorescent organic light-emitting diodes under electrical stress. *Org. Electron.* **70**, 286–291 (2019).

41. C. Féry, B. Racine, D. Vaufrey, H. Doyeux & S. Ciǹ, Physical mechanism responsible for the stretched exponential decay behavior of aging organic light-emitting diodes. *Appl. Phys. Lett.* **87**, 213502 (2005).

42. P. Desai, P. Shakya, T. Kreouzis, W. P. Gillin, N. A. Morley & M. R. J. Gibbs, Magnetoresistance and efficiency measurements of Alq_3-based OLEDs. *Phys. Rev. B* **75**, 094423 (2007).

Chapter 4

Molecular orientation of disk-shaped small molecules exhibiting thermally activated delayed fluorescence in host-guest films

Masaki Tanaka, Hiroki Noda, Hajime Nakanotani and Chihaya Adachi

Applied Physics Letters, **116**, 023302 (2020)

Abstract

Control of the molecular orientation in a glassy film is a crucial issue, not only for an understanding of the fundamental processes of organic amorphous film formation but also for enhancement of the performance of OLEDs by increasing their light-outcoupling efficiency. In this study, the molecular orientation in codeposited films composed of a host molecule and a disk-shaped emitter that exhibits TADF is investigated systematically. It is found that the orientation of the transition dipole moment (TDM) of the disk-shaped emitters is strongly dependent on the glass transition temperature and the polarization of the host molecules and almost perfectly horizontal orientation of the TDM of the disk-shaped emitters can be realized. My findings clarify the role of the host-guest dipole-dipole interaction in the molecular orientation and it will enable expansion of both the molecular design and the material combination rules for high-performance OLEDs.

4-1. Introduction

In **Chapters 2** and **3**, I discussed degradation mechanisms, especially, triplet-exciton interactions in TADF-OLEDs. Further, the improvement of light-outcoupling efficiency (η_{OC}) is one of the simplest ways to increase EQE and decrease operational current density, *i.e.*, low electrical stress under device operation, resulting in a lenghtend device lifetime. Although vapor-deposited small organic molecules were believed to be deposited randomly in these glassy films, it has been found that the molecules that have a large aspect ratio in their shapes, *i.e.*, linear-shaped molecules, can show horizontal orientations on a substrate even in a glassy film[1,2]. For OLED performances, particularly for enhancement of the η_{OC}, which is a limiting factor for the EQE[3], molecular orientation control is essential because it provides the transition dipole moment (TDM) orientation of the emitting molecules. Over the last decade, the TDM orientation mechanisms of emitters in amorphous films have been investigated widely[1–4] and it has been shown that various emitters exhibit horizontal TDM orientations in amorphous thin films[5–12].

This molecular orientation behavior also indicates that a permanent dipole moment (PDM) can be oriented simultaneously if the molecule has polarization. Spontaneous PDM ordering, *i.e.*, spontaneous orientation polarization (SOP) of organic molecules with anisotropic shapes, leads to the formation of polar films with a high surface potential called the giant surface potential (GSP)[13,14]. Therefore, the molecular orientation will also critically affect charge carrier injection and accumulation properties in OLEDs[14–16].

Although the detailed mechanism for ordering of the molecules remains unclear, possible mechanisms including intermolecular dipole-dipole interactions (long-range interactions) and van der Waals interactions between molecules and a surface during deposition (short-range interactions) have been proposed and studied experimentally and

computationally[14–19]. Furthermore, it has been widely accepted that linear-shaped molecules preferentially show horizontal TDM orientation because of the orientations of their long molecular axes on substrates. However, studies of the TDM and PDM orientations of non-linear-shaped but disk-shaped molecules that exhibit TADF are in their early stages[20], while OLEDs based on disk-shaped TADF emitters have demonstrated excellent device performance[21]. Therefore, in this study, I investigated the TDM and PDM orientations of various disk-shaped TADF emitters in host-guest systems systematically using angular-dependent PL measurements and displacement current measurement (DCM) techniques. I compared various combinations of emitters and host matrices with different PDMs and found that the TDM orientations of the disk-shaped molecules could be controlled toward horizontal alignment by tuning the glass transition temperature and polarization of the host matrix in glassy host-guest systems; this will lead to advanced molecular design rules for high-performance OLEDs.

4-2. Experimental

4-2-1. Materials

The molecular structures of the emitter and host molecules used in this study and the PDMs of the guest emitter molecules (p_G) and the host molecules (p_H) calculated using Gaussian 09 program package with a basis set of B3LYP/6-31G (d) for the ground state are summarized in **Figures 4-1** and **4-2**. 1,4-dicyano-2,3,5,6-tetrakis(carbazol-9-yl)benzene (4CzTPN), 1,4-dicyano-2,3,5,6-tetrakis(3,6-diphenylcarbazol-9-yl)benzene (4CzTPN-Ph) and 1,4-dicyano-2,5-bis(carbazol-9-yl)benzene (2CzTPN) were used as the molecules with small or zero polarization because of their symmetrical structures, whereas 2,3,5,6-tetrakis(carbazol-9-yl)benzonitrile (4CzBN), 2,3,5,6-tetrakis(carbazol-9-yl)-4-phenylbenzonitrile (4CzBN-Ph), 2,3,5,6-tetrakis(carbazol-9-yl)-4-(9,9-dimethylfluoren-3-yl)benzonitrile (4CzBN-Flu) and 1,2,3,4-tetrakis(carbazol-9-yl)-5,6-dicyanobenzene (4CzPN) had larger PDMs, *i.e.*, >1 D. 4,4'-di(9H-carbazol-9-yl)-1,1'-biphenyl (CBP) and 1,3,5-tris(1-phenyl-1H-benzo[d]imidazol-2-yl)benzene (TPBi) were used as the hosts with nonpolar and polar characteristics, respectively.

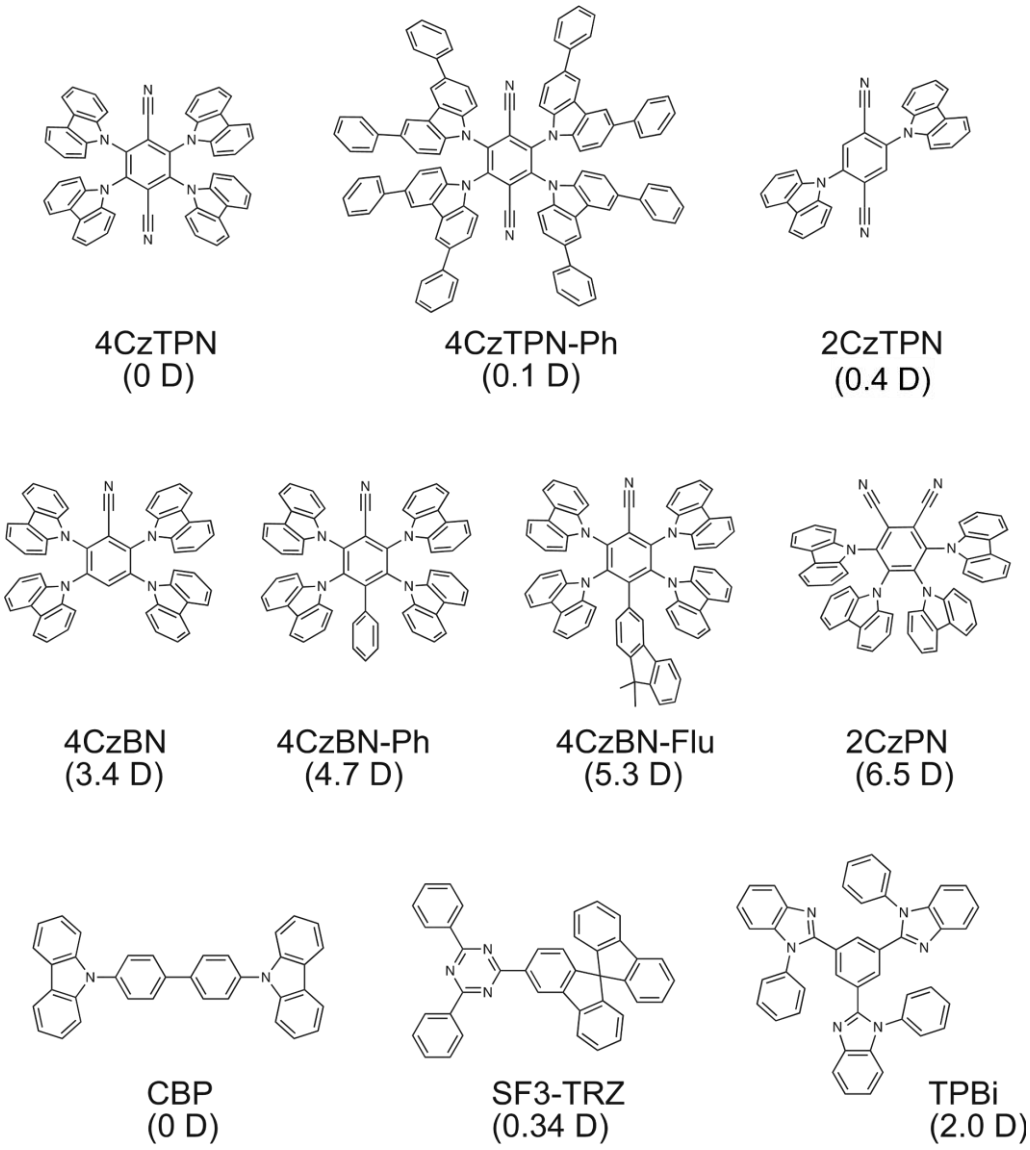

Figure 2. Molecular structures and calculated permanent dipole moments (p_G and p_H) of disk-shaped TADF emitters and host molecules.

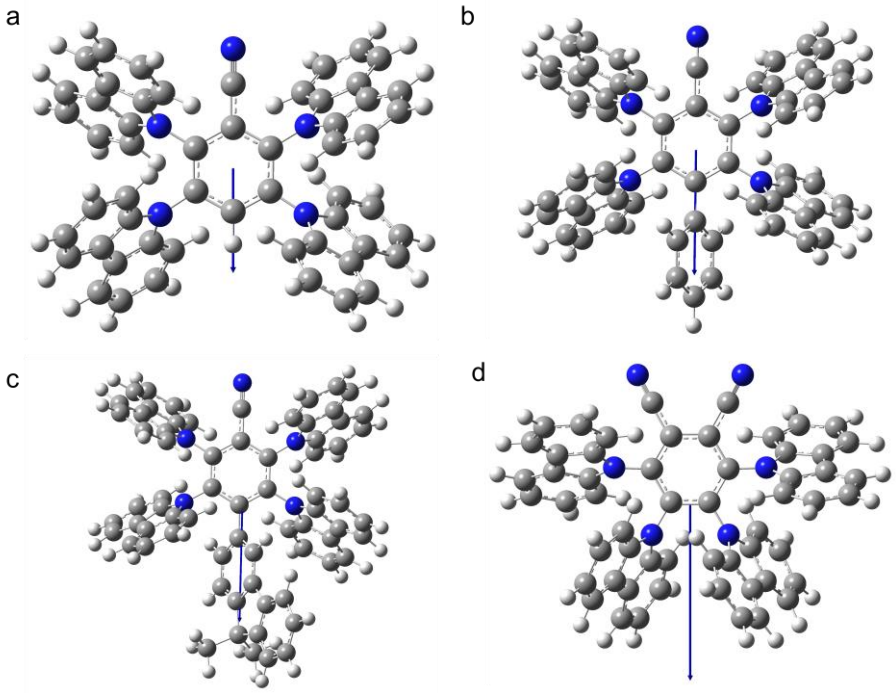

Figure 4-2. Directions of permanent dipoles of (a) 4CzBN, (b) 4CzBN-Ph, (c) 4CzBN-Flu and (d) 4CzPN. With regard to molecules with major conformers, the more stable structures in **Figure C-1** were used for this calculation.

Computational calculations of the molecular geometry revealed that some of the TADF molecules, including 4CzTPN, 4CzTPN-Ph, 2CzTPN and 4CzBN, have two major conformers with completely different angles for their carbazole moieties, as shown in **Figures C-1** and **C-2** (see **Appendix C**). In the 2CzTPN case, the averaged PDM values of several conformers weighted by existence ratios estimated using the Boltzmann distribution along with their calculated energies were used as shown in **Figure C-2**. For the other molecules, the PDMs of the most stable structures were used. Although TPBi also has two major conformers that show completely different PDMs, as indicated by Noguchi *et al.*[14], the more stable molecular structure was used in this study (**Figure C-3**).

4-2-2. Angular-dependent PL measurement

Angular-dependent PL measurements were performed using an H14234-01 (Hamamatsu Photonics) at an excitation wavelength of 365 nm (**Figure 4-3**)[7]. The samples were 15-nm-thick doped organic films on glass substrates fabricated *via* vacuum deposition. The order parameters (S) of the emitters were estimated by comparing the angle profiles given by the experimental and simulated results using an optical simulator (Setfos). The S value is given by

$$S = \frac{1}{2}\langle 3\cos^2\theta \rangle$$

where θ is the angle between the transition dipole and the substrate normal.

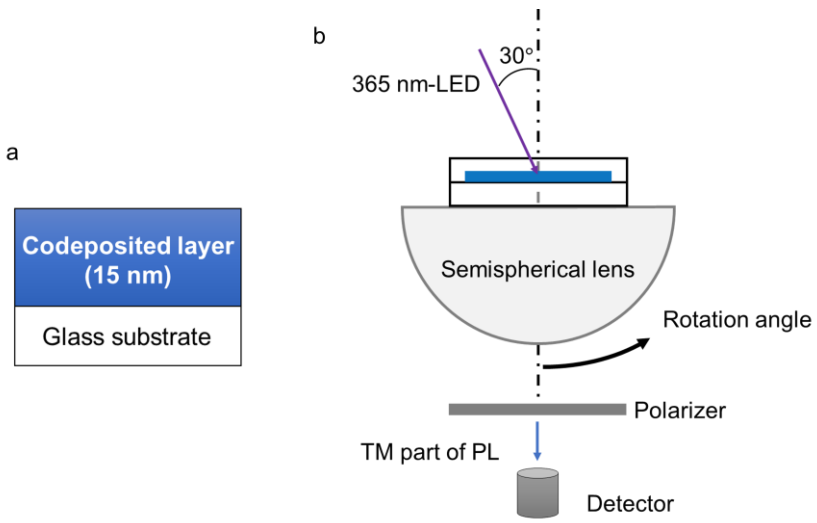

Figure 4-3. (a) Sample configuration for angular-dependent PL measurements, (b) Measurement setup for angular-dependent PL measurements.

4-2-3. DCM method

The carrier injection and accumulation properties of the two-layer devices were investigated using the DCM method. The device structures with active area (A) of 4 mm^2 are shown in **Figure 4-4a**. A voltage with a triangular waveform was applied to the devices using a function generator (WaveStation 2052, Teledyne Lecroy), and their current responses were measured using a voltage/current amplifier (CA5350, NF Corporation) and an oscilloscope (HDO4054A, Teledyne Lecroy). The triangular waveform ramp rate was 100 V s^{-1} and the voltage ranges were varied for each sample because of their different surface charge densities.

Figures 4-4b and **c** show the typical DCM profiles of devices based on the undoped TPBi and CBP films. Because of the negative charges at the interface between 4,4-bis[*N*-(1-naphthyl)-*N*-phenylamino]-biphenyl (α-NPD) and the polar layers, e.g., TPBi, hole injection and accumulation at the interfaces were observed in the DCM profiles. I defined the accumulation voltage and the threshold voltage of the actual current as V_{acc} and V_{th}, respectively. The surface charge density (σ_S) can be calculated as follows:

$$\sigma_S = (V_{acc} - V_{th})\frac{\varepsilon_0 \varepsilon_r}{d} = (V_{acc} - V_{th})\frac{C_{codeposited}}{A}$$

where d is the film thickness of the codeposited layers, which is 60 nm here. $C_{codeposited}$, ε_0 and ε_r are the codeposited layer capacitance, the vacuum permitivity and the relative permitivity of the codeposited films, respectively. Here, when calculating σ_S, use of the $C_{codeposited}$ and A values is more relevant than use of ε_r and d because of the value of ε_r of each codeposited film is experimentally inaccessible[15].

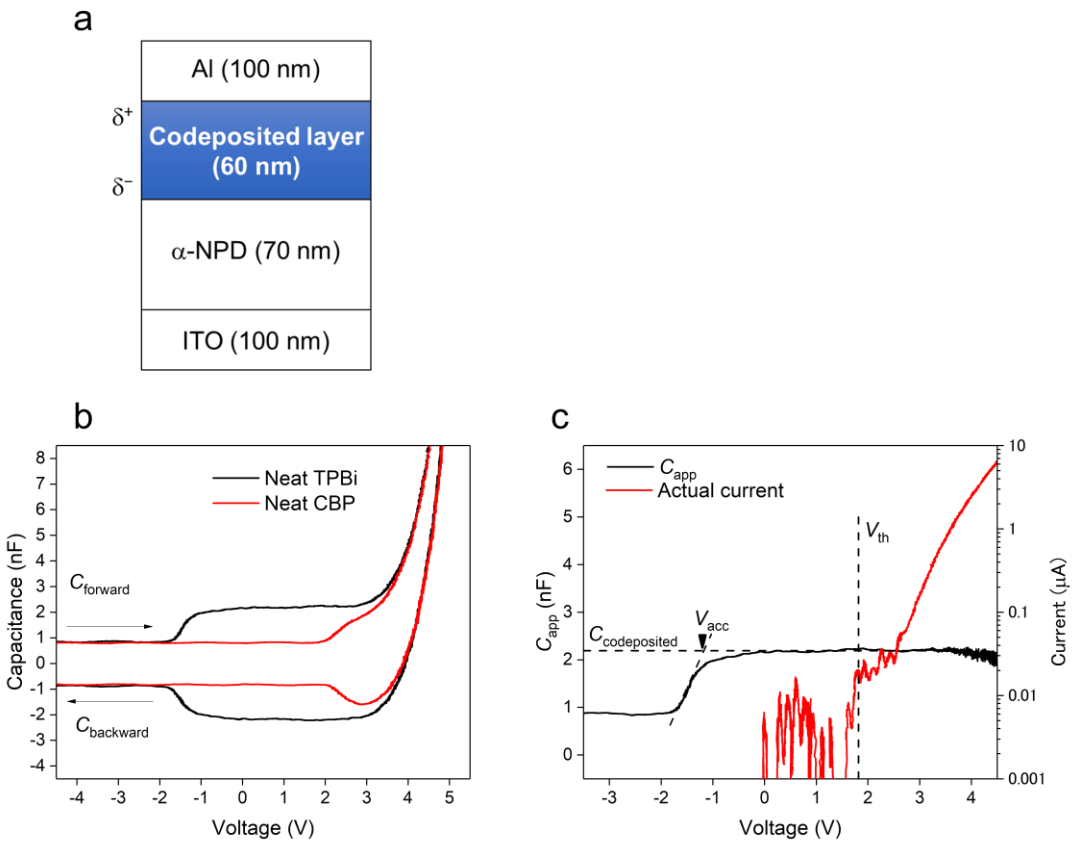

Figure 4-4. (a) Device structure used for DCM measurements. ITO and a-NPD are indium tin oxide and 4,4-bis[*N*-(1-naphthyl)-*N*-phenylamino]-biphenyl, respectively. (b) DCM profiles of devices based on undoped CBP- and TPBi films. (c) Detailed analysis to determine values of $C_{codeposited}$, V_{acc} and V_{th}. The apparent capacitance (C_{app}) and actual current (J_{act}) in **Figure 4-4c** are given by $\boldsymbol{C_{app} = (C_{forward} - C_{backward})/2}$ and $\boldsymbol{J_{act} = (C_{forward} + C_{backward})/2}$, respectively. $C_{forward}$ and $C_{backward}$ are DCM signals of forward and backward scans, respectively (**Figure 4b**).

4-3. Results

4-3-1. Angular-dependent PL measurement

The *S* values of the test samples are summarized in **Table 4-1** and **Figure 4-5**. Here, note that the directions of the TDM vectors of these molecules are oriented parallel to the central phenyl ring (**Figure 4-6**). For emitters doped into a CBP host, the TDM orientations of both 4CzBN and 2CzTPN were shown to be completely random (*S*~0), whereas the TDMs of the other emitters showed relatively good horizontal orientations. The random orientations of the 4CzBN and 2CzTPN emitters were caused by the presence of unsubstituent positions on the central phenyl unit. Free rotation of the carbazole units is possible during film formation and causes randomization of the molecular orientation (**Figure C-2**).

Table 4-1. *S* values of the emitters in 20 wt.%-doped films in two host materials

Host	4CzTPN	4CzTPN-Ph	2CzTPN
CBP	−0.29	−0.50	−0.01
TPBi	−0.37	−0.49	−0.27

Host	4CzBN	4CzBN-Ph	4CzBN-Flu	4CzPN
CBP	−0.10	−0.29	−0.31	−0.29
TPBi	−0.23	−0.40	−0.40	−0.37

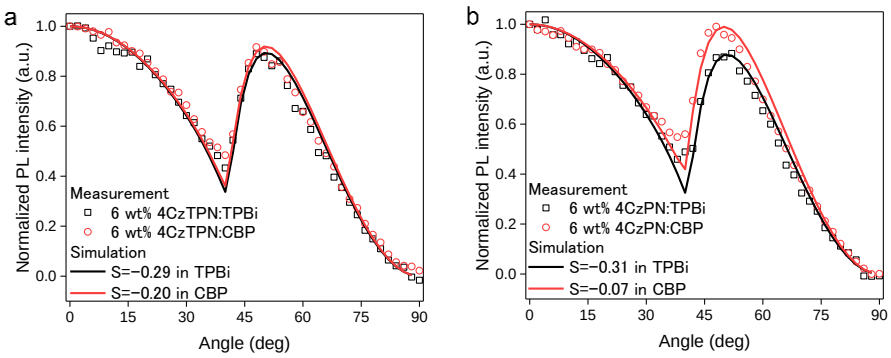

Figure 4-5. Angular-dependent PL profiles of (a) 4CzTPN and (b) 4CzPN as emitters in different hosts.

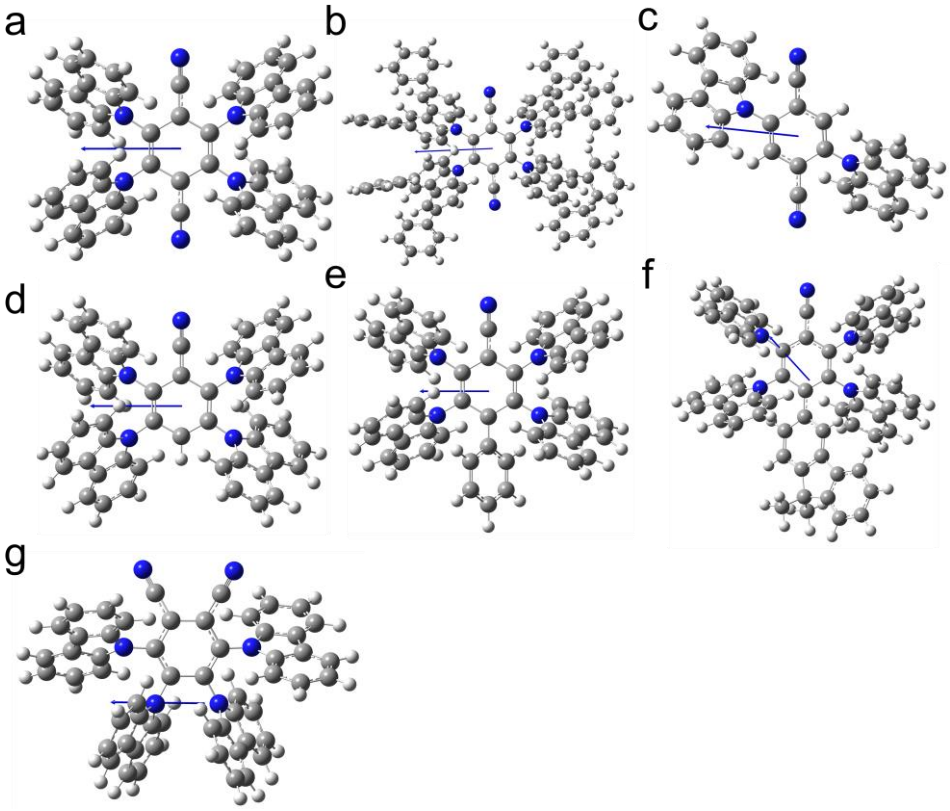

Figure 4-6. Directions of transition dipoles of (a) 4CzTPN, (b) 4CzTPN-Ph, (c) 2CzTPN, (d) 4CzBN, (e) 4CzBN-Ph, (f) 4CzBN-Flu and (g) 4CzPN. Blue arrows indicate the direction of the transition dipole. With regard to molecules with major conformers, the structure-(1) types in **Figure C-1** were used for this calculation. For the calculation, time-dependent density functional theory (TD-DFT) and CAM-B3LYP/6-31G (d) methods using optimized ground state geometries was used.

4CzTPN-Ph achieved $S = -0.5$, thus demonstrating the completely horizontal orientation of the TDM. An OLED based on a 4CzTPN-Ph:CBP codeposited film as an emission layer showed the maximum EQE of 4.6% (**Figure 4-7**), even though the photoluminescence quantum yield of the 20 wt.% 4CzTPN-Ph:CBP film was only 16%. Under the assumption that both the carrier balance and the exciton utilization yields were 100%, the value of η_{OC} reached 29%, thus indicating that the completely horizontal orientation contributes to the enhancement of the light outcoupling efficiency.

The TDM of each emitter in a polar host such as TPBi showed higher horizontal orientation than that of each emitter with the CBP host. The doping concentration dependence of the TDM orientation was also studied using both 4CzPN (6.5 D) and 4CzTPN (0 D) (**Figures 4-8a** and **b**). For each emitter, a high doping concentration resulted in higher horizontal orientation in the CBP host. In contrast, in the TPBi host, a weak doping concentration dependence on the orientation was observed that resulted in a highly horizontal TDM orientation, even at low concentrations, *i.e.*, in a 1 wt.% emitter-doped TPBi film.

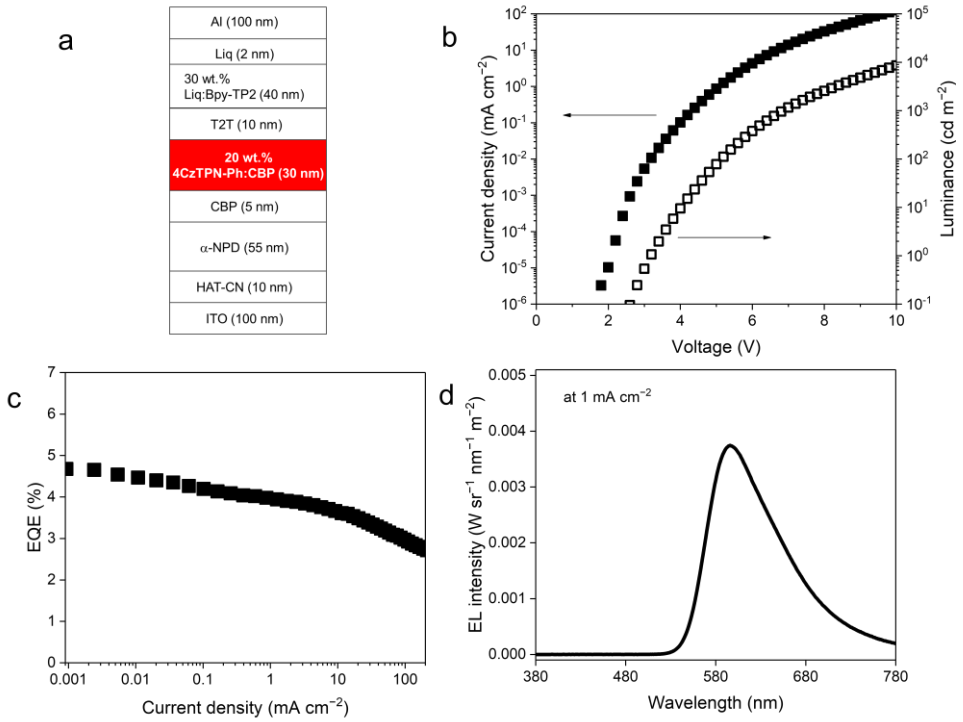

Figure 4-7. (a) OLED device structure based on a 4CzTPN-Ph:CBP film. T2T and BPy-TP2 are 2,4,6-tris(biphenyl-3-yl)-1,3,5-triazine and 2,7-bis(2,20-bipyridine-5-yl)triphenylene, respectively. (b) Current density-luminance-voltage characteristics. (c) EQE-current density characteristics. (d) EL spectrum. The EQE and *J*-*V*-*L* measurements were performed using a calibrated luminance meter (CS-2000, Konica Minolta). EQE values were collected based on the results of angular-dependent EL profile measurements (C9920-11, Hamamatsu Photonics).

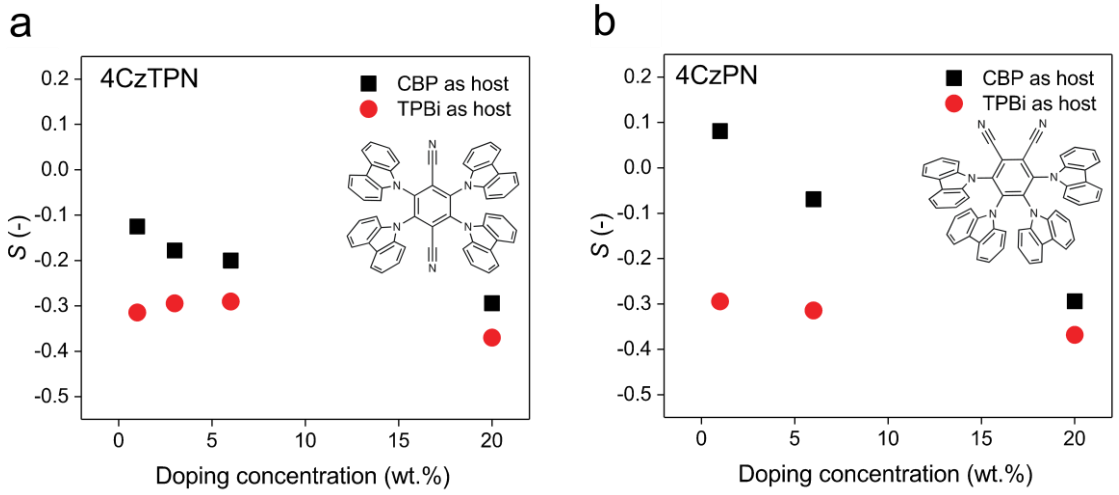

Figure 4-8. (a) and (b) Doping concentration dependences of *S* values of 4CzTPN (inset of **Figure 4-8a**) and 4CzPN (inset of **Figure 4-8b**) in two hosts, respectively.

4-3-2. Evaluation of surface charge density

Figures 4-9a and **b** show the DCM profiles of two-layer devices based on codeposited films composed of 4CzTPN and 4CzPN in CBP and TPBi hosts, respectively. The calculated surface charge densities of these codeposited films (σ_S) were plotted versus the emitter PDM values in **Figures 4-9c** and **d**. In the undoped films, I observed a proportional relationship between the σ_S values and the emitter PDM values, as reported previously by Osada *et al.*[19] The σ_S values of the emitter:CBP doped films were also similar to those of the undoped films and a similar proportional relationship with p_G was also observed. Furthermore, although the numbers of polar emitter molecules in the 20 wt.%-doped CBP film were one-fifth of those in the undoped films, the σ_S values of the emitter:CBP films were greater than 20% of the corresponding values of the undoped films, thus indicating that σ_S showed a nonlinear relationship with the number of polar molecules. These results can be understood based on the discussion of the manner of dipole-pair formation proposed by Jäger *et al.*[15] Here, the dipole-dipole interaction energies of parallel-pair ($U_{\uparrow\uparrow}$) and antiparallel-pair ($U_{\uparrow\downarrow}$) are given by

$$U_{\uparrow\uparrow} = -\frac{p^2}{4\pi\varepsilon_0 r^3}(3\cos\beta - 1) \;\; and \;\; U_{\uparrow\downarrow} = -U_{\uparrow\uparrow}$$

where p is the permanent dipole moment of each molecule, and r is the distance between two dipoles, and β is the angle between the direction of dipoles and the line connecting them as shown in **Figure 4-10a**. As a result of the spatial separation of the polar emitters in the codeposited films caused by the presence of nonpolar host molecules, the dipole-dipole interactions should be reduced and the formation of the anti-parallel dipole-pairs that counteract the molecular polarity should be suppressed. The formed parallel pairs can then increase σ_S for the doped films (**Figure 4-10b**).

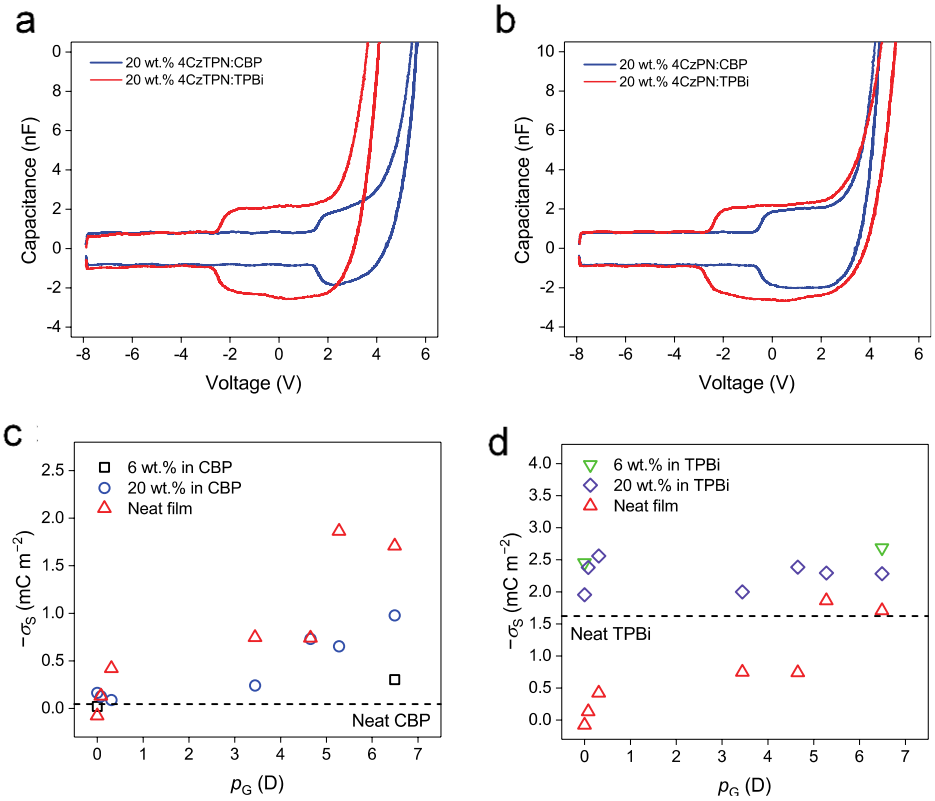

Figure 4-9. DCM profiles of two-layer devices based on (a) 4CzTPN and (b) 4CzPN. (c) and (d) Relationships between surface charge densities (σ_S) of the codeposited layers and p_G.

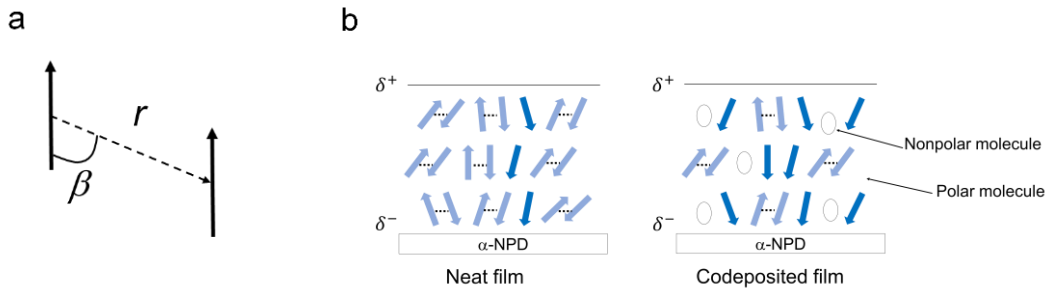

Figure 4-10. (a) Schematic of dipole-dipole interaction. **(**b) Schematics of formation of dipole-dipole pairs in an undoped film of polar molecules and in a codeposited film based on nonpolar and polar molecules. Arrows represent the permanent dipole vectors. For the undoped film, dipole interactions promote the formation of anti-parallel pairs. In contrast, the nonpolar molecules provide a spatial distance between the polar molecules to prevent the formation of anti-parallel pairs in the codeposited film.

For the TPBi host matrix, the σ_S values of all codeposited films were greater than that of the undoped TPBi film. While the σ_S values of codeposited films based on the nonpolar emitters (4CzTPN, 4CzTPN-Ph and 2CzTPN) were greater than the sum of σ_S(neat TPBi) + σ_S(neat TADF), the σ_S values based on highly polar molecules were smaller than σ_S(neat TPBi) + σ_S(neat TADF). Furthermore, the emitter dependence of σ_S for the TPBi host was rather small when compared with the values for the CBP hosts, indicating the presence of different host-guest interactions in the polar TPBi host layer.

4-4. Discussion

4-4-1. Horizontal orientation of TDM in host matrix

Next, I discuss the origin of the TDM orientations of the disk-shaped molecules in codeposited films. Mayr and Brütting reported that one of the most important factors for TDM orientation of the guest molecules is the glass transition temperature (T_g) of the host matrix[5]. A high T_g for the host materials results in suppression of guest molecule reorientation and randomization during deposition, and results in horizontal orientation of the guest molecules due to minimization of the film's surface energy during deposition. The T_g values of CBP and TPBi are 62°C and 122°C, respectively. To confirm the effect of the host T_g, another high-T_g host with low polarization (0.34 D, **Figure 4-11**), 2-(9,9′-spirobi[fluoren]-3-yl)-4,6-diphenyl-1,3,5-triazine (SF3-TRZ)[22] with a T_g of 135°C was also used as a host for 4CzTPN, 2CzTPN, 4CzBN and 4CzPN, and the *S* values of the emitter: SF3-TRZ films are summarized in **Table 4-2** and **Figure 4-12**. For the nonpolar emitters, 4CzTPN and 2CzTPN, in the SF3-TRZ host, smaller *S* values than those in CBP and TPBi were confirmed, indicating that the higher T_g clearly affects the molecular orientations of the 'nonpolar' TADF emitters. In contrast, the *S* values of the 'polar' emitters in SF3-TRZ showed comparable values with those in the CBP host. This implies that there are other underlying origins of the horizontal orientation in the TPBi host, rather than the effect of T_g alone.

Table 4-2. *S* values of TADF emitters in SF3-TRZ as host.

	4CzTPN (20 wt.%)	2CzTPN (20 wt.%)	4CzBN (20 wt.%)	4CzPN (6 wt.%)	4CzPN (20 wt.%)
S (-)	−0.41	−0.29	−0.10	−0.21	−0.29

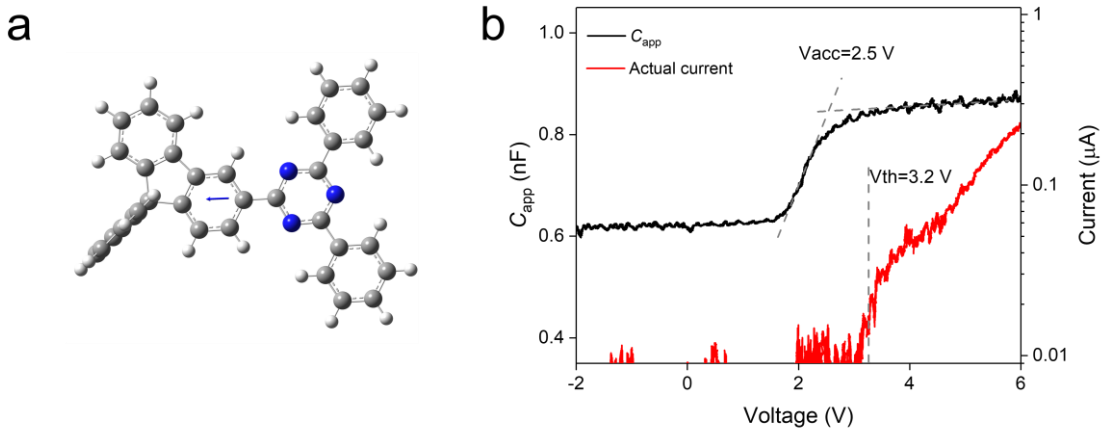

Figure 4-11. (a) Computational results for SF3-TRZ molecule. The blue arrow represents the PMD vector of the molecule. (b) Results of DCM study of ITO (100 nm)/a-NPD (30 nm)/SF3-TRZ (120 nm)/Al structure. According to the results, σ_S (SF3-TRZ undoped) is −0.15 mC m^{-2}, which means that the SF3-TRZ molecule acts as a nonpolar molecule and shows a significantly low surface charge.

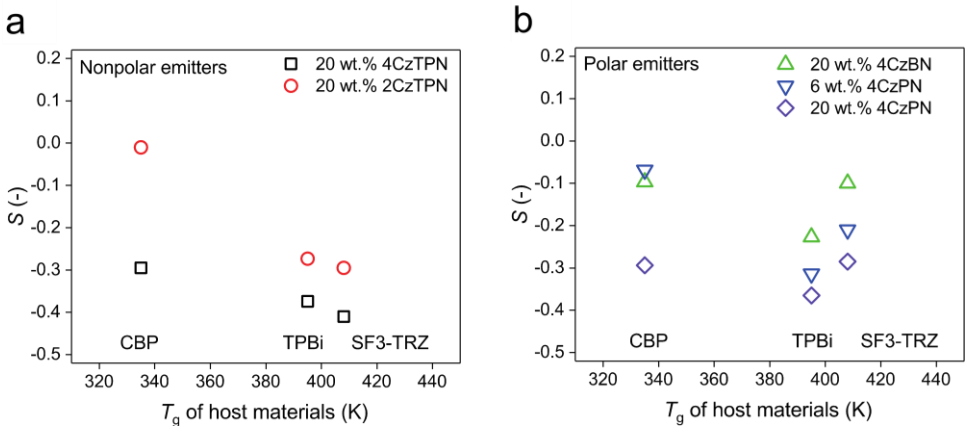

Figure 4-12. (a) and (b) *S* values of nonpolar and polar emitters in hosts with different glass transition temperatures (T_g), respectively.

The observed concentration dependence of the S values in a CBP host can be understood based on the change in T_g for the mixed emitter:CBP systems. The concentration dependence was discussed by Jiang *et al.*[11], who suggested that the difference between the substrate temperature during deposition, T_{sub}, and the T_g of the mixed system, $T_{g,mixed}$, is a critical issue for determination of the orientations of molecules and $T_{g,mixed}$ is strongly dependent on the doping concentration of the mixed system. Although the T_g values of molecules such as 4CzTPN and 4CzPN unfortunately could not be identified because of the similarity of their values to their melting points and decomposition temperatures, I could perform differential scanning calorimetry (DSC) measurements for mixed samples such as an emitter:host system (**Figures 4-13a** and **b**). In fact, the $T_{g,mixed}$ of the TADF emitters:host system showed high or similar values when compared with the host-only system, indicating the high T_g of the TADF emitters. Therefore, because of the large variation of $T_{g,mixed}$ in a CBP host, significant concentration dependences were observed. Furthermore, **Figures 4-13c** and **d** show the relationship between the S values of the emitters and the $T_{g,mixed}$ values of the emitter:host combinations, with similar results to the trends shown in **Figure 4-12**, *i.e.*, a nonlinear relationship for the polar emitters.

Mayr and Brütting also noted a similar host dependence for phosphorescence emitters in the TPBi host[5]. Although computational studies have suggested that dipole-dipole interactions are not the dominant factor for TDM orientation[6], I can infer that the intermolecular dipole-dipole interaction of the host-guest molecules is one possible mechanism by which horizontal orientation is induced. Additionally, I can also speculate that the small but non-negligible polarization of the host molecule slightly disturbs the dipole-dipole interactions between the guest molecules and causes enhancement of the

horizontal TDM orientation of the emitters (**Figure 4-16c**).

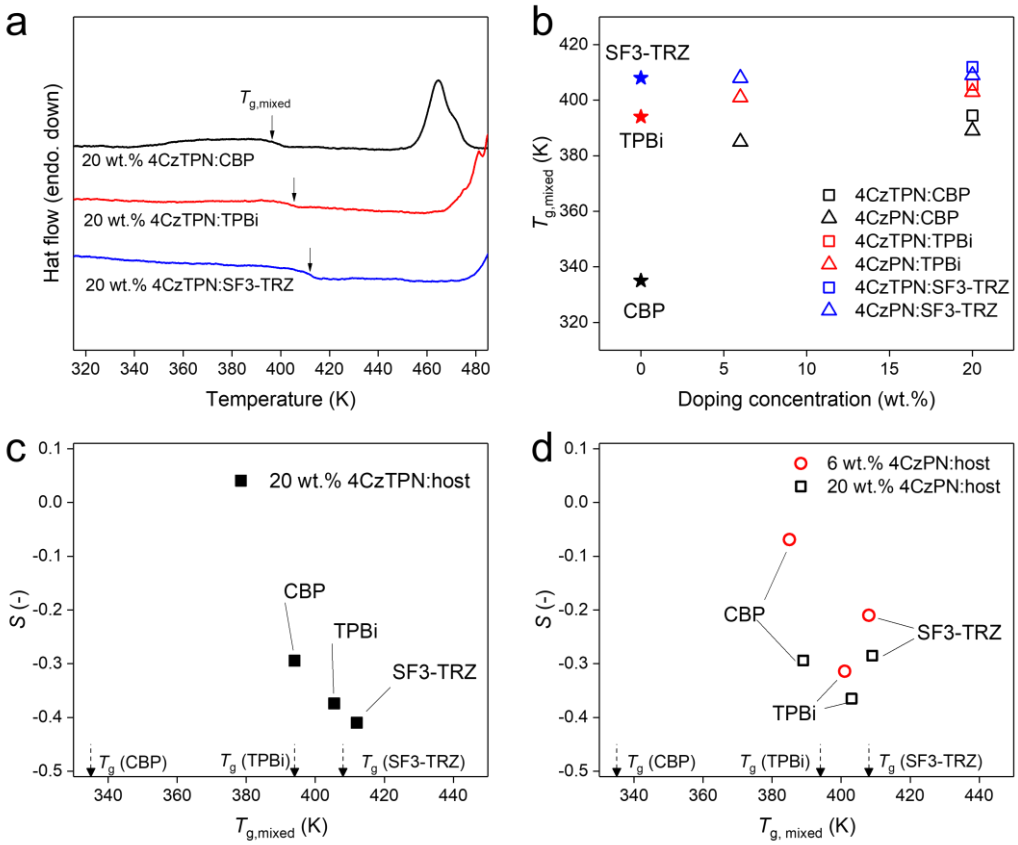

Figure 4-13. (a) DSC profiles of each mixed compound. The measurements were performed using a Netsch DSC204 Phoenix calorimeter with a scanning rate of 10°C min^{-1} under a N_2 atmosphere. (b) Concentration dependence of $T_{g,mixed}$ values. (c) Relationship between $T_{g,mixed}$ and S values of 4CzTPN in various hosts. (d) Relationship between $T_{g,mixed}$ and S values of 4CzPN in various hosts.

4-4-2. Orientation of PDM in nonpolar host

The σ_S values of the emitter:CBP films showed a clear dependence on p_G, as shown in **Figure 4-9c**. As noted above, because of the suppression of anti-parallel dipole-pair formation in the host-guest film, the host-guest film SOP should be more significant than that in undoped films. To discuss the degree of SOP, I defined the averaged PDM per molecule and the ratio of σ_S to p_{HG} in host-guest systems, *i.e.*, p_{HG}, and σ_S^* as follows:

$$p_{HG} = p_H \times \frac{c_H}{100} + p_G \times \frac{c_G}{100}$$

$$\sigma_S^* = \frac{\sigma_S}{p_{HG}}$$

where c_H and c_G are the molar ratios of the codeposited systems of host and guest molecules, respectively. For undoped films, c_H and c_G are simply 100 and 0, respectively. **Figure 4-14a** shows the relationship between p_G and σ_S*. The plots of 4CzTPN, 4CzTPN-Ph and 2CzPN are excluded because these molecules show almost no polarization. The σ_S* values of the doped films are higher than those of the undoped films, indicating the major contribution of polar emitters to the SOP due to the suppression of anti-parallel dipole-pair formation.

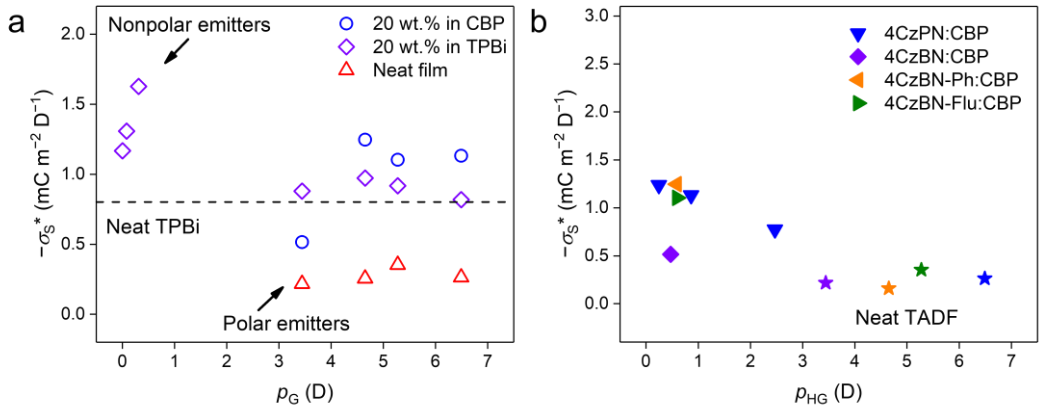

Figure 4-14. (a) Guest PDM (p_G) dependence of calculated σ_S^* values of emitter-doped films in CBP and TPBi hosts and undoped films. (b) Averaged PDM (p_{HG}) dependence of σ_S^* values of films based on emitter:CBP systems.

The σ_S* values are plotted versus p_{HG} as shown in **Figure 4-14b**. The plots in **Figure 4-14b** other than 4CzBN clearly showed nearly linear relationship, indicating that smaller dipole moments in doped systems are preferred to increase the degree of SOP. Because 4CzBN in the CBP host showed a random TDM orientation, the PDM orientation of 4CzBN would be also random in a CBP host. σ_S* then became smaller than the value estimated using p_{HG} because of the small numbers of parallel pairs of dipoles available to increase σ_S.

Note here that no clear relationship was observed between σ_S^* and S for the emitters in a CBP host (**Figure 4-15**), suggesting that the manner of the parallel and anti-parallel dipole-pairs is the dominant factor for surface charge formation, rather than the direction of the PDM vector.

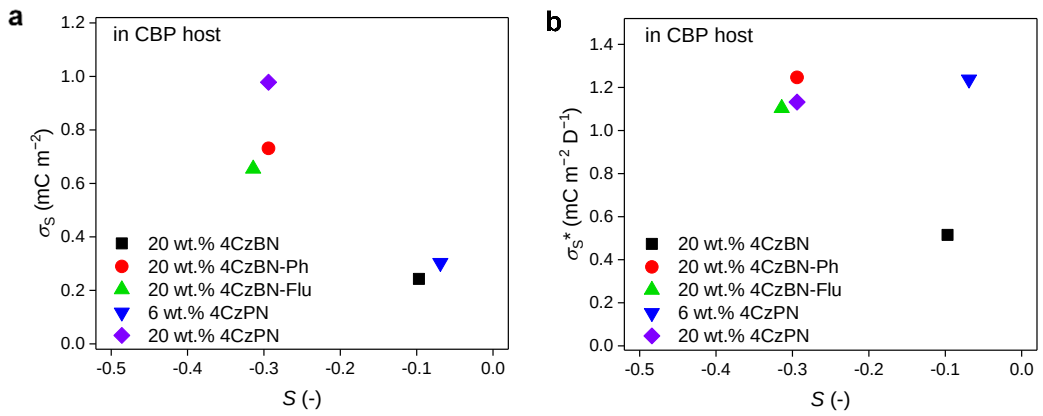

Figure 4-15. Relationships between (a) S and σ_S, and (b) S and σ_S^* for various emitter:host systems.

4-4-3. Orientation of PDM in polar host

The σ_S* characteristics of the emitter:TPBi films are shown in **Figure 4-14a**. The dotted line indicates the σ_S* of an undoped TPBi film. Doping of nonpolar molecules (p_G < 1 D) such as 4CzTPN, 4CzTPN-Ph and 2CzTPN results in an increase in σ_S* when compared with that of undoped TPBi. This can be explained using the discussion of the combination of nonpolar and polar molecules mentioned earlier[15]. Doping of polar molecules showed similar σ_S* values to that of undoped TPBi, despite the non-negligible p_G values. Furthermore, the σ_S concentration dependence (**Figure 4-16a**) showed relatively large and small variations in σ_S with the doping concentrations of 4CzTPN and 4CzPN, respectively, in the TPBi host. These results suggest that the polarizations of both TPBi and 4CzPN contribute to surface charge formation and then the concentration dependence of σ_S became weak.

Additionally, the σ_S* values of TPBi films with polar emitters such as 4CzBN-Flu and 4CzPN (**Figure 4-14a**) were smaller than the sum of (σ_S^*(TPBi neat) + σ_S^*(TADF neat)). Therefore, during codeposition, intermolecular dipole-dipole interaction promotes formation of anti-parallel dipole-pairs between host-host, guest-guest and host-guest molecules because of the high p_G. The σ_S values of the combination of polar host and guest molecules then showed limited values. Therefore, the dipole-dipole interactions between the polar guest and host contribute the molecular ordering during deposition (**Figure 4-16c**). **Figure 4-16b** shows the relationships between p_{HG} and σ_S* for the emitter:TPBi films. Similar to the results for the CBP matrix, the small p_{HG} values in the doped films increased the degree of SOP because weak dipole-dipole interactions allow parallel-pairs of PDMs to form and contribute to the surface charge formation.

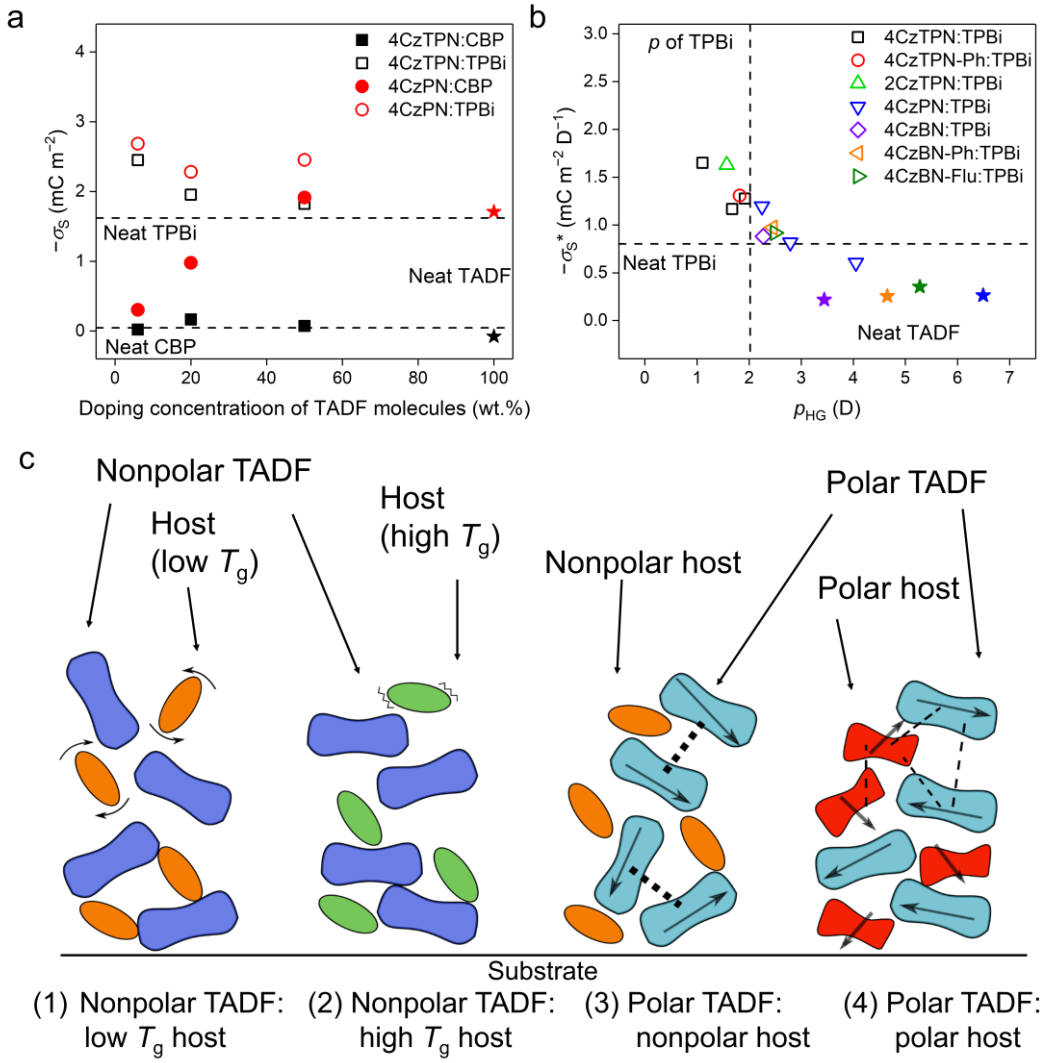

Figure 4-16. (a) Concentration dependence of σ_S values of films based on emitter:host systems. (b) p_{HG} dependence of σ_S^* values of films based on emitter:TPBi systems. (c) Schematics of film formation processes for emitter:host systems including (1) nonpolar emitter:low-T_g host, (2) nonpolar emitter:high-T_g host, (3) polar emitter:nonpolar host, and (4) polar emitter:polar host. Dotted and broken lines indicate emitter-emitter dipole interactions for (3), and emitter-emitter, host-host and emitter-host dipole interactions for (4), respectively. Black arrows indicate PDMs of emitter and host molecules.

4-5. Summary

In this study, I analyzed the molecular orientations of disk-shaped emitters exhibiting TADF *via* a coupling of optical and electrical methods. I found that the T_g and the polarization of host molecules are the key factors for increased horizontal molecular order. Furthermore, while previous computational studies reported that the short-range interaction is the dominant factor for orientation of the phosphorescent emitters, my experimental results showed that the dipole-dipole interactions also affect the PDM and TDM orientations in codeposited films. Although detailed computational studies are required for disk-shaped emitters exhibiting TADF, my experimental results showed the considerable potential of disk-shaped emitters to provide ultimate OLED characteristics, including high exciton-utilization efficiency, high light-outcoupling efficiency and high device stability.

4-6. Appendix C: Molecular conformation

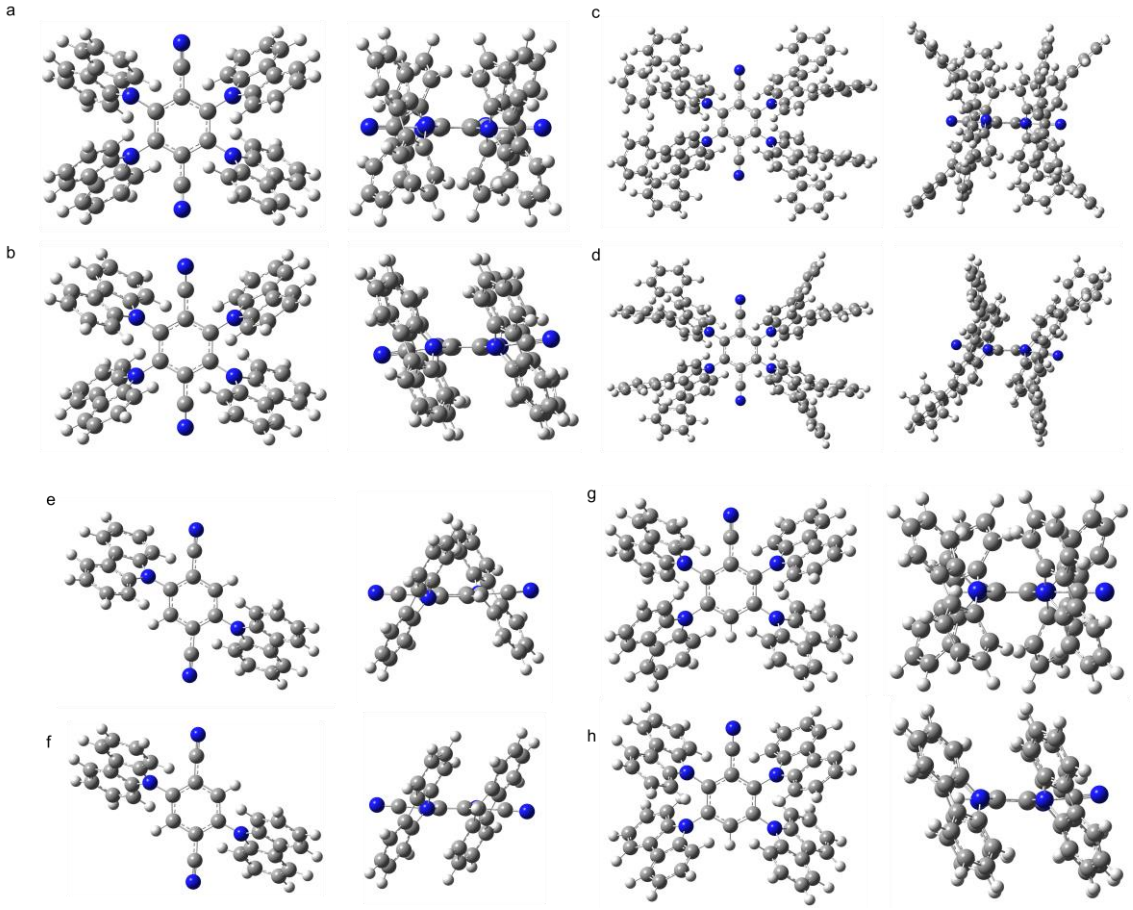

Figure C-1. Molecular structures of conformers. (a) 4CzTPN-(1), (b) 4CzTPN-(2), (c) 4CzTPN-Ph-(1), (d) 4CzTPN-Ph-(2), (e) 2CzTPN-(1), (f) 2CzTPN-(2), (g) 4CzBN-(1) and (h) 4CzBN-(2).

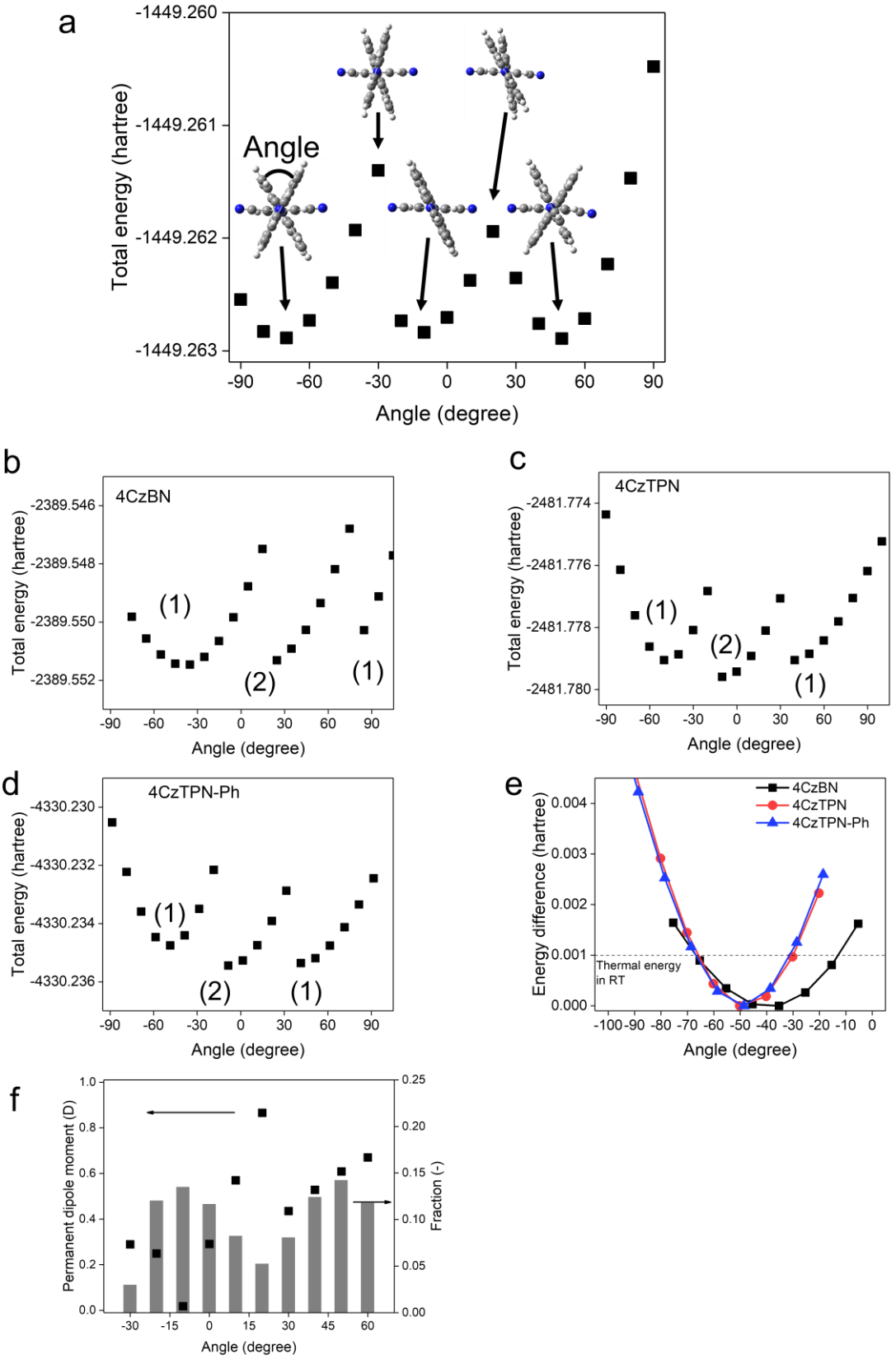
a
Angle
Total energy (hartree)
Angle (degree)
b
4CzBN
(1)
(2)
(1)
Total energy (hartree)
Angle (degree)
c
4CzTPN
(1)
(2)
(1)
Total energy (hartree)
Angle (degree)
d
4CzTPN-Ph
(1)
(2)
(1)
Total energy (hartree)
Angle (degree)
e
4CzBN
4CzTPN
4CzTPN-Ph
Thermal energy in RT
Energy difference (hartree)
Angle (degree)
f
Permanent dipole moment (D)
Fraction (-)
Angle (degree)

Figure C-2. (a) Relationship between total energies of 2CzTPN molecule and dihedral angles of two carbazole units (2,5-substituted). At −70° and 50°, the molecule showed the (1)-structure (**Figure C-1**) with the same total energy in each case. At −10°, the molecule showed the (2)-structure. Because the activation energy for the transformation, *i.e.*, the difference between the local maximum (at 20°) and minimum (at −10° and 50°) energies, of ~0.001 hartree (0.027 eV) is comparable to the thermal energy at room temperature (RT), transitions between the (1)- and (2)-structures are possible even at RT. Relationships between the total energies of the molecules and the dihedral angles of two carbazole units (2,5-substituted) for (b) 4CzBN, (c) 4CzTPN and (d) 4CzTPN-Ph. These profiles showed the local energy minima, *i.e.*, for the (1)- and (2)-structures. For these molecules, the activation energies for the transformation are greater than the thermal energy at RT. (e) Energy differences relative to the local minimum around −40° for the (1)-structures of 4CzBN, 4CzTPN and 4CzTPN-Ph. The broader energy profile for 4CzBN when compared with those of 4CzTPN and 4CzTPN-Ph suggests that large fluctuations in the carbazole units are possible for 4CzBN. (f) Dihedral angle dependence of PDM and existence fraction of 2CzTPN conformers under the assumption that −30° to −60° represents a typical cycle.

When there are several (n) conformationally different structures with a total molecule energy of E_n, I can calculate the existence ratio, R_n, *i.e.*, the fraction of each structure under the assumption of a Boltzmann distribution, which is given by

$$R_n = \frac{exp\left(-\frac{E_n - E_L}{k_B T}\right)}{\sum exp\left(-\frac{E_n - E_L}{k_B T}\right)}$$

where E_L, k_B and T are the lowest energy, the Boltzmann constant and the system temperature (T = 300 K in this calculation). Furthermore, when each conformer has permanent dipole moments (p_n), an averaged dipole moment (p_{AVG}) in the system can be calculated using the following equation:

$$p_{AVG} = \sum (R_n \times p_n)$$

In the 2CzTPN case, because of the small activation energies required for the transformation, the calculation of p_{AVG} introduced above was performed. For simplicity, I used the angular dependence of the total energy from −30° to −60° (**Figure C-2a**) to represent a typical cycle. **Figure C-2f** shows the angular dependences of the PDMs and the calculated fractions. Based on **Figure C-2f**, I calculated p_{AVG} to be 0.4 D for 2CzTPN.

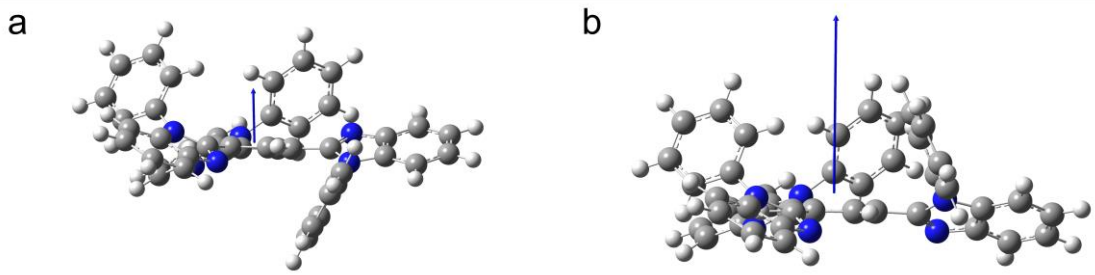

Figure C-3. Molecular structures of conformers of TPBi. (a) Structure-(1) with a permanent dipole moment of 2.0 D. (b) Structure-(2) with a permanent dipole moment of 6.0 D.

References

1. D. Yokoyama, A. Sakaguchi, M. Suzuki & C. Adachi, Horizontal orientation of linear-shaped organic molecules having bulky substituents in neat and doped vacuum-deposited amorphous films. *Org. Electron.* **10**, 127–137 (2009).
2. D. Yokoyama, Y. Setoguchi, A. Sakaguchi, M. Suzuki & C. Adachi, Orientation control of linear-shaped molecules in vacuum-deposited organic amorphous films and its effect on carrier mobilities. *Adv. Funct. Mater.* **20**, 386–391 (2010).
3. T. Komino, Y. Sagara, H. Tanaka, Y. Oki, N. Nakamura, H. Fujimoto & C. Adachi, Electroluminescence from completely horizontally oriented dye molecules. *Appl. Phys. Lett.* **108**, 241106 (2016).
4. J. Frischeisen, D. Yokoyama, C. Adachi & W. Brütting, Determination of molecular dipole orientation in doped fluorescent organic thin films by photoluminescence measurements. *Appl. Phys. Lett.* **96**, 073302 (2010).
5. C. Mayr & W. Brütting, Control of molecular dye orientation in organic luminescent films by the glass transition temperature of the host material. *Chem. Mater.* **27**, 2759–2762 (2015).
6. P. Friederich, R. Coehoorn & W. Wenzel, Molecular Origin of the Anisotropic Dye Orientation in Emissive Layers of Organic Light Emitting Diodes. *Chem. Mater.* **29**, 9528–9535 (2017).
7. T. Komino, H. Tanaka & C. Adachi, Selectively Controlled Orientational Order in Linear- Shaped Thermally Activated Delayed Fluorescent Dopants Selectively Controlled Orientational Order in Linear-Shaped Thermally Activated Delayed Fluorescent Dopants. *Chem. Mater.* **26**, 3665–3671 (2014).
8. A. Graf, P. Liehm, C. Murawski, S. Hofmann, K. Leo & M. C. Gather, Correlating

the transition dipole moment orientation of phosphorescent emitter molecules in OLEDs with basic material properties. *J. Mater. Chem. C*. **2**, 10298–10304 (2014).

9. S. S. Dalal, D. M. Walters, I. Lyubimov, J. J. de Pablo & M. D. Ediger, Tunable molecular orientation and elevated thermal stability of vapor-deposited organic semiconductors. *Proc. Natl. Acad. Sci.* **112**, 4227–4232 (2015).
10. C. S. Oh, C. K. Moon, J. M. Choi, J. S. Huh, J. J. Kim & J. Y. Lee, Relationship between molecular structure and dipole orientation of thermally activated delayed fluorescent emitters. *Org. Electron.* **42**, 337–342 (2017).
11. J. Jiang, D. M. Walters, D. Zhou & M. D. Ediger, Substrate temperature controls molecular orientation in two-component vapor-deposited glasses. *Soft Matter*. **12**, 3265–3270 (2016).
12. M. J. Jurow, C. Mayr, T. D. Schmidt, T. Lampe, P. I. Djurovich, W. Brütting & M. E. Thompson, Understanding and predicting the orientation of heteroleptic phosphors in organic light-emitting materials. *Nat. Mater.* **15**, 85–91 (2016).
13. E. Ito, Y. Washizu, N. Hayashi, H. Ishii, N. Matsuie, K. Tsuboi, Y. Ouchi, Y. Harima, K. Yamashita & K. Seki, Spontaneous buildup of giant surface potential by vacuum deposition of Alq_3 and its removal by visible light irradiation. *J. Appl. Phys.* **92**, 7306 (2002).
14. Y. Noguchi, W. Brütting & H. Ishii, Spontaneous orientation polarization in organic light-emitting diodes. *Jpn. J. Appl. Phys.* **58**, SF0801 (2019).
15. L. Jäger, T. D. Schmidt & W. Brütting, Manipulation and control of the interfacial polarization in organic light-emitting diodes by dipolar doping. *AIP Adv.* **6**, 095220 (2016).
16. Y. Noguchi, Y. Miyazaki, Y. Tanaka, N. Sato, Y. Nakayama, T. D. Schmidt, W.

Brütting & H. Ishii, Charge accumulation at organic semiconductor interfaces due to a permanent dipole moment and its orientational order in bilayer devices. *J. Appl. Phys.* **111**, 114508 (2012).

17. T. Morgenstern, M. Schmid, A. Hofmann, M. Bierling, L. Jäger & W. Brütting, Correlating Optical and Electrical Dipole Moments to Pinpoint Phosphorescent Dye Alignment in Organic Light-Emitting Diodes. *ACS Appl. Mater. Interfaces*. **10**, 31541–31551 (2018).
18. P. Friederich, V. Rodin, F. Von Wrochem & W. Wenzel, Built-In Potentials Induced by Molecular Order in Amorphous Organic Thin Films. *ACS Appl. Mater. Interfaces*. **10**, 1881–1887 (2018).
19. K. Osada, K. Goushi, H. Kaji, C. Adachi, H. Ishii & Y. Noguchi, Observation of spontaneous orientation polarization in evaporated films of organic light-emitting diode materials. *Org. Electron.* **58**, 313–317 (2018).
20. Y. Hasegawa, Y. Yamada, M. Sasaki, T. Hosokai, H. Nakanotani & C. Adachi, Well-Ordered 4CzIPN ((4s,6s)-2,4,5,6-Tetra(9-H-carbazol-9-yl)isophthalonitrile) Layers: Molecular Orientation, Electronic Structure, and Angular Distribution of Photoluminescence. *J. Phys. Chem. Lett.* **9**, 863–867 (2018).
21. H. Noda, H. Nakanotani & C. Adachi, Excited state engineering for efficient reverse intersystem crossing. *Sci. Adv.* **4**, eaao6910 (2018).
22. L. S. Cui, S. Bin Ruan, F. Bencheikh, R. Nagata, L. Zhang, K. Inada, H. Nakanotani, L. S. Liao & C. Adachi, Long-lived efficient delayed fluorescence organic light-emitting diodes using n-type hosts. *Nat. Commun.* **8**, 2250 (2017).

Chapter 5

Summary of this thesis

Summary of this thesis

In this thesis, OLED device architectures and materials were investigated to reveal the origins of device degradation with the improvement of device stabilities.

In **Chapter 2**, device degradation processes in TADF-OLEDs based on 5CzBN and 3Cz2DPhCzBN having similar molecular structures but significantly different triplet exciton lifetimes were carefully considered. The device based on 3Cz2DPhCzBN with a shorter triplet lifetime than that of 5CzBN showed a significantly long device lifetime under constant current operation. Simple observations of the difference spectra, ΔI_{EL}, in the degradation processes suggested the shift of the carrier recombination site toward the HBL-side and hole-injection into the HBL under continuous operation. The 3Cz2DPhCzBN-based OLED showed the smaller spectral changes than those of the 5CzBN-based OLED. Furthermore, carrier-transport stabilities of the EMLs were investigated by HODs and EODs studies. I revealed that the coupled operational stress of electron current and the excitation of the TADF molecules, *i.e.*, triplet exciton-polaron interaction (TPI) is one of dominant channels of the degradation of TADF-OLEDs. Because of its short triplet lifetime, 3Cz2DPhCzBN resulted in low triplet-exciton density and a suppressed rate of TPI in the device. Therefore, the improvement of the RISC characteristics of TADF molecules and the control of carrier transport properties of EML aimed for the suppression of TPI are significantly needed for improvement of a device lifetime.

In **Chapter 3**, exciton dynamics in TADF-OLEDs under operation were investigated by MFEs in the devices. Magnetic responses of OLED characteristics could be expected to use as a method to prove the manner of exciton annihilation processes such as TPI as suggested in **Chapter 2**, because separation of degenerate triplet states by a

magnetic field should affect the device performance and reflect the exciton dynamics in devices. Thus I compared MEL profiles of TADF-OLEDs based on various emitters and revealed that the profiles contain two origins of MFEs such as PP and TPI models. Further, the MEL amplitudes based on TPI model significantly depended on emitters' exciton lifetime that clearly suggests that emitters with long exciton lifetimes suffer from more significant annihilation induced by TPI than the emitters with short exciton lifetimes. Furthermore, for an analysis of degraded OLEDs, I identified the exciplex-formation on a film interface as one of the origins of a change in MEL profiles because the device aging affects carrier transport properties in an EML. Therefore, as same as the conclusion in **Chapter 2**, exciton lifetimes of TADF molecules and a control of carrier transport properties are important for improvement of device stability. Furthermore, because of the generation of interfacial excited state such as an exciplex, I clarified that the stability of the interface should be also improved.

In **Chapter 4**, a molecular orientations in organic host:guest films based on disk-shaped TADF molecules were investigated. Because the orientation is one of limiting factors of EQE of OLEDs, the investigations of an emitter molecule and a combination with a host molecule are needed for improvement of an emission efficiency and a decrease of driving current. I revealed that a T_g and the polarization of a host molecule are ones of key factors to control the emitter's molecular orientation. For the nonpolar TADF molecules, a high-T_g host molecule can easily fix a molecular motion of the emitter molecule, and achieve the highly horizontal emitter's TDM orientation. For polar emitter molecules, the polarization of a host molecule disturbs intermolecular dipole-dipole interactions between emitter molecules by a formation of the interaction between host and emitter molecules. Further, I demonstrated perfectly horizontal TDM orientation and

light-outcoupling efficiency of around 30% of an OLED based on a 4CzTPN-Ph:host film. These results provide a possibility to achieve an ultimate OLED performance with a combination of 100% of internal quantum efficiency, extremely high light-outcoupling efficiency and high device stability of the OLEDs based on disk-shaped TADF emitters. For the ultimate performance, further development of emitter and host molecules and film-fabrication process will be needed to exploit the abilities in emitters and OLEDs.

I hope that my results will be useful to realize ultimately stable TADF-OLED in near future.

Future perspective

For TADF-OLEDs, an unstable triplet exciton generated by electrical excitation is one of the origins for degradation of the devices. An efficient RISC (high rate constant of RISC, k_{RISC}) process can decrease a density of accumulated triplet excitons in operating devices. To enhance RISC properties of the emitters, a fine molecular tuning is performed and clear advances have been reported[1–4]. As introduced in **Chapter 2**, Noda et al. reported that the insertion of second type electron-donor (D_2) moieties having a suitable locally excited triplet state (^{3}LE) to the donor-acceptor (D-A) TADF molecular systems based on carbazole-benzonitrile (CzBN) efficiently improved the k_{RISC} because of the reduced activation energy for the RISC process due to tuned energy difference between ^{3}LE of D_2 and the triplet charge-transfer (^{3}CT) state of the D-A system[5]. According to this RISC improvement mechanism, the strategy to insert multiple-donor moieties, *i.e.*, several (n) types of donor (D_n), into TADF molecules can be expected to efficiently enhance k_{RISC}. For BN-based structures, the maximum of n value is five, *i.e.*, five different donor moieties having tuned ^{3}LE levels, can be substituted to the BN group to reduce activation energy for RISC. With considering the triplet levels of these moieties, for example, fluorene, dibenzofuran, and dibenzothiophene are promising candidates for the electron-donor moieties with a suitable triplet energy (**Figure 5-1**). As Noda et al. reported[5], the substitution of phenyl or methyl groups to donor moieties can change their triplet energies, that makes fine tuning of the ^{3}LE level possible. Design of a multiple-donor TADF molecule with high k_{RISC} can be expected to improve the device characteristics such as efficiency rolloff and device stability because of suppressed unwanted triplet interactions under device operation.

Further, the high radiative decay rate constant from S_1 (k_r^S) also essentially reduces

the exciton density in EMLs, however, the k_r^S of a TADF molecule is basically limited because of the tradeoff relationship between the small ΔE_{ST} and the high k_r^S of TADF molecules. A TADF-assisted-fluorescence (TAF) system-based EML[6,7] comprising host, TADF, and fluorescent molecules can reduce the exciton density in the EML through the FRET energy transfer from S_1 of TADF molecules to S_1 of fluorescent molecules having high k_r^S. Therefore, the TAF-OLEDs based on the combination of TADF molecules having high k_{RISC} and fluorescent molecules having high k_r^S that show efficient FRET energy transfer is a promising proper system for high OLED stability (**Figure 5-4**).

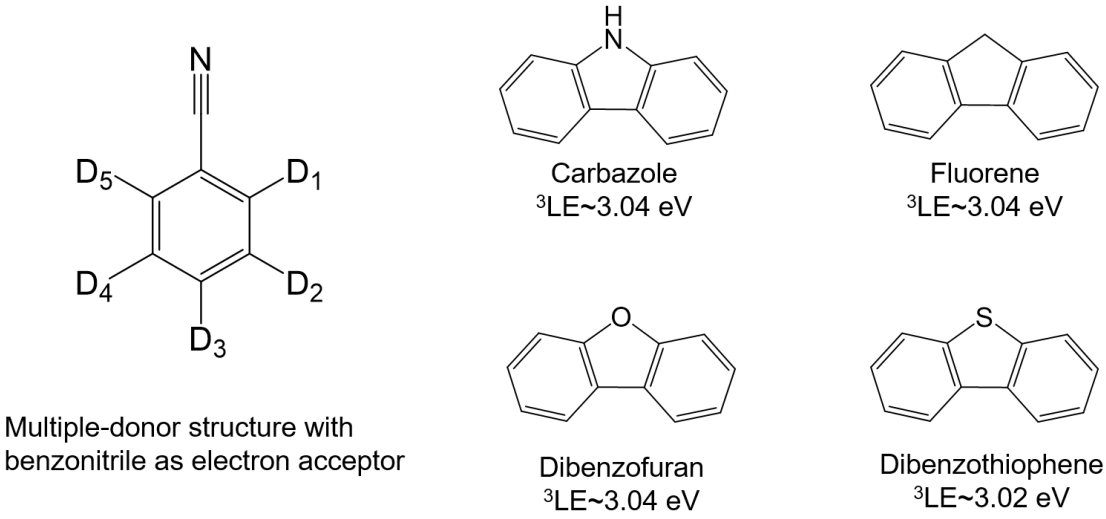

Figure 5-3. The molecular structure of a multiple-donor TADF molecule based on benzonitrile as an electron acceptor. D_ns (n = 1-5) are donor moieties having suitable ^{3}LE levels to reduce the activation energy for the RISC process. The candidates for D_n are fluorene, dibenzofuran, and dibenzothiophene having ^{3}LE levels around 3 eV[8].

In addition to the importance of EMLs' stability, HBLs and EBLs can also contribute the triplet-exciton management in the EML. For example, an insertion of a thin Liq layer into the interface between an EML and an HBL dramatically increased the device lifetime[9]. The lifetime improvement was ascribed the triplet quenching, adhesion effect and a removal of water molecules. For any reasons, their results clearly suggest that

an interface engineering between EML and other layers significantly affects the device lifetime because of high exciton density at the layer interfaces. Generally, a recombination site position in an EML of TADF-OLEDs generally locate near film interface between an EML and an HBL in case of TADF-OLEDs because an electron-transport is controlled by the confined LUMO level of the TADF molecule inside the LUMO level of the host molecule[10]. In case of a single-host EML, carrier balance is not completed, then major charge carriers (electrons or holes) in the EML might invade the adjacent layers, *i.e.*, EBL or HBL, and degrade the charge transport and injection characteristics (**Figure 5-2a** and **b**). Therefore, I suggested mainly two approaches for further improvement of device lifetimes, *i.e.*, a tuning of carrier transport properties of an EML and interface engineering in OLEDs.

For state-of-the-art phosphorescence-based OLEDs, an exciplex co-host technique has been used for highly efficient and stable OLEDs[11,12] as shown in **Figure 5-2c**. Co-host structures form a highly efficient exciplex state and well-balanced carrier transport properties to improve efficiency rolloff and stability issues. Although there are a few reports to apply co-host technique and they mentioned that the efficiency rolloff and stability issues were successfully improved even in TADF-OLEDs[13,14], the improvement of device lifetime was still primitive. One of limiting factors of the improvement might be a stability of n-type host molecule because of difficulty of a compatibility of high electron mobility, stability of excited and cation states, high T_1 energy for energy confinement and high T_g[15]. Especially, for using as a host molecule, the stability of excited and cation states of a molecule is highly demanded because not only an anion state but also the excited and cation states of the host molecule are generated in the EML. Although SF3-TRZ used as the HBL molecule in this study was supposed as n-type host suggested

by Cui *et al*.[16], I observed the red electromer emission from the SF3-TRZ layer[17], indicating that imperfect hole-blocking function and successive device degradation channel. Therefore, the preparation of stable n-type host molecules for blue TADF molecules is one of critical issues to improve the device stability. Further, the carrier injection and transport properties of all the layers and interfaces in OLEDs should be considered. For good carrier transport and injection, a high carrier mobility and a small HOMO or LUMO energy difference between organic layers (ΔE_{HOMO} and ΔE_{LUMO}) are needed. Regarding carrier injection performance, smaller ΔE_{HOMO} and ΔE_{LUMO} than 0.2 eV are favorable for good carrier injection without carrier accumulation because the localized density of states (DOS) distributions with the width of ~0.2 eV in general organic layers should be largely overlapped in each interface between layers[18,19].

At the interface between an EML and an HBL where the electrically-generated excitons are highly localized, some unwanted chemical reactions would generate decomposed materials and degrade device performance. Fujimoto *et al*. clarified that a short device fabrication time provides a significant improvement of device lifetime[20], indicating that the adsorption of some materials during the deposition process affect the device stability. It was concluded that the materials, *i.e.*, chamber impurities such as previously-deposited materials and plasticizers in the deposition chamber, adsorbed on the layer interfaces promote the chemical reactions and the device degradation. Furthermore, in **Chapter 3**, I observed the presence of interfacial excited states in degraded devices. It is speculated that these excited states would interact with the chamber impurities, and result in inferior device performance. Therefore, for high device stability, not only the control of exciton distribution in the EML, but also the decrease of chemical reactants during the device fabrication to suppress unwanted chemical reactions

is a critical issue. In particular, the preparation of clean chamber condition and the minimization of the exposure time of film interfaces during the fabrication should be required for the improvement of device lifetimes.

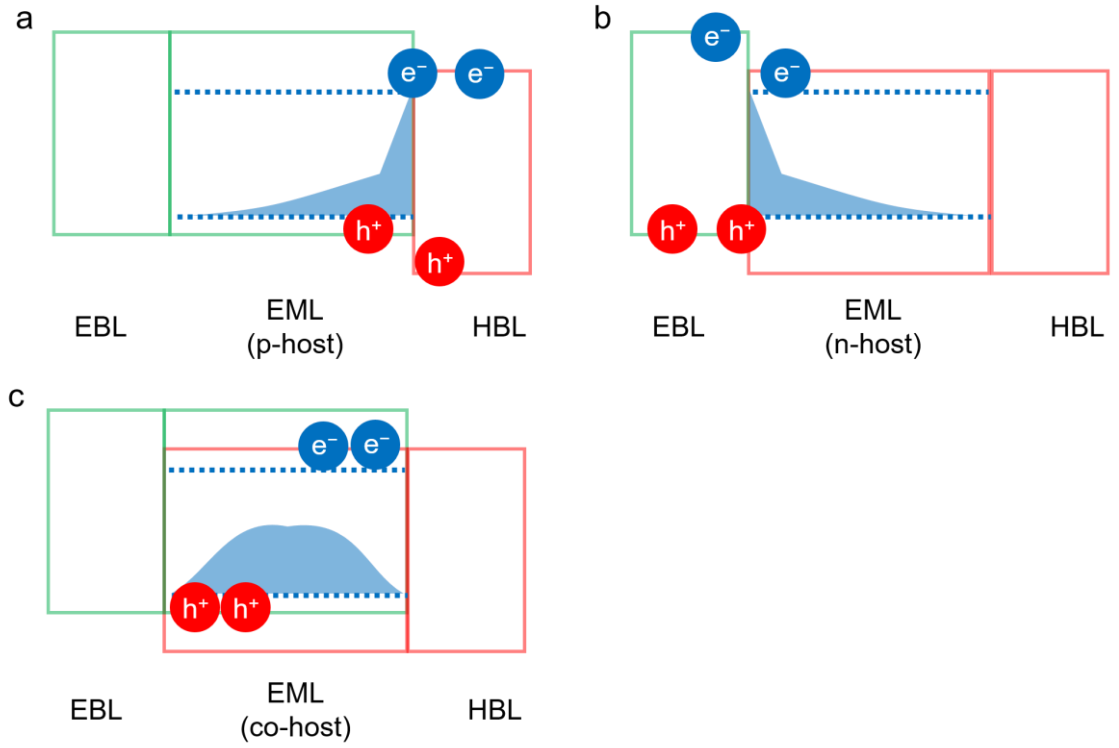

Figure 5-2. Schematics of (a) p-host EML, (b) n-host EML, and (c) co-host EML systems. Green, red blue lines show HOMO and LUMO levels of EBL (p-host), HBL (n-host) and doped emitter molecules, respectively. Each EML system can be expected to show a highly-localized and a broad exciton distributions in the EMLs, respectively.

In **Chapter 3**, I discussed the exciton energy loss at the layer interface between a EML and a HBL through unexpected exciplex generation due to dramatically degraded carrier transport properties of the EML. Because the interlayer exciplex based on mCBP and SF3-TRZ is unfortunately not emissive (PLQY~4%), there are large energy loss via triplet CT and LE states of mCBP and SF3-TRZ, that cannot contribute the EL from TADF molecules because of the low energy transfer efficiency. Therefore, the design of a highly

efficient exciplex based co-host system[12] is also needed to reduce exciton loss through intermediate excited states.

In **Chapter 4**, I mentioned that the T_g values of host molecule and mixed system of host and emitter molecules are the key issues to control an emitter's orientation. Recently, a relationship between a T_g, a film density and device characteristics has been studied and a remarkable improvement of device characteristics such as device lifetime was reported[21,22]. A film density can be well controlled by a substrate temperature during a deposition, T_{sub}, and a rate of T_{sub}/T_g. A molecule shows highly horizontal orientation in small T_{sub}/T_g condition whereas a film density shows the maximum value in 0.75-0.85 of T_{sub}/T_g. Furthermore, phosphorescent OLEDs based on the EML deposited under a controlled T_{sub} corresponding to $0.85T_g$ of a host molecule such as TPBi showed an improvement of device lifetimes[21]. The authors mentioned that a suppressed nonradiative decay of the triplet exciton of a phosphorescent emitter in the highly dense TPBi film resulted in the improvement of device stability. Although the control of a T_{sub} during the deposition of organic layers is not common in the industry field, the control would effectively improve a device lifetime due to high density of the films. Furthermore, for the application to an automotive high thermal stability of the device has been demonstrated by using organic molecules having high T_g above 130°C[23]. When the high-T_g molecules are used in the devices, T_{sub} should be controlled above the room temperature for the formation of the highly dense films (**Figure 5-3**). Therefore, the clarification of detailed physics of film formation processes and the development of the T_{sub}-control system for manufacturing processes are important issues to improve the device performance.

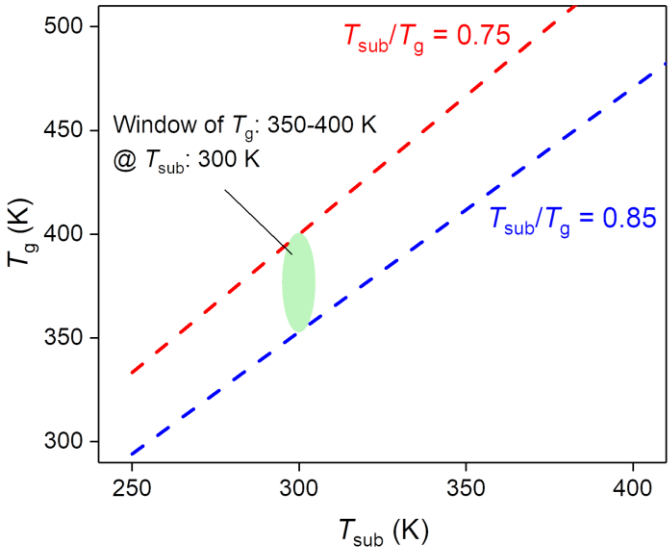

Figure 5-3. Relationships between a T_{sub} and T_g to get the highest density of a deposited film. Blue and red lines show the relationship for $T_{sub}/T_g = 0.85$[21] and 0.75[22], respectively.

I demonstrated the perfect horizontal orientation of an emitter in a doped film and a light-outcoupling efficiency of around 30% in **Chapter 4**. For CzBN-based disk-shaped emitter molecules, the suppression of rotation and fluctuation of Cz units in the molecules is essentially needed to obtain horizontal TDM orientation. For example, the substitution of bulky moieties such as spirobifluorene[15] and adamantane[24] to the BN unit (**Figure 5-1**) can be expected to result in a rigid molecular structure and higher T_g of the emitter molecule, that are favorable for the emitter's horizontal orientation. However, a stability of the orientation in the device under operation is still unknown. If the horizontal orientations (η_{OC} = 30%) of an emitter in the device randomize under device operation (η_{OC} = 20%), a luminance decrease to ~67% of the initial luminance, meaning that the randomization should be one of the degradation mechanisms. Therefore, further investigation of orientation stability is needed for ultimate efficient and stable OLEDs, because the aggregation of molecules in the devices is sometimes one of the reasons to

degrade the device performance[25].

In summary, for the improvement of TADF-OLEDs' stability, the enhancement of k_{RISC} of rigid TADF molecules, the preparation of stable bipolar host (co-host) molecules with high T_gs exhibiting high PLQY and efficient RISC process, interface engineering to reduce energy loss and improve carrier injection, the application of a TAF system with highly emissive fluorescence molecules, and clean fabrication environment and T_{sub}-control system are needed as shown in **Figure 5-4**.

By further considerations and assembling the above technique, I strongly expect the realization of ultrahigh stability of OLEDs.

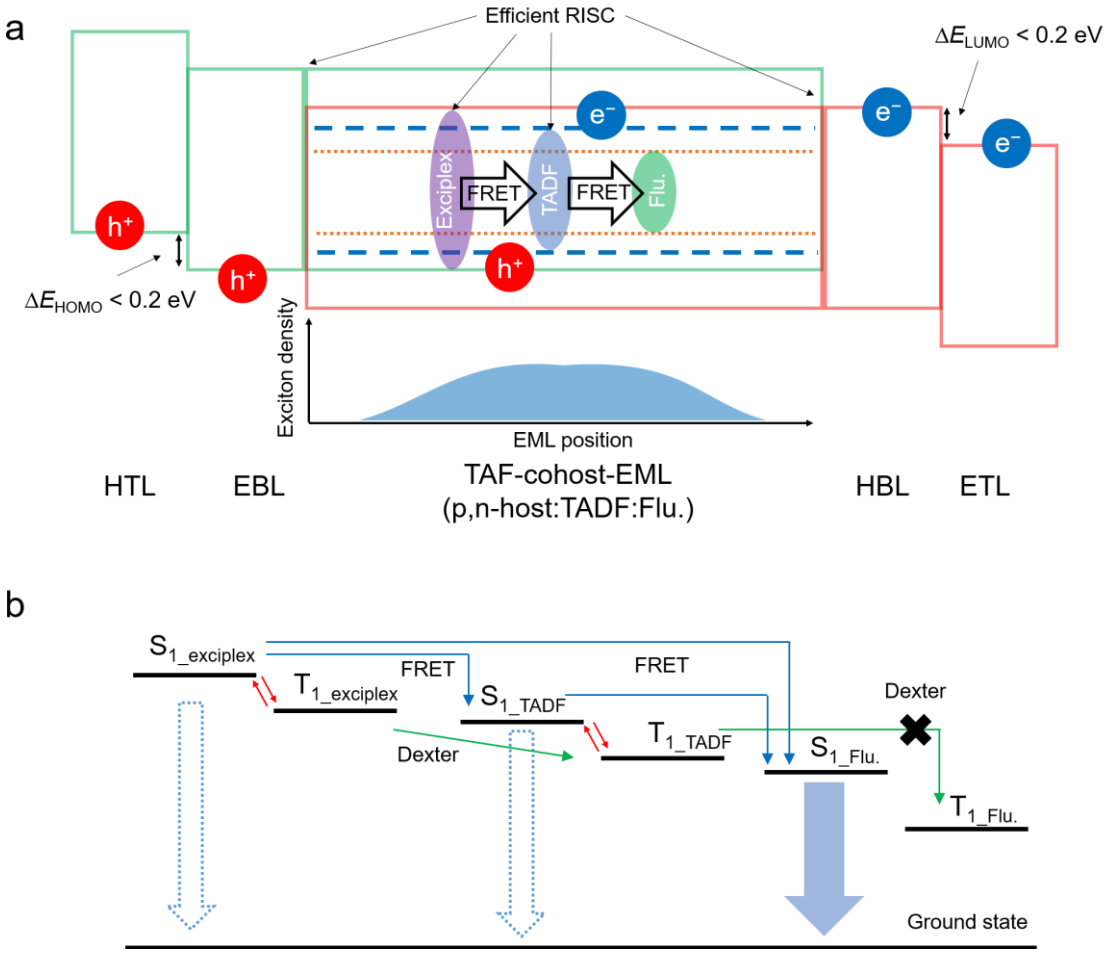

Figure 5-4. Schematics of the OLED based on the combination of a co-host and a TAF system for high device stability. (a) HOMO-LUMO energy diagrams of stacked layers such a HTL, an EBL, an EML, a HBL, and an ETL. The EML comprises host, TADF, and fluorescent (Flu.) molecules. Orange dotted lines show the HOMO and LUMO energy levels of fluorescent molecule. In the co-host system, broader exciton distribution can be expected as shown. (b) Energy transfer pathway in the TAF-cohost-EML. Carrier recombination, *i.e.*, electrical exciton generation, on exciplex host and TADF molecules is assumed.

References

1. H. Noda, H. Nakanotani & C. Adachi, Highly Efficient Thermally Activated Delayed Fluorescence with Slow Reverse Intersystem Crossing. *Chem. Lett.* **48**, 126–129 (2018).
2. C. Y. Chan, M. Tanaka, H. Nakanotani & C. Adachi, Efficient and stable sky-blue delayed fluorescence organic light-emitting diodes with CIEy below 0.4. *Nat. Commun.* **9**, 5036 (2018).
3. T. Miwa, S. Kubo, K. Shizu, T. Komino, C. Adachi & H. Kaji, Blue organic light-emitting diodes realizing external quantum efficiency over 25% using thermally activated delayed fluorescence emitters. *Sci. Rep.* **7**, 284 (2017).
4. H. Kaji, H. Suzuki, T. Fukushima, K. Shizu, K. Suzuki, S. Kubo, T. Komino, H. Oiwa, F. Suzuki, A. Wakamiya, Y. Murata & C. Adachi, Purely organic electroluminescent material realizing 100% conversion from electricity to light. *Nat. Commun.* **6**, 8476 (2015).
5. H. Noda, H. Nakanotani & C. Adachi, Excited state engineering for efficient reverse intersystem crossing. *Sci. Adv.* **4**, eaao6910 (2018).
6. H. Nakanotani, T. Higuchi, T. Furukawa, K. Masui, K. Morimoto, M. Numata, H. Tanaka, Y. Sagara, T. Yasuda & C. Adachi, High-efficiency organic light-emitting diodes with fluorescent emitters. *Nat. Commun.* **5**, 4016 (2014).
7. T. Furukawa, H. Nakanotani, M. Inoue & C. Adachi, Dual enhancement of electroluminescence efficiency and operational stability by rapid upconversion of triplet excitons in OLEDs. *Sci. Rep.* **5**, 8429 (2015).
8. R. C. Heckman, Phosphorescence studies of some heterocyclic and related organic compounds. *J. Mol. Spectrosc.* **2**, 27–41 (1958).

9. D. P. K. Tsang, T. Matsushima & C. Adachi, Operational stability enhancement in organic light-emitting diodes with ultrathin Liq interlayers. *Sci. Rep.* **6**, 22463 (2016).

10. H. Nakanotani, K. Masui, J. Nishide, T. Shibata & C. Adachi, Promising operational stability of high-efficiency organic light-emitting diodes based on thermally activated delayed fluorescence. *Sci. Rep.* **3**, 2127 (2013).

11. K. H. Kim, S. J. Yoo & J. J. Kim, Boosting Triplet Harvest by Reducing Nonradiative Transition of Exciplex toward Fluorescent Organic Light-Emitting Diodes with 100% Internal Quantum Efficiency. *Chem. Mater.* **28**, 1936–1941 (2016).

12. M. Sarma & K. T. Wong, Exciplex: An Intermolecular Charge-Transfer Approach for TADF. *ACS Appl. Mater. Interfaces*. **10**, 19279–19304 (2018).

13. C. K. Moon, K. Suzuki, K. Shizu, C. Adachi, H. Kaji & J. J. Kim, Combined Inter- and Intramolecular Charge-Transfer Processes for Highly Efficient Fluorescent Organic Light-Emitting Diodes with Reduced Triplet Exciton Quenching. *Adv. Mater.* **29**, 1606448 (2017).

14. J. M. Kim, C. H. Lee & J. J. Kim, Mobility balance in the light-emitting layer governs the polaron accumulation and operational stability of organic light-emitting diodes. *Appl. Phys. Lett.* **111**, 203301 (2017).

15. H.-F. Chen, S.-J. Yang, Z.-H. Tsai, W.-Y. Hung, T.-C. Wang & K.-T. Wong, 1,3,5-Triazine derivatives as new electron transport–type host materials for highly efficient green phosphorescent OLEDs. *J. Mater. Chem.* **19**, 8112 (2009).

16. L. S. Cui, S. Bin Ruan, F. Bencheikh, R. Nagata, L. Zhang, K. Inada, H. Nakanotani, L. S. Liao & C. Adachi, Long-lived efficient delayed fluorescence

organic light-emitting diodes using n-type hosts. *Nat. Commun.* **8**, 2250 (2017).

17. M. Tanaka, H. Noda, H. Nakanotani & C. Adachi, Effect of Carrier Balance on Device Degradation of Organic Light-Emitting Diodes Based on Thermally Activated Delayed Fluorescence Emitters. *Adv. Electron. Mater*. **5**, 1800708 (2019).
18. T. Matsushima, K. Goushi & C. Adachi, Charge-carrier injection characteristics at organic/organic heterojunction interfaces in organic light-emitting diodes. *Chem. Phys. Lett.* **435**, 327–330 (2007).
19. P. Friederich, V. Rodin, F. Von Wrochem & W. Wenzel, Built-In Potentials Induced by Molecular Order in Amorphous Organic Thin Films. *ACS Appl. Mater. Interfaces*. **10**, 1881–1887 (2018).
20. H. Fujimoto, T. Suekane, K. Imanishi, S. Yukiwaki, H. Wei, K. Nagayoshi, M. Yahiro & C. Adachi, Influence of vacuum chamber impurities on the lifetime of organic light-emitting diodes. *Sci. Rep.* **6**, 38482 (2016).
21. J. Ràfols-Ribé, P. A. Will, C. Hänisch, M. Gonzalez-Silveira, S. Lenk, J. Rodríguez-Viejo & S. Reineke, High-performance organic light-emitting diodes comprising ultrastable glass layers. *Sci. Adv.* **4**, eaar8332 (2018).
22. Y. Esaki, T. Komino, T. Matsushima & C. Adachi, Enhanced Electrical Properties and Air Stability of Amorphous Organic Thin Films by Engineering Film Density. *J. Phys. Chem. Lett.* **8**, 5891–5897 (2017).
23. F. Steuber, J. Staudigel, M. Stössel, J. Simmerer, A. Winnacker, H. Spreitzer, F. Weissörtel & J. Salbeck, White light emission from organic LEDs utilizing spiro compounds with high-temperature stability. *Adv. Mater.* **12**, 130–133 (2000).
24. Y. Wada, S. Kubo & H. Kaji, Adamantyl Substitution Strategy for Realizing

Solution-Processable Thermally Stable Deep-Blue Thermally Activated Delayed Fluorescence Materials. *Adv. Mater.* **30**, 1705641 (2018).

25. Q. Wang, B. Sun & H. Aziz, Exciton-polaron-induced aggregation of wide-bandgap materials and its implication on the electroluminescence stability of phosphorescent organic light-emitting devices. *Adv. Funct. Mater.* **24**, 2975–2985 (2014).

Abbreviation list

Keywords

Benzonitrile-carbazole (CzBN)
Density functional theory (DFT)
Differential scanning calorimetry (DSC)
Displacement current measurement (DCM)
Electroluminescence (EL)
Electron-blocking layer (EBL)
Electron-injection layer (EIL)
Electron-only device (EOD)
Electron-transporting layer (ETL)
Emission layer (EML)
External quantum efficiency (EQE)
Förster resonance energy transfer (FRET)
Giant surface potential (GSP)
High-field effect (HFE)
Hole-blocking layer (HBL)
Hole-injection layer (HIL)
Hole-only devices (HOD)
Highest occupied molecular orbital (HOMO)
Hole-transporting layer (HTL)
Internal quantum efficiency (IQE)
Intersystem crossing (ISC)
Lifetime (LT)
Lowest singlet excited state (S_1)
Lowest triplet excited state (T_1)
Lowest unoccupied molecular orbital (LUMO)
Low-field effect (LFE)
Magnetic field effect (MFE)
Organic light-emitting diodes (OLEDs)
Permanent dipole moment (PDM)
Photoluminescence (PL)
Photoluminescence quantum yield (PLQY)
Photomultiplier tube (PMT)
Polaron (P)
Polaron pair (PP)

Resistance-capacitance (RC)
Reverse intersystem crossing (RISC)
Room temperature (RT)
Singlet ground state (S_0)
Singlet-triplet annihilation (STA)
Spontaneous orientation polarization (SOP)
Thermally-activated delayed fluorescence (TADF)
Time-dependent density functional theory (TD-DFT)
Transition dipole moment (TDM)
Triplet exciton-polaron annihilation (TPA)
Triplet exciton-polaron interaction (TPI)
Triplet-triplet annihilation (TTA)
Zero-field splitting (ZFS)

Materials

10-[4-(4,6-Diphenyl-1,3,5-triazin-2-yl)phenyl]-10H-phenoxazine (ACRXTN)
Tris(8-hydroxyquinolinato)aluminium (Alq_3)
4,4-Bis[*N*-(1-naphthyl)-*N*-phenylamino]-biphenyl (α-NPD)
2,7-Bis(2,20-bipyridine-5-yl)triphenylene (BPy-TP2)
4,4'-Di(9H-carbazol-9-yl)-1,1'-biphenyl (CBP)
N,*N*-Dimethylformamide (DMF)
1,4,5,8,9,11-Hexaazatriohenyleane hexacarbonitrile (HAT-CN)
Indium-tin-oxide (ITO)
Lithium fluoride (LiF)
8-Hydroxyquinolinolato-lithium (Liq)
Tris(2-phenylpyridine)iridium(III) ($Ir(ppy)_3$)
3,3'-Di(9*H*-carbazol-9-yl)-1,1'-biphenyl (mCBP)
1,3-Bis(N-carbazolyl)benzene (mCP)
Molybdenum trioxide (MoO_3)
2-Biphenyl-4,6-bis(12-phenylin-dolo[2,3-a]carbazol-11-yl)-1,3,5-triazine (PIC-TRZ)
3-(9,9-Dimethylacridin-10(9H)-yl)-9H-xanthen-9-one (PXZ-TRZ)
2-(9,9'-Spirobi[fluoren]-3-yl)-4,6-diphenyl-1,3,5-triazine (SF3-TRZ)
4,4’-Cyclohexylidenebis[N,N-bis(4-methylphenyl)benzamine] (TAPC)
9,9'-Diphenyl-6-(9-phenyl-9H-carbazol-3-yl)-9H,9'H-3,3'-bicarbazole (Tris-Pcz)
1,3,5-Tris(1-phenyl-1H-benzo[d]imidazol-2-yl)benzene (TPBi)
2,4,6-Tris(biphenyl-3-yl)-1,3,5-triazine (T2T)

1,2-Bis(carbazol-9-yl)-4,5-dicyanobenzene (2CzPN)
1,4-Dicyano-2,5-bis(carbazol-9-yl)benzene (2CzTPN)
2,4,6-Tris(3,6-diphenylcarbazole-9-yl)-3,5-(9H-carbazole-9-yl)benzonitrile (2Cz3DPhCzBN)
9-(3-(9H-Carbazol-9-yl)-9-(4-(4,6-diphenyl-1,3,5-triazin-2-yl)phenyl)-9H-carbazol-6-yl)-9H-carbazole (3CzTRZ)
2,4,6-Tris(9H-carbaozle-9-yl)-3,5-bis(3,6-diphenylcarbazole-9-yl)benzonitrile (3Cz2DPhCzBN)
2,3,5,6-Tetrakis(carbazol-9-yl)benzonitrile (4CzBN)
2,3,5,6-Tetrakis(carbazol-9-yl)-4-(9,9-dimethylfluoren-3-yl)benzonitrile (4CzBN-Flu)
2,3,5,6-Tetrakis(carbazol-9-yl)-4-phenylbenzonitrile (4CzBN-Ph)
2,4,5,6-Tetra(9H-carbazol-9-yl)isophthalonitrile (4CzIPN)
1,2,3,4-Tetrakis(carbazol-9-yl)-5,6-dicyanobenzene (4CzPN)
1,4-Dicyano-2,3,5,6-tetrakis(carbazol-9-yl)benzene (4CzTPN)
1,4-Dicyano-2,3,5,6-tetrakis(3,6-diphenylcarbazol-9-yl)benzene (4CzTPN-Ph)
Penta(9H-carbazol-9-yl)benzonitrile (5CzBN)

Physical symbols

Accumulation voltage (V_{acc})
Active device area (A)
Actual current (J_{act})
Amplitude of HFE (A_H)
Amplitude of LFE (A_L)
Angle between the direction of dipoles and the line connecting them (β)
Apparent capacitance (C_{app})
Carrier balance (η_{CB})
Change in driving voltage (ΔV)
Change in emission efficiency under magnetic field ($\Delta\eta(B)$)
Characteristic field of LFE (B_H)
Characteristic field of HFE (B_L)
Codeposited layer capacitance ($C_{codeposited}$)
Current density (J)
DCM signal of backward scan ($C_{backward}$)
DCM signal of forward scan ($C_{forward}$)
Difference spectrum (ΔI_{EL})
Dipole interaction energy of antiparallel-pair ($U_{\uparrow\downarrow}$)

Dipole interaction energy of parallel-pair ($U_{\uparrow\uparrow}$)
Distance between two dipoles (r)
Electroluminescence intensity (I_{EL})
Emission efficiency with no magnetic field ($\eta(0)$)
Energy gap between the lowest singlet and triplet excited energy levels (ΔE_{ST})
Exciton-utilization efficiency (η_{EX})
Glass transition temperature (T_g)
Glass transition temperature of mixed system ($T_{g,mixed}$)
Initial luminance (L_0)
Initial voltage (V_0)
Injection voltage (V_{inj})
Light-outcoupling efficiency (η_{OC})
Luminance (L)
Magnetic field (B)
Magneto-conductance (MC)
Magneto-efficiency under constant current ($M\eta_J$)
Magneto-efficiency under constant voltage ($M\eta_V$)
Magneto-electroluminescence, magnetic-field-modulated EL (MEL)
Magneto-electroluminescence under constant current (MEL_J)
Magneto-electroluminescence under constant voltage (MEL_V)
Magneto-photoluminescence (MPL)
Magneto-resistance (MR)
Molar ratio of guest molecule (c_G)
Molar ratio of host molecule (c_H)
Normalized EL intensity ($I_{EL,normalized}$, $I_{EL,norm}$)
Order parameter (S)
Permanent dipole moment (p)
Permanent dipole moment of guest molecule (p_G)
Permanent dipole moment of host molecule (p_H)
Permanent dipole moment of host-guest system (p_{HG})
Photoluminescence quantum yield (η_{QY})
Rate constant of intersystem crossing of excitonic state (k_{ISC}, k_{EX})
Rate constant of intersystem crossing of polaron pair state (k_{ISCP})
Rate constant of radiative decay from singlet excited state (k_r^S)
Rate constant of reverse intersystem crossing of excitonic state (k_{RISC})
Rate constant of triplet exciton-polaron interaction (k_{TPI})

Ratio of surface charge density to permanent dipole moment of host-guest system (σ_S^*)
Relative permitivity (ε_r)
Substrate temperature during deposition (T_{sub})
Surface charge density (σ_S)
Thickness (d)
Threshold voltage (V_{th})
Voltage (V)
Work function of anode (ϕ_{Anode})
Work function of cathode ($\phi_{Cathode}$)
Zeeman splitting (ΔE_Z)
Zero-field splitting parameters (D and E)

Publication list

Original papers

1. Masaki Tanaka, Hiroki Noda, Hajime Nakanotani and Chihaya Adachi, *Advanced Electronic Materials*, **5**, 1800708 (2019)
   "Effect of carrier balance on device degradation of organic light-emitting diodes based on thermally activated delayed fluorescence emitters"

2. Masaki Tanaka, Ryo Nagata, Hajime Nakanotani and Chihaya Adachi, *Communications Materials* (submitted)
   "Proving the origin of degradation in and organic light-emitting diode derives from triplet exciton interaction by a magnetic field"

3. Masaki Tanaka, Hiroki Noda, Hajime Nakanotani and Chihaya Adachi, *Applied Physics Letters*, **116**, 023302 (2020)
   "Molecular orientation of disk-shaped small molecules exhibiting thermally activated delayed fluorescence in host-guest films"

Joint paper

1. Chin-Yiu Chan, Masaki Tanaka, Hajime Nakanotani and Chihaya Adachi, *Nature Communications*, **9**, 5036 (2018)

Presentations at international conferences

1. Masaki Tanaka, Hiroki Noda, Hajime Nakanotani and Chihaya Adachi, The 3rd *International TADF Workshop*, Fukuoka, Japan (July 19, 2018).

"Change of carrier balance in organic light-emitting diodes having thermally activated delayed fluorescence emitters"

2. Masaki Tanaka, Ryo Nagata, Hajime Nakanotani and Chihaya Adachi, The 4th *International TADF Workshop*, Fukuoka, Japan (August 19, 2019).
"Analysis of TADF-OLED characteristics based on external magnetic field effect"

3. Masaki Tanaka, Ryo Nagata, Hajime Nakanotani and Chihaya Adachi, The 24th *International KRUTYŃ SUMMER SCHOOL 2019*, Krutyń, Poland (September 4, 2019).
"Analysis of TADF-OLED characteristics based on external magnetic field effect"

4. Masaki Tanaka, Ryo Nagata, Hajime Nakanotani and Chihaya Adachi, The 26th *International Display Workshop,* Sapporo Japan (November 27, 2019)
"Analysis Method for Dynamics of Exciton in Organic Light-Emitting Diodes Based on Thermally Activated Delayed Fluorescence Emitters: Magnetic Field Effect as Footprint of Exciton"

Presentations at domestic conferences

1. 田中 正樹、野田 大貴、中野谷 一、安達 千波矢
有機 EL 討論会 第 26 回例会、6 月 21 日、2018 年、東京都
"TADF-OLED の劣化過程における発光スペクトル変化とキャリアバランスの関係"

2. 田中 正樹、野田 大貴、中野谷 一、安達 千波矢

第 79 回応用物理学会秋季学術講演会、9 月 20 日、2018 年、愛知県

“TADF-OLED の劣化過程における発光スペクトル変化と輝度劣化機構”

3. 田中 正樹、永田 亮、中野谷 一、安達 千波矢

有機 EL 討論会 第 28 回例会、6 月 13 日、2019 年、東京都

“熱活性化遅延蛍光 EL における外部磁場印加効果”

4. 田中 正樹、永田 亮、中野谷 一、安達 千波矢

第 80 回応用物理学会秋季学術講演会、9 月 18 日、2019 年、北海道

“外部磁場印加効果を利用した TADF-OLED 特性の解析(I)”

5. 田中 正樹、永田 亮、中野谷 一、安達 千波矢

第 80 回応用物理学会秋季学術講演会、9 月 18 日、2019 年、北海道

“外部磁場印加効果を利用した TADF-OLED 特性の解析(II)”

Acknowledgements

The studies in this thesis were carried out at Adachi laboratory, Department of Chemistry and Biochemistry, Graduate School of Kyushu University from 2017-2019.

I am deeply grateful to Professor Chihaya Adachi for supervising this thesis, excellent experimental environment, helpful discussion, and advise for all of my works. I would also deeply grateful to Professor Yuji Oki and Professor Takuma Yasuda for co-supervising of this thesis. I would also like to thank Associate Professor Hajime Nakanotani for useful comments and helps in preparing of my papers. All the studies in this thesis were financially supported by the Program for Building Regional Innovation Ecosystems of the Ministry of Education, Culture, Sports, Science and Technology, Japan. Dr. Kentaro Harada and Ms. Sachiko Higashikawa supported my work in this program. Dr. Hiroki Noda, Mr. Ryo Nagata, and Mr. Yu Esaki also helped me in many discussions and preparation of chemicals. Ms. Keiko Kusuhara and Ms. Nozomi Nakamura also helps in preparation and measurement of thermal properties of chemicals. Assistant Professor Kenichi Goushi, Associate Professor Takeshi Komino (University of Hyogo), Dr. Yoichi Tsuchiya, Dr. Chin-Yiu Chan, Dr. Yi-Ting Lee, Dr. Umamahesh Balijapalli, Dr. Morgan Auffray, Dr. Ayataka Endo (Kyulux), Dr. Yoshitake Suzuki (Kyulux), Associate Professor Toshinori Matsushima, Associate Professor Ryota Kabe (Okinawa Institute of Science and Technology Graduate University), Assistant Professor Masashi Mamada, Assistant Professor Yuya Tanaka (Chiba University), Mr. Ko Inada, Mr. Ryota Ieuji, Mr. Yuhi Ueda, Dr. Masayuki Yahiro (ISIT), Dr. Hiroshi Fujimoto (i^3opera), Dr. Hin-Wai Mo (i^3opera), Ms. Kaori Nagayoshi (i^3opera), Ms. Nao Onishi (i^3opera), Ms. Hiroko Kuratomi, Ms. Yuko Kawahara, Ms. Rei Sasagawa (Koala tech.), Ms. Hiromi Aizaki (Koala tech.), and

Ms. Chihiro Hino also helped me in experiments and daily life. Finally, I would like to express my gratitude to my family for their moral support and warm encouragements.